ISSN (print) 0207-401X
ISSN (online) 3034-6126

Российская Академия Наук

Volume 44, No.1 January 2025

ЖУРНАЛ РОССИЙСКОЙ АКАДЕМИИ НАУК

ХИМИЧЕСКАЯ ФИЗИКА

ADVANCES IN CHEMICAL PHYSICS

NAUKA
1727

Russian Academy of Sciences
N.N. Semenov Federal Research Center for Chemical Physics of the Russian Academy of Sciences

ХИМИЧЕСКАЯ ФИЗИКА / ADVANCES IN CHEMICAL PHYSICS

No. 1 2025 January

Published 12 times a year
ISSN 0207-401X
ISSN (online) 3034-6126

Published under the guidance of the
Department of Chemistry and Materials Sciences of the Russian Academy of Sciences

Subscription to the journal is accepted without restriction by all divisions of "Rospechat" (No. 39432 in the catalog)

Editorial Office Head **I.N. Mikhailova**
Editorial Office Address: Kosygina st., 4, Moscow, 119991
Phone: +7 495 939 7495
e-mail: jcp@chph.ras.ru
http ://j. chph.ru/

CONTENTS

Vol. 44, No 1, 2025

Chemical physics of nanomaterials

Reactions on surface

ADVANCES IN CHEMICAL PHYSICS, 2025, Vol. 44, No. 1, pp. 3–13

ELEMENTARY PHYSICOCHEMICAL PROCESSES

FORMATION OF IONIC NETWORKS IN MOLTEN SALT MIXTURES. COMPUTER EXPERIMENT

© 2025 A. E. Galashev[a, b]*

[a] *Institute of High Temperature Electrochemistry, Ural Branch of the Russian Academy of Science, Yekaterinburg, Russia*

[b] *Ural Federal University named after the First President of Russia B. N. Yeltsin, Yekaterinburg, Russia*

**e-mail: galashev@ihte.ru*

Received February 08, 2024

Revised February 29, 2024

Accepted March 20, 2024

Abstract. Molten salts are used as heat-conducting media in liquid salt reactors and solar installations. Knowledge of the thermal conductivity of molten salt is necessary for the safe operation of these units. Computational methods are an alternative way to the hard-to-reach experimental way of determining thermal conductivity. In this work, the temperature dependence of the thermal conductivity of the molten salt FLiNaK, as well as this molten salt with NdF_3 dissolved in it, was calculated using the method of equilibrium molecular dynamics. The temperature trend of thermal conductivity, as well as its change after the dissolution of NdF_3 in FLiNaK, is explained based on the determination of the dynamic network of ionic bonds that exists in the molten salt model. Networks of ionic bonds were established with an upper limit of interionic distance of 0.2 nm for both types of salt melts and with a limit of 0.27 nm for the Nd–F network in a melt containing NdF_3. These networks of bonds appear in different parts of the system over time and may disappear completely. The total number of dynamic network nodes, determined during the correlation of heat flows, has an impact on the thermal conductivity value of the simulated system. A new method for interpreting the temperature behavior of the thermal conductivity of molten salt in a computer model can be used for predictive purposes when fluorides of various lanthanides and actinides are dissolved in salt melts.

Keywords: *dynamic ionic bond, fluoride, molecular dynamics, molten salt, phonon, thermal conductivity*

DOI: 10.31857/S0207401X250101e2

1. INTRODUCTION

The interest in molten fluoride salts is largely dictated by their use in liquid salt reactors (LSRs) [1, 2]. Depending on the type of reactor, liquid fluoride salts can act both as a coolant and simultaneously as a solvent for nuclear fuel. Such application of fluoride salts is connected with their stability under irradiation, minimal parasitic absorption of neutrons and relatively low melting point. High-temperature molten salt acts as a heat accumulator and is used as a coolant in solar thermal power plants, which provide uninterrupted power supply during peak hours [3]. Due to high fluorine activity, low-molecular fluorine polymers are able to form new analogs during pyrolytic processing [4].

In spent nuclear fuel (SNF) reprocessing, the goal is to extract and separate from each other all useful elements, including rare earth elements, and to minimize radioactive waste. Rare earth elements are practically significant. They are used in the development of fiber optics, electron beam tubes, and liquid crystal displays [5]. Rare earth elements have properties similar to those of actinoids. The rare-earth element neodymium (Nd) is a constituent of spent nuclear fuel. The element Nd is non-radioactive and can serve as an actinoid simulant in model experiments on nuclear fuel reprocessing.

Molten salts are an unsafe corrosive medium. This dictates the need to know their thermophysical properties, the key among which is thermal conductivity [6, 7]. The error of determination of experimental data on thermal conductivity is high, and the accuracy of calculated data is questioned [8, 9]. According to traditional ideas, thermal

conductivity should be inversely proportional to the distance between atoms [10]. Fluoride molten salts have a positive coefficient of thermal expansion [11]. With increasing temperature, the interatomic distances in fluoride salt melt increase. Therefore, its thermal conductivity should decrease. However, many experimental data indicate that the thermal conductivity of these systems increases with increasing temperature [12, 13].

There is an opinion that the non-standard behavior of thermal conductivity with increasing temperature of the system is due to the neglect of contributions due to radiation and convection. This is supported by data for single-component chloride salts obtained by the method of forced Rayleigh scattering [14]. The scattering data show a negative temperature trend for the thermal conductivity of the salt. However, the same method applied to a fluoride salt (FLiNaK) indicates a small but slightly positive temperature trend [15]. Such studies were performed for FLiNaK of eutectic composition (LiF-NaF-KF (46.5–11.5–42 mol%). Measurements are performed at time intervals (μs) and distances (μm) too short for convection to play a role in heat transfer. The radiative contribution in this method of heat transfer measurement is also small. Thus, so far, no reasonable explanation has been given for the phenomenon of increasing thermal conductivity of fluoride salt melt with increasing temperature.

The term phonon or a quantum of energy of elastic vibrations of a medium was interpreted up to a certain time as a coordinated vibrational motion of atoms of a solid body. However, gradually this term was extended to the liquid state. In a simple liquid, collective excitations of acoustic type with short waves were found in liquid rubidium [16]. They appear due to the viscoelastic response of the liquid. In multicomponent liquids containing charges of both signs, collective excitations of both acoustic and optical types have been experimentally found [17]. The appearance of the latter can be caused by the vibrational process of mutual diffusion of ions.

Some experimental and theoretical facts confirming the existence of phonons in alkali metal halide melts can be cited. The study of phonon dynamics of molten NaI by inelastic X-ray scattering has shown the possibility of propagation of a fast sound mode, about 45% higher than the speed of sound propagation in the ultrasonic range [18]. Optical phonon-like excitations were found computationally in molten NaCl [19]. The authors suggest that such excitations can be associated with rapid fluctuations of the mass concentration (charge in NaCl). The presence of mutual dependence of the wave sources leads to the joint generation of waves of different nature [20].

The aim of the present work is to determine the temperature trend of thermal conductivity of pure molten FLiNaK as well as this salt mixture with dissolved neodymium trifluoride (NdF_3), the molar concentration of which was 15 mol%.

2. COMPUTER MODEL

Molecular dynamic (MD) modeling was performed using the FLiNaK model containing 20000 particles. The composition of the salt mixture (LiF-NaF-KF) was defined as 46.5–11.5–42 mol.%, i.e., corresponding to the eutectic composition of FLiNaK. Thus, the model consisted of 9300 ions of the LiF component, 2300 ions (NaF) and 8400 ions (KF). Integration of the equations of motion was performed with a time step of 0.1 fs. The Nose-Hoover thermostat and barostat were used in the calculations.

The interaction between ions in molten FLiNaK salt mixture was determined using the Born-Huggins-Meyer potential [21]. This means that molten FLiNaK was modeled as a system of point charges in a medium with unit dielectric permittivity, i.e., polarizability effects were not taken into account. The basis for the representation of the potential is the Born solid sphere model. The total energy describing the interaction between ions in the Fumi-Tosi form [22] is represented as

$$U_{ij}^{tot}(r) = U_{ij}^{rep}(r) + U_{ij}^{disp}(r) + U_{ij}^{q-q}(r).$$

The contribution U_{ij}^{rep}, describing short-range repulsion, characterizes the "overlapping" forces arising between ions. The form of repulsive interaction was proposed by Huggins and Mayer [21]:

$$U_{ij}^{rep}(r) = A \exp\left(\frac{\sigma_i + \sigma_j - r}{\rho}\right) \equiv A \exp\left(\frac{\sigma - r}{\rho}\right).$$

Here, the parameter A for the ions included in FLiNaK was determined by the Poling parameters [23], and for the description of the interaction of neodymium with FLiNaK, the value of A was established by quantum mechanical calculation

Table 1. Parameters of the Born-Huggins-Meyer potential for the components of the molten FLiNaK salt [26]

Ion pair	A, eV	σ, Å	ρ, Å	C_{ij}, eV · Å^6	D_{ij}, eV · Å^8
$F^- - F^-$	0.15795	2.358	0.330	10.31	12.26
$F^- - Li^+$	0.29007	1.995	0.299	0.449	0.374
$F^- - Na^+$	0.21096	2.349	0.330	2.8	2.37
$F^- - K^+$	0.21096	2.642	0.338	12.17	13.107
$Li^+ - Li^+$	0.42192	1.632	0.299	0.0455	0.0187
$Li^+ - Na^+$	0.29007	1.986	0.3145	0.54	0.25885
$Li^+ - K^+$	0.29007	2.279	0.2855	7.6	7.49
$Na^+ - Na^+$	0.2637	2.340	0.330	1.04	0.499
$Na^+ - K^+$	0.2637	2.633	0.334	8.1	7.7345
$K^+ - K^+$	0.2637	2.926	0.338	15.16	14.97

[24]. The parameters σ_i and σ_j are defined as "base radii" for ions i and j; ρ is a "stiffness parameter" characterizing a particular salt.

The van der Waals-type dispersion forces are written as

$$U_{ij}^{disp}(r) = -\frac{C_{ij}}{r^6} + \frac{D_{ij}}{r^8},$$

here C_{ij} and D_{ij} are the dipole-dipole and dipole-quadrupole dispersion coefficients, respectively, obtained by Mayer from quantum mechanical calculations based on experimental data on UV absorption; it has been shown that higher-order interactions are negligibly small [25].

The last contribution is determined by the pairwise Coulomb interaction:

$$U_{ij}^{q-q}(r) = \frac{q_i q_j}{r},$$

Where q_i and q_j are ion charges.

The Born-Huggins-Meyer potential parameters for the components of the molten FLiNaK salt are shown in Table 1 [26].

The interaction parameters of FLiNaK melt ions with NdF_3 additive were determined in separate calculations using density functional theory (DFT) [24]. These data are summarized in Table 2. The dispersion interaction was absent in this case, i.e., it was assumed that $C_{ij} = 0$ and $D_{ij} = 0$.

When using periodic boundary conditions (PBCs), the Coulomb interactions between ions were calculated using the Particle-Particle-Particle-Mesh (PPPM) method [27]. The data obtained in MD calculations using PPPM can be extended to the case of confining the basic MD cell to atomically smooth metal walls, on which the energy stability of the deposited atom is independent of the adsorption site [28]. As in the work [24], the modeling involved two steps. First, melting of LiF, NaF, KaF, and NdF_3 crystals in NVT ensemble was carried out. The system was superheated to 3000 K and good mixing in the equilibrium melt was achieved within 0.5 ns. The second step (under NPT and NVE ensemble conditions) involved bringing the system to the experimental density value, geometric optimization, relaxation and calculation of physicochemical properties. After 2.5 ns, when the system reached equilibrium, we proceeded to calculate the thermal conductivity (λ). Fig. 1 shows the FLiNaK-NdF_3 (15 mol%) system before melting and upon completion of the equilibrium melt at $T = 1020$ K (right).

We will establish categorical collective oscillations in the model based on the composition of the salt melt. This is due to the fact that ions having the same electric charge but differing in size and mass behave differently in the molten salt. The content of bonds in the system was monitored by a special program written by us, with the help of which it was possible to determine

Table 2. Parameters of interaction of Nd^{3+} with components of molten salt

Ion pair	A, eV	ρ, Å	σ, Å
$Nd^{3+} - Nd^{3+}$	0.723	0.117	1.96
$Nd^{3+} - F^-$	1.634	0.3328	2.31
$Nd^{3+} - Li^+$	0.012	0.110	1.74
$Nd^{3+} - Na^+$	0.028	0.121	2.00
$Nd^{3+} - K^+$	0.032	0.146	2.36

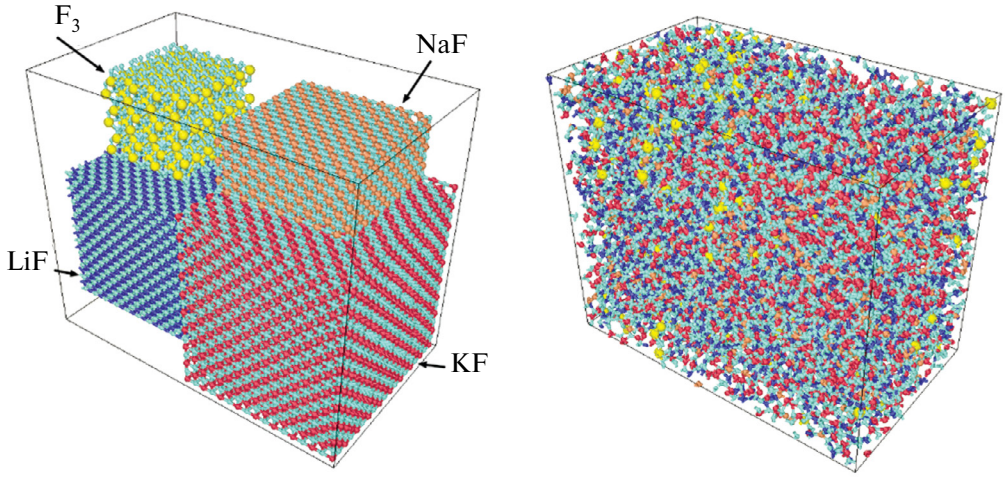

Fig. 1. General view of the FLiNaK + 15 mol.% NdF_3 system before MD calculation ($t = 0$ s, shown on the left), and at the end of the calculation when the melt was obtained at $T = 1020$ K ($t = 2.5$ ns, shown on the right).

which ions and in what quantity form a bond network with a certain size of bond length. First of all, when studying the systems FLiNaK and FLiNaK+ NdF_3, we were interested in the number of Li^+ bonds with F^-. This is because Li^+ ions are the most representative among the positive ions in these systems. In addition, they are the most dynamic ions that respond more sharply than all other positive ions to changes in external conditions, i.e., temperature and density. Finally, these ions form the closest instantaneous bonds with F^- ions, characterized by the shortest bond length. According to [29], a chemical covalent bond between pairs of Li-F and Nd-F atoms is formed when they approach each other at distances of 0.185 and 0.258, respectively. The program for determining the bonding of ions in the system analyzed the coordinates of all ions in the system recorded at equal time intervals (5 ps). Using this program, it was found that at all temperatures and densities considered, bonds with lengths no greater than 0.2 nm are established almost exclusively between the Li ions$^+$ and F^-. All other positive ions accounted for less than 0.1% of such bonds with F^- ions. Thus, the value of 0.2 nm served as the main bonding parameter in the models of the studied salt melts. Due to the large charge, Nd^{3+} ions are much more strongly attracted to F- ions than univalent ions. Therefore, when the system with dissolved NdF_3 was investigated, attention was also paid to the formation of a bonding network consisting of Nd^{3+} and F^- ions. In this case, a value of 0.27 nm served as the threshold value for bond formation. Both threshold distances (0.20 and 0.27 nm) fall in the range between the first maximum and minimum of the corresponding partial radial distribution function. The minimum distance between Li^+ and F^- ions in molten FLiNaK and this salt containing neodymium trifluoride at different temperatures was ~0.14–0.17 nm, and between Nd^{3+} and F^- ions was 0.203–0.207 nm.

The principle of operation of the connectivity program is based on the selection of distances between all (or some specific) positive and all negative ions of the system that satisfy the connectivity condition. When the list of such distances was saved, the numbers of ions between which these small distances were set were simultaneously saved. After complete such processing of the entire configuration, the connectivity of the selected charged particles was analyzed on the basis of the stored numbers of the selected ions. The necessary condition for obtaining a cohesive structure, i.e., a network, was the presence of at least two bonds (close neighbors) for each selected ion. In other words, the number of each bonded ion had to appear in the list of numbers at least twice. Thus, at the output we had the coordinates and numbers of the ions forming the linked network. Now, in order to establish the numbers and quantities of different ions forming the network, it was enough to perform another reduction of the list of ions so that each of the ions forming the network appeared in it once. As a result, we obtained the numbers, and, hence, the coordinates of the ions forming the network of bonds. In addition, the minimum and maximum distances in the resulting bond network were

determined. The number of ions (both positive and negative) forming a bonded network is visualized in relative units or percentages with respect to the total number of ions in the system. In the following, two types of dynamic categorical bonds will be considered, whose lengths do not exceed 0.2 nm and 0.27 nm. The former are mainly related to the Li^+ -F^- ion pair, and the latter to the Nd^{3+}-F^- pair.

The thermal conductivity of the pre-equilibrated structures was calculated according to the Green-Cubo formalism [30]:

$$\lambda_\alpha = \frac{1}{k_B V T^2}\int_0^\infty \left\langle S_\alpha(t) S_\alpha(0)\right\rangle \mathrm{d}t'$$

where k_B is the Boltzmann constant, t is time, T and V are the temperature and volume of the system, and $\left\langle S_\alpha(t) S_\alpha(0)\right\rangle$ is the current autocorrelation function of the α component of heat. The total correlation time was 50 ps and the simulation was run for 2.1 ns.

Each of the components $\alpha = x, y, z$ of the heat flux was determined according to the expression:

$$S = \frac{1}{2}\sum_{i=1}^{N}\left[m_i V_i^2 + \sum_{j\neq i}^{N} u\left(r_{ij}\right)\right] V_i + \frac{1}{2}\sum_{i=1}^{N}\sum_{j\neq i}^{N}\left(r_{ij} F_{ij}\right) V_i,$$

where m_i, v_i are the mass and velocity of the i ion; $u\left(r_{ij}\right)$ is the contribution to the potential energy from the interaction between the ions i and j, and r_{ij} is the distance between these ions; the strength of the interaction between the ions i and j is denoted as F_{ij}; N is the number of ions in the system.

Here, the first summand reflects the flux of total energy, while the second summand reflects the flux associated with the forces acting between atoms. The value of λ was determined as an arithmetic average for its three components (λ_x, λ_y and λ_i).

3. MODELING RESULTS

The distribution over the number of nodes in the bond network during the correlation time for the thermal conductivity calculation of the FLiNaK+15 mol% NdF_3 system is shown in Fig. 2. Fig. 2a shows the number of nodes formed by Li^+ and F^- ions in the network, while Fig. 2b shows the number of nodes in the network formed by Nd^{3+} and F^- ions. In both cases, the number of grid nodes is presented as a percentage of the total number of ions in the whole system. It is clear from the figure that those and other networks of closely related ions can appear and disappear during the evolution of the system. The number of Li^+ ions in the system exceeds the number of Nd^{3+} ions more than 5 times. Therefore, the networks formed involving Li^+ ions are more representative. It can be noted that the average number of nodes in the Nd-F network decreases with increasing temperature, starting from T = 850 K. However, this pattern is not observed in the case of the Li-F network.

Li^+ ions fill the whole volume of the MD cell reflecting the FLiNaK+15 mol% NdF_3 system (Fig. 3). However, it cannot be said that their distribution over the cell volume is homogeneous. The periphery of the cell is less populated with Li^+ ions, than the center of the cell. This is probably due to the specificity of the periodic boundary conditions in a disordered multicomponent ionic system.

Fig. 4 shows the largest observed ionic Li-F network in the system with NdF_3. It should be noted that in general the time fluctuating Li-F networks in the system containing NdF_3 incorporation are more representative than those in pure FLiNaK under similar external conditions. It means that dilution of the salt melt by introduction of much heavier trivalent ions Nd^{3+}, as well as introduction of imbalance between the number of positive and negative ions in the studied system (while maintaining the equality of common charges between those and other ions) promotes the convergence of Li^+ and F^- ions and their unification into a single network with the network link size ⩽ 0.2 nm.

Heavy Nd ions$^+$ are distributed unevenly over the MD cell volume (Fig. 5). This non-uniformity may be due to a number of factors present in the model system (the shape of the interaction potentials used, neglecting the effect of polarizability on ion interaction, the influence of periodic boundary conditions, etc.). However, it is possible that such inhomogeneity will also occur in real molten salt systems due to some other reasons, such as insufficiently effective mixing. Trivalent Nd^{3+} ions tend to retain F^- ions near them. Due to the low mobility of Nd^{3+} ions, their distribution pattern in the MD cell does not change much with increasing temperature. In this case, temperature changes in the morphology of the Nd-F network occur mainly due to the much more mobile F^- ions. The Nd-F network obtained at 1020 K appears as an irregularly shaped cluster (Fig. 6). At all temperatures

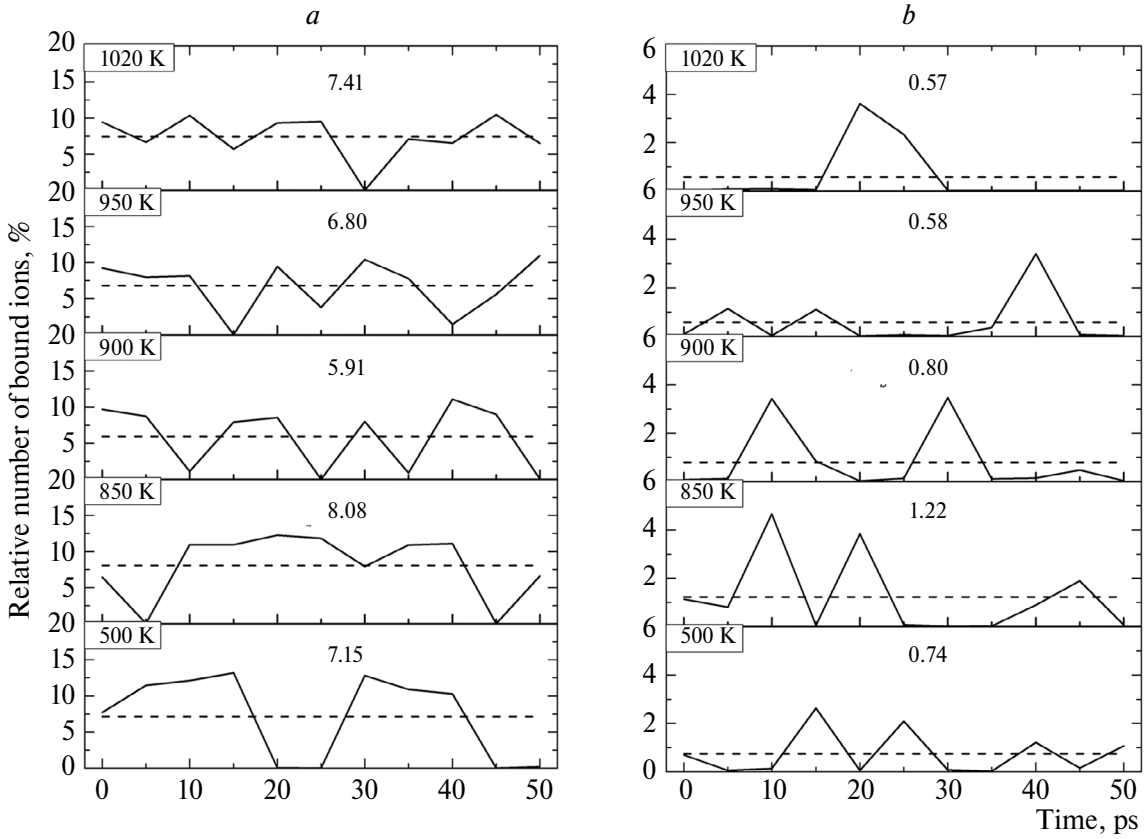

Fig. 2. Relative number of interconnected positive and negative ions in the FLiNaK+15 mol.% NdF_3 system: (a) forming $Li^+ - F^-$ bonds with the length not exceeding 0.2 nm and (b) Nd^{3+}- F^- bonds with the length ⩽0.27 nm; the dashed line and figures show the average values of the number of interconnected ions N_b; the temperature to which the obtained dependence applies is indicated in the upper left corner of each part of this figure.

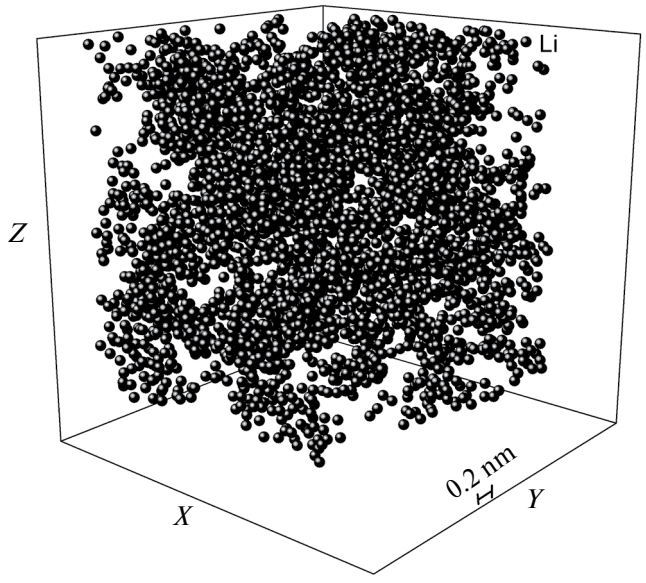

Fig. 3. Placement of Li ions$^+$ in the system FLiNaK+15 mol% NdF_3 (800 K) at the end of the calculation.

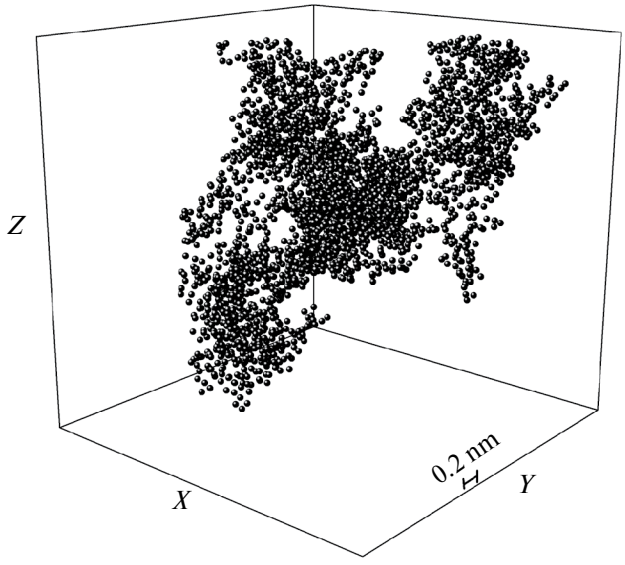

Fig. 4. Nodes of the largest bond mesh with bond lengths of 0.2 nm or less between positive and negative ions in the FLiNaK+15 mol% NdF_3 system at 800 K.

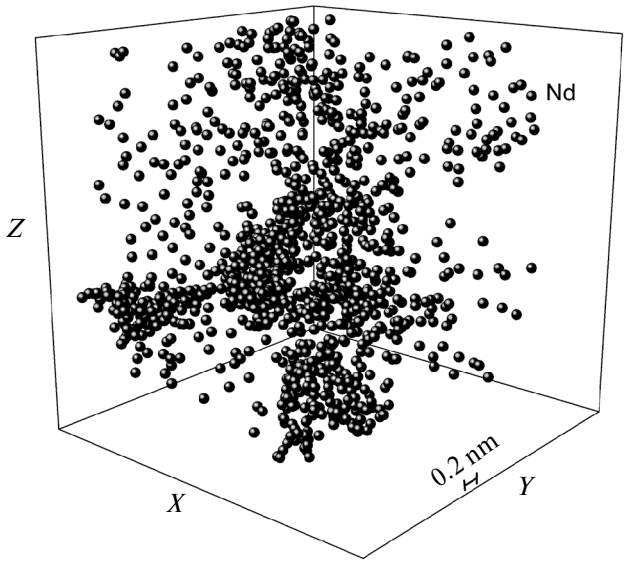

Fig. 5. Placement of Nd^{3+} ions in the FLiNaK+15 mol% NdF_3 system at the end of the calculation at 1020 K.

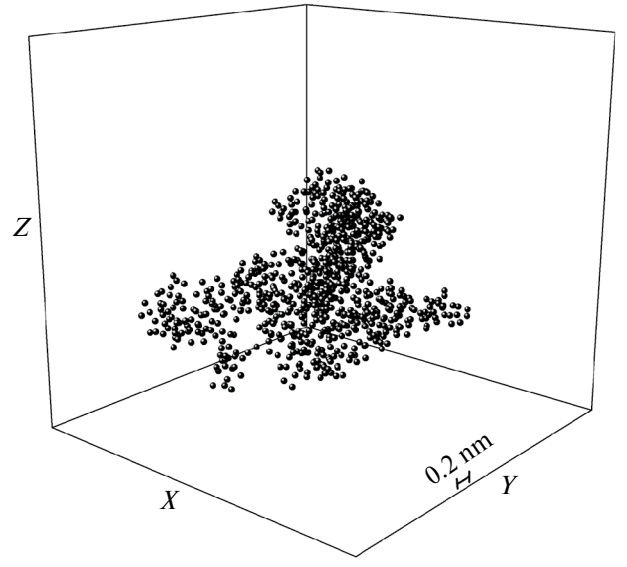

Fig. 6. Bond mesh nodes between Nd^{3+} and F^- ions in the FLiNaK+15 mol% NdF_3 system with bond lengths of 0.27 nm or less at the end of the calculation at 1020 K.

considered, the size of Nd-F networks is inferior to that of Li-F networks. However, their appearance should also influence the value of the thermal conductivity coefficient of the salt mixture.

The average number of ions forming a temporary bonding network in the molten salt systems FLiNaK and FLiNaK+15 mol% NdF_3 as a function of temperature is shown in Fig. 7. As can be seen from the figure, the average number of Li^+ and F^- ions

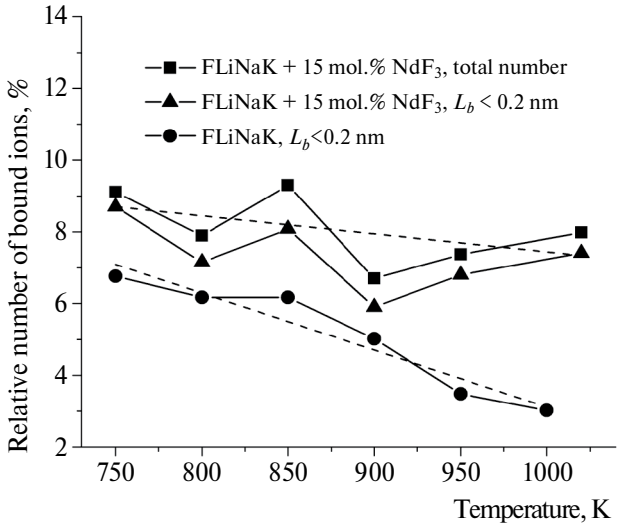

Fig. 7. Temperature dependence of the relative number of bound ions for the systems: FLiNaK and FLiNaK+15 mol.% NdF_3; dotted line is a linear approximation of the presented dependences; in the Fig. the term "total number" means that the bond lengths L_b of all positive ions with F^- not exceeding 0.2 nm and L_b of dissolved ions with Nd^{3+}–F^- bonds not exceeding 0.27 nm are taken into account.

creating a network in the system containing Nd^{3+} ions at all considered temperatures exceeds the analogous characteristic for the same ions in the FLiNaK system. The Nd^{3+} and F^- ions creating their network increase the aggregate of ions producing temporary ionic networks, bringing their average number in the temperature range $750 \leqslant T \leqslant 1020$ K to 8.05% of the total number of ions in the system. In pure molten FLiNaK over the same temperature range, the average fraction of Li^+ and F^- ions producing ion networks was 5.10%. Thus, dissolution of neodymium trifluoride in molten FLiNaK increases ion network formation, which in turn enhances the thermal conductivity of the salt melt. The trend of the temperature dependences is represented in Fig. 7 by dashed lines. The upper dashed lithium line reflects a linear approximation of the two temperature dependences shown in the figure for the system containing Nd^{3+} ions, while the lower dashed line refers to pure FLiNaK. It can be seen that in the case of both systems, the fraction of ion network nodes decreases with increasing temperature. We believe that the appearance of ionic networks is an important factor in increasing the thermal conductivity of the system. Therefore, in both systems we should expect the thermal conductivity to decrease with increasing temperature.

Fig. 8 shows the temperature dependences of thermal conductivity of molten salt mixtures of FLiNaK and FLiNaK+15 mol% NdF_3 calculated by our MD model. The experimental temperature dependence of pure FLiNaK obtained by laser flash method [31] is also shown here. As can be seen from the figure, all the dependences presented therein have a negative temperature trend. In addition, each of the dependences is well approximated by a linear approximation. A good agreement between the calculated data for pure FLiNaK and the corresponding experimental data is observed. The coefficient λ obtained at all considered temperatures for the salt melt with dissolved NdF_3 turns out to be higher than the corresponding coefficient calculated for pure FLiNaK. On average, the difference between thermal conductivities of FLiNaK and FLiNaK+15 mol% systems at the temperature range $750 \leqslant T \leqslant 870$ K amounted to 6.7%. There is reason to believe that the increase in thermal conductivity in the salt melt containing NdF_3 is achieved by increasing the size of pulsating ionic networks when this additive appears in FLiNaK. The average size of ionic networks in systems with NdF_3 increased by 25.2% in the temperature range over which the thermal conductivity was determined.

4. DISCUSSION OF RESULTS

In common parlance, thermal conductivity describes how easily a material can transfer heat in the presence of an applied temperature gradient. Lattice heat conduction is usually referred to as heat conduction due to vibrations of lattice ions in a solid. The interaction of phonons causes anharmonicity of the vibrations. The interaction of two modes (ω_1, q_1) and (ω_2, q_2) may result in a third mode (ω_3, q_3). A nonzero probability of this process exists if:

$$\omega_1 + \omega_2 = \omega_3 \text{ and } q_1 + q_2 = q_3 + Q,$$

if Q is equal to the inverse lattice vector, the so-called overshooting process occurs. In this case, the total phonon flux changes direction. It is the overshooting processes that cause thermal resistance, not the normal processes when $Q = 0$. The physical mechanisms explaining the thermal conductivity of molten salts are still insufficiently understood.

There are experimental facts indicating the dependence of thermal conductivity on the coordination number and degree of bonding of atoms in various systems with covalent bonds. It has been shown that when a-SiO, a-SiC and a-Si films are hydrogenated, their thermal conductivity can decrease up to 2 times [32]. It was found that the speed of sound, atomic density and heat capacity cannot explain the measured decrease in thermal conductivity of thin amorphous films. Energy transfer occurs through a non-hydrogen network of atoms. The disruption of the cohesion of the basic atoms is the reason for the decrease in thermal conductivity of amorphous films.

The rupture of the continuity of the medium can lead to a sharp decrease in thermal conductivity. Thus, in the case of strengthening of aluminum-based composite material by reinforcing with graphene flakes, the thermal conductivity of the composite decreased (relative to aluminum) by 9 times [33].

The thermal conductivity of a thin film of aluminum nitride decreased by a factor of 3.6 during its heating from 100 K to 400 K [34]. The authors explain the sharp decrease in thermal conductivity by the formation of vacancies during heating, the presence of which causes the greatest dissipation. At the same time, 50% of the thermal conductivity was provided by phonons with a wavelength less than 0.3 μm.

The thermal conductivity can be controlled by changing the coordination of atoms. Based on MD modeling, it was shown that the mass density and coordination of atoms significantly

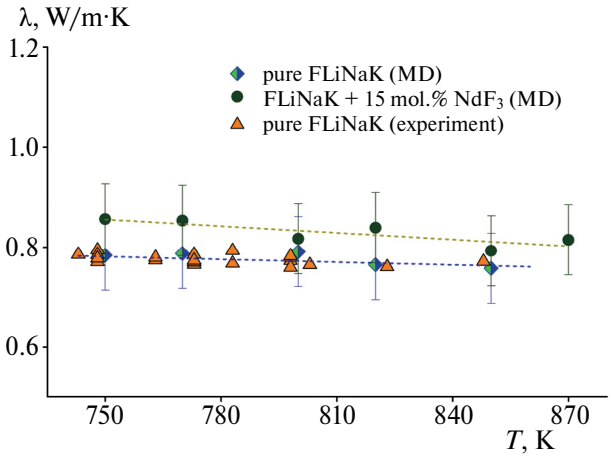

Fig. 8. Thermal conductivity of the FLiNaK and FLiNaK+15 mol% NdF_3 systems determined in the molecular dynamic calculation (present work) and in the λ coefficient experiment by laser flash method [31].

affect the fundamental vibrational characteristics of the *a*-SiC: H system [30]. The median coordination of atoms increases with increasing density, which entails a linear increase in thermal conductivity.

Ions in the salt melt oscillate and are exposed to thermal energy. In collisions, the ions transfer kinetic energy to their neighbors, who then excite the ions further downstream from the heat source. The vibrations caused by the thermal energy propagate through the material to cooler regions. The thermal conductivity of most liquids decreases with temperature, and when approaching the boiling point, the decrease in thermal conductivity becomes almost linear.

Due to the Coulomb long-range action, some instantaneously locally stabilized parts of the salt melt appear to be bound together [35]. Therefore, in the region of low temperatures there are prerequisites for the realization of a phonon-like mechanism of heat conduction in the salt melt. Here phonons propagate over small distances within a short time interval, and the low-temperature melt has high thermal conductivity. As the temperature increases, a breakdown of the partially bonded structure of the melt is observed. Breaks in the continuous bonding of salt melt fragments, often repeated in time, create obstacles for phonon propagation. With increasing temperature such obstacles become more and more. Therefore, due to increased phonon scattering, the thermal conductivity of the salt melt decreases with increasing temperature. Various impurities existing in the real system can contribute to consolidation or, on the contrary, create a rupture in the continuity of the salt melt. As a result, the temperature behavior of thermal conductivity in a physical experiment can take somewhat unexpected forms, for example, be insensitive to temperature changes, or even increase with increasing temperature.

In the present work, we have considered only two types of categorical bonds formed by Li^+ -F^- and Nd^{3+}-F^- ion pairs. These fluctuating bonds are stronger than the bonds formed by Na^+ and K^+ ions with F^- ions. This is because Li^+ cations, because of their small size, can approach the F^- anions at closer distances than Na^+ and K^+ ions are able to do. At the same time, Nd^{3+} ions, because of their large electric charge, have a significantly greater ability to attract F^- ions compared to Na^+ and K^+. In other words, the categorical bonding networks formed by Li^+-F^- and Nd^{3+}-F^- pairs appear to be significantly more effective by the nature of the effect on thermal conductivity (as well as viscosity).

In this work, for the first time, attention is drawn to the ion connectivity observed in a molten salt mixture. Each configuration of the ion network is short-lived. It arises and disappears. In addition, the ion network is able to move through the volume of the system. Previously, when studying the structure of salt melts, only attention was paid to the formation of complex ionic groups, for example, in the melt of Na_3AlF_6, Al-F groups were formed [36, 37]. In this case, the system consists of sufficiently light ions of three types: Na^+, Al^{3+} and F^-. Using the first-principles molecular dynamics, three rather stable formations were found in such a molten salt: AlF_4, AlF_5, and AlF_6 [37].

When heavy ions such as Th^{4+} and U^{4+} are dissolved in AF^- fluoride salt melts ($A=Li^+$, Na^+, K^+), thorium and uranium cations can collect an average of 8 F^- ions [38]. The formation of such complexes when dissolved in the electrolyte up to 35 mol% of ThF_4 or UF_4 leads to an increase in the viscosity of the salt melt.

5. CONCLUSION

The development of new reactors and solar energy systems requires accurate prediction of the thermophysical properties of molten salts. Thermal conductivity is one of the most important properties in this respect. In the present work, the temperature dependence of thermal conductivity of the molten salt FLiNaK, including dissolved neodymium trifluoride, has been calculated by the molecular dynamics method. To explain the change in thermal conductivity caused by dissolution of the lanthanide salt NdF_3 in this salt mixture, as well as the temperature trend of thermal conductivity of pure FLiNaK, the formation of certain ionic bonds in the systems under consideration has been investigated. The existence of connectivity between the ions creating the shortest bonds ($\leqslant$ 0.2 nm) in both types of the considered systems, as well as the connectivity of Nd^{3+} and F^- ions (with bond length $\leqslant$ 0.27 nm) in the system in dissolved NdF_3 was established. The revealed dynamic networks of ionic bonds have a pulsating character in time, i.e. they can appear from time to time in different parts of the system and completely or partially disappear. The correlation between the total number of ionic network nodes, on average existing on the time

interval of determining the autocorrelation function of heat fluxes, and the value of thermal conductivity of the system under study has been established. Thus, by determining the degree of development of dynamic ion networks of the established categories, it is possible to predict changes in the thermal conductivity of the system caused by the dissolution of heavy ion fluorides and temperature changes.

The developed method for predicting thermal conductivity behavior will be useful in predicting this important thermophysical property for multicomponent salt melts with dissolved lanthanide and actinoid fluorides.

FUNDING

The work was completed on the topic of state assignment No. 125021702324-9 and in the frame of the agreement No. 075-03-2025-258 dated 17.01.2025 (theme number FEUZ-2025-0002);

CONFLICT OF INTEREST

The author of this paper declares that he has no conflict of interest.

REFERENCES

1. *Halliday C., Hatton T.A.* // Appl. Energy. 2020. Vol. 280. Art. No. 116016. https://doi.org/10.1016/j.apenergy.2020.116016
2. 2*Sorbom N., Ball J., Palmer T. R., Mangiarotti F. J., Sierchio J. M., et al.* // Fusion Eng. Des. 2015. Vol. 100. P. 378. https://doi.org/10.1016/j.fusengdes.2015.07.008
3. *Akanda M. A. M., Shin D.* // J. Ener. Storage. 2023. Vol. 60. Art. no. 106608. https://doi.org/10.1016/j.est.2023.106608
4. *Ignatyeva L. N., Mashenko V.A., Gorbenko O. M., Buznik V. M.* // Chem. Physics 2023. No. 11. p. 23. https://doi.org/10.31857/S0207401X23110031
5. *Froese B. C.* // Adsorption of Neodymium Experiment Design to Simulate Nuclear Fuel Reprocessing. Syracuse: University Honors Program Capstone Projects, 2011. Pp. 5–14. https://surface.syr.edu/honors_capstone/249
6. *Cervi E., Lorenzi A., Cammi A., Luzzi L.* // Chem. Eng. Sci. 2019. Vol. 193. P. 379. https://doi.org/10.1016/j.ces.2018.09.025
7. *Nunes V. M. B., Lourenco M. J. V., Santos F. J. V., Nieto de Castro C. A.* // J. Chem. Eng. Data. 2003. Vol. 48. No. 3. P. 446. https://doi.org/10.1021/je020160l
8. *Gheribi A. E., Chartrand P.* // J. *Chem*. Phys. 2016. Vol. 144. No. 8. P. 084506. https://doi.org/10.1063/1.4942197
9. *Gheribi A. E., Torres J. A., Chartrand P.* // Sol. Energy Mater. Sol. Cells. 2014. Vol. 126. P. 11. https://doi.org/10.1016/j.solmat.2014.03.028
10. *Ross R. G.* // Rep. Prog. Phys. 1984. Vol. 47. No. 10. P. 1347. https://doi.org/10.1088/0034–4885/47/10/002
11. *Romatoski R. R., Hu L. W.* // Ann. Nucl. Energy. 2017. Vol. 109. No. 2–3. P. 635. https://doi.org/10.1016/j.anucene.2017.05.036
12. *An X.-H., Cheng J.-H., Yin H.-Q., Xie L.-D., Zhang P.* // Int. J. Heat Mass Transfer. 2015. Vol. 90. P. 872. https://doi.org/10.1016/j.ijheatmasstransfer.2015.07.042
13. *Robertson S. G., Wiser R., Yang W., Kang D., Choi S., et al.* // J. Appl. Phys. 2022. Vol. 131. No. 22. 225102. https://doi.org/10.1063/5.0088059
14. *Nagasaka Y., Nakazawa N., Nagashima A.* // Int. J. Thermophys. 1992. Vol. 13. No. 4. P. 555. https://doi.org/10.1007/BF00501941
15. *Robertson G., Short M. P.* // Rev. Sci. Instrum. 2021. Vol. 92. Art. No. 064905. https://doi.org/10.1063/5.0049727
16. *Copley J. R. D., Rowe J. M.* // Phys. Rev. Lett. 1974. Vol. 32. No. 2. P. 49. https://doi.org/10.1103/PhysRevLett.32.49
17. *Demmel F., Hosokawa S., Pilgrim W.-C.* // J. Phys.: Condens. Matter. 2021. Vol. 33. No. 37. Art. No. 375103. https://doi.org/10.1088/1361–648X/ac101c
18. *Hosokawa S., Demmel F., Pilgrim W.-C., Inui M., Tsutsui S., Baron A. Q. R.*. // Electrochem. 2009. Vol. 77. No. 8. P. 608. https://doi.org/10.5796/electrochemistry.77.608
19. *Bryk T., Mryglod I. M.* // J. Mol. Liquids. 2005. Vol. 120. No. 1–3. P. 83. https://doi.org/10.1016/j.molliq.2004.07.041
20. *Kishevetsky S. P., Kudryaeva Yu.A., Gavrilov N. M.* // Chem. Physics. 2023. Vol. 42. No. 10. p. 77. https://doi.
21. *Tosi M. P., Fumi F. G.* // J. Phys. Chem. Solids. 1964. Vol. 25. No. 1. P. 45. https://doi.org/10.1016/0022–3697(64)90160-x
22. *Adams D. J., McDonald I. R.* // J. Phys. C: Solid State Phys. 1974. Vol. 7. No. 16. P. 2761. https://doi.org/10.1088/0022–3719/7/16/009

23. *Pauling L.* // J. Amer. Chem. Soc. 1929. Vol. 51. No. 4. P. 1010. https://doi.org/10.1021/ja01379a006
24. *Galashev A. Y., Rakhmanova O. R., Abramova K. A., Katin K. P., Maslov M. M., et al.* // J. Phys. Chem. B. 2023. Vol. 127. No. 5. P. 1197. https://doi.org/10.1021/acs.jpcb.2c06915
25. *Mayer J. E.* // J. Chem. Phys. 1933. Vol. 1. No. 4. P. 270. https://doi.org/10.1063/1.1749283
26. *Wang H.* Ph. D. Dis. Molecular dynamics simulations of molten salts: Force field evaluation and development. Indiana, Notre Dame: University of Notre Dame, 2022
27. *Ishii Y., Sato K., Salanne M., Madden P. A., Ohtori N.* // J. Phys. Chem. B. 2014. Vol. 118. No. 12. P. 3385. https://doi.org/10.1021/jp411781n
28. *Rudenko E. I., Dokhlikova N. V., Gatin A. K., Sarvadiy S. Y., Grishin M. V.* // Chem. Physics. 2023. Vol. 42. No. 7. C. 70. https://doi.org/10.31857/50207401X23070166
29. *Cordero B., Gomes V., Platero-Prats A., Reves M., Echeverria J., et al.* // Dalton Trans. 2008. Vol. 21. No. 21. P. 2832. https://doi.org/10.1039/b801115j
30. *Thakur S., Dionne C. J., Karna P., King S. W., Lanford W.* // Phys. Rev. Mater. 2022. Vol. 6. Art. no. 094601. https://doi.org/10.1103/PhysRevMate rials.6. 094601
31. *Rudenko A., Redkin A., Il'ina E., Pershina S. et al.* // Materials. 2022. Vol. 15. No. 16. Art. No. 5603. https://doi.org/10.3390/ma15165603
32. *Braun I. L., King S. W., Giri A., Gaskins J., Sato M., et al.* // Appl. Phys. Lett. 2016. Vol. 109. No. 19. Art.No. 191905. https://doi.org/10.1063/1.4967309
33. *Vozniakovskiy A. A., Vozniakovskiy A. P., Kidalov S. V., Zavarinsky V. I.* // Chem. Physics. 2021. T. 40. No. 6. P. 14. https://doi.org/10.31857/S0207401X21060169
34. *Xu R. L., Rojo M. M., Islam S. M., Sood A., Vareskic B., et al.* // J. Appl. Phys. 2019. Vol. 126. No. 18. Art.No.185105. https://doi.org/ 10.1063/1.5097172
35. *Galashev A. Y.* // Appl. Sci. 2023. Vol. 13, No. 2. P. 1085. https://doi.org/10.3390/app13021085
36. *Özen A. S., Akdeniz Z.* // J. Mol. Liquids. 2022. Vol. 368. Part B. P. 120771. https://doi.org/10.1016/j.molliq.2022.120771
37. *Li J., Guo H., Zhang H., Li T., Gong Y.* // Chem. Phys. Lett. 2019. Vol. 718, P. 63. https://doi.org/10.1016/j.cplett.2019.01.035
38. *Bessada C., Zanghi D., Salanne M., Gil-Martin A., Gibilaro M., et al.* // J. Mol. Liquids. 2020. Vol. 307. No. 2. Art. No. 112927. https://doi.org/10.1016/j.molliq.2020.112927

ADVANCES IN CHEMICAL PHYSICS, 2025, Vol. 44, No. 1, pp. 14–21

STRUCTURE OF CHEMICAL COMPOUNDS, QUANTUM CHEMISTRY, SPECTROSCOPY

KINETICS THE PROLIFERATION OF CORRELATIONS IN MULTIPLE QUANTUM NMR SPECTROSCOPY

© 2025 V. L. Bodneva, A. S. Vetchinkin, B. V. Lidsky, A. A. Lundin*, S. Y. Umansky, Y. A. Chaikina, and A. I. Shushin

Semenov Federal Research Center for Chemical Physics, Russian Academy of Sciences, Moscow, Russia

** e-mail: ya-andylun2012@yandex.ru*

Received January 22, 2024

Revised February 02, 2024

Accepted February 20, 2024

Abstract. It is shown that the number of spins in clusters of coherently correlated states arising under conditions of multiplequantum NMR – spectroscopy in a solid increases exponentially with time. The Smolukhovsky equation was used to study the above processes. Possible processes of cluster degradation were not taken into account. The results obtained are in good agreement with the experimental data, at least up to about 10^5 spins in the cluster.

Keywords: *spin, radio spectroscopy, multi-quantum NMR, paramagnet, quantum technologies, spin dynamics, multi-spin correlations*

DOI: 10.31857/S0207401X250102e2

1. INTRODUCTION

The rapid (both experimental and theoretical [1–3]) development of multi-pulse coherent solid-state NMR spectroscopy, which began in the late 1960s, led to the emergence and further intensive development, beginning in the 1980s, of multi-quantum (MQ) NMR spectroscopy [4–6]. The new NMR methods that emerged with the growth of MQ spectroscopy proved to be extremely useful and effective, for example, in the study of clusters and local structures, in particular those formed on surfaces [7], liquid crystal structures [8], nanoscale cavities [9], for the study of the structure of macromolecules (e.g., proteins) (Nobel Prize in Chemistry for 2002) [10], and so on.

The basis of MQ-spectroscopy is the observation of the behavior of multispin-multiquantum coherent states. Multiquantum coherences are coherent transitions between states with a change of the magnetic quantum number by more than one. Usually in MQ NMR spectroscopy this change is counted from the main filled state of the system with total spin equal to 0 at high temperatures. The magnitude of the change in the magnetic (spin) quantum number is called the coherence order. The above-mentioned coherent states arise due to the so-called "spin alchemy", when the secular Hamiltonian of inter-nuclear dipole-dipole interactions (see below) acting usually in a solid body is replaced by a transformed Hamiltonian (from "lead Hamiltonian to gold Hamiltonian"), non-secular with respect to the external permanent magnetic field [1,4–6], due to very fast irradiation of the sample with a certain sequence of radio-frequency pulses. The correlated coherent states arising under the action of the new Hamiltonian propagate through the sample, forming clusters of correlated states.

Emerging coherent states turned out to be fundamentally important in the study of physical processes necessary for the development of quantum informatics (creation of quantum registers) [11]. The point is that the system of nuclear magnetic moments (spins) of a solid body observed by NMR methods serves as a good example of a closed system, and, as it is known, in a closed system quantum information is preserved with time [11]. At the same time, initially localized in single-particle (single-spin) states, this information is redistributed over the set of degrees of freedom, which can be represented by the appearance of time correlation functions

(TCFs) of a very complex structure. It turns out that these TCFs describe, in principle, the propagation ("spreading") of quantum information practically on any multiparticle system. The mentioned process of propagation is called scrambling (see, for example, [12–14] and the bibliography given there), and the above mentioned TCFs have, in a certain sense, universal character.

The construction of a consistent theory describing the high-temperature spin dynamics of solids and any rigorous calculation of the corresponding TCFs is an extremely complex multi-particle and still very little investigated problem. In the traditional statistical model [4,5], by means of the simplest algebraic estimation of the number of transitions between levels of large clusters, a Gaussian distribution was proposed, in fact empirically, for the distribution of coherences of different order M in the MQ spectrum

$$G_M(T) = \frac{1}{\sqrt{\pi K(\tau)}} \exp\left(-\frac{M^2}{K(\tau)}\right). \qquad (1)$$

The second moment (dispersion) of the distribution in this model $K(\tau)/2$ is determined by the average number of spins $K(\tau)$ between which a dynamical correlation has been established during the preparation time τ [5, 15]. This number, called the number of correlated spins or the effective (average) cluster size, grows with increasing preparation time τ.

In [15,16] we found that for three-dimensional nuclear spin systems with secular dipole-dipole interaction (or with effective two-spin-two-quantum interaction (see below)) the second moment of the MQ NMR, which determines the number of correlated spins, grows exponentially with time τ in the absence of any external perturbations. Although the above result was obtained with the help of a very complicated diagrammatic technique of iterative type, developed specially in [15], which significantly complicates the qualitative understanding of the general picture of what is happening, the formulas obtained in [15,16] allowed, in particular, to correctly describe the experimental data of [17–20] on the observation of emerging clusters of correlated spins containing up to about 10^5 particles.

The purpose of the present work is to describe the functional dependence of the growth and growth rate of the number of correlated particles in clusters on the basis of the Smoluchowski equation describing particle aggregation [21, 22]. This allows us to give at least a qualitative description of the above experimental facts. Here we will consider the process of correlation expansion as a process of merging (aggregation) of clusters. In this case, one spin is also a "single-particle cluster".

2. HAMILTONIAN, SPIN-SPIN INTERACTIONS AND THE PROCESS OF CORRELATION FORMATION

As is known [23], the main reason for the broadening of NMR B lines in nonmetallic diamagnetic solids is the secular part of the inter-nuclear dipole-dipole interactions, which fully determines the dynamics of the nuclear spin system:

$$H_d = \sum_{i \neq j} b_{ij} S_{zi} S_{zj} -$$

$$-(1/4)\sum_{i \neq j} b_{ij} (S_{+i} S_{-j} + S_{-i} S_{+j}) = H_{zz}^0 + H_{ff}, \quad (2)$$

Where $b_{ij} = \gamma^2 \hbar (1 - 3\cos^2 \theta_{ij}) / r_{ij}^3, \vec{r}_{ij}$ is the vector connecting spins i and j, θ_{ij} is the angle formed by the vector $\vec{r}_{ij}$ with a constant external magnetic field, γ is the gyromagnetic ratio, $S_{\alpha i}$ is the α *-component* ($\alpha = z, +, -$) of the vector operator of the spin at node i. Hereinafter the energy is expressed in frequency units.

Usually, when using pulsed methods in solid-state NMR, the base Hamiltonian (2) is transformed using "spin alchemy" into other Hamiltonians of interest to the researcher [1]. For example, in conventional MQ NMR spectroscopy, the base Hamiltonian is transformed into an effective Hamiltonian [4,5]:

$$H_{eff} = (-1/4)\sum_{i \neq j} b_{ij} (S_{+i} S_{+j} + S_{-i} S_{-j}), \qquad (3)$$

non-secular with respect to the external magnetization. Under its influence, during the so-called "preparatory period" of some duration τ, the initial magnetization is pumped into various TCFs of rather complicated structure depending on the product of a different number (Q) of spin operators, which we will call clusters. In other words, the equilibrium high-temperature density matrix in a strong permanent magnetic field has the form [23]

$$\rho_{eq} \propto 1 + \frac{\gamma \hbar H_0}{kT} \sum_{j=1}^{N} S_{zj}, \qquad (3a)$$

(where k is the Boltzmann constant, T is the temperature, N is the total number of spins in the sample), turns into a nonequilibrium density

matrix, which is conveniently represented as a sum of non-diagonal elements ρ_M with a certain difference M of magnetic quantum numbers, called multiquantum coherences (M-order of coherence):

$$\rho(\tau) = \exp\{-iH_{eff}\tau\}\rho_{eq}\exp\{iH_{eff}\tau\} = \sum_M \rho_M(\tau), \quad (4)$$

$$\rho_M(\tau) = \sum_{Q=M}^{Q=N}\sum_{\{i\}}\sum_p g_{QMp\{i\}}(\tau)\left|QMp\{i\}\right\rangle,$$

where $\left|QMp\{i\}\right\rangle$ is the basis operator in which Q single-spin operators form a product linking Zeeman states differing by M units. $\{i\}$ are the numbers of the lattice nodes occupied by a given cluster. Thus, $\{i\}$ here is essentially a multi-index. Summing over $\{i\}$ implies summing over both the set of clusters and the set of spins within each cluster. The summed expression depends only on the differences of the coordinates it is given. That is, there is no dependence on one of the coordinates. Setting this coordinate arbitrary, we obtain that the summarized expression dampens rather quickly on other coordinates. A cluster here is a group of spins for which the summarized expression is not negligibly small. The index p numbers different ground states with the same values of Q and M. N is the total number of spins in the system. The coherence arising during the preparation time τ can be labeled using the phase shift ϕ, proportional to time [4,5]. The resulting phase shift is proportional to $M\phi$, where M *is* an integer. Thus, *Q-spin* correlations are also distinguished by the number of quanta ($M \leqslant Q$) [4–6]. Further these coherences can be allowed to relax (if it is reasonable) during the time t, called the free evolution period, under the action, for example, of the secular dipole-dipole (or its same, but averaged by the momentum sequence [1]) Hamiltonian (2).

At the end of the period of free evolution, a new impulse sequence is applied to the system, changing the sign of the effective Hamiltonian (3) to the opposite one and, thus, the "time reversal" is performed [24,25], as a consequence of which the order is again pumped into the observable quantity – the single-quantum longitudinal magnetization. If necessary, the amplitude of the partial (for a given value of M) magnetization or its full magnitude without "qualification by grades" (i.e., by M) can be measured using a $\pi/2$ – pulse that rotates magnetization into the plane perpendicular to the external magnetic field.

It should be emphasized that the observation of signals of MQ-coherence is possible only under certain conditions, due to which all contributions to the coherence of a given order appear (after the recovery (mixing) period) with the same phase [4]. Due to the fundamental importance of this circumstance, let us discuss this aspect of MQ spectroscopy in detail.

The amplitude and phase of the partial magnetization are completely determined by the prehistory of the spin system development. Thus, if during the preparatory period the development of the system takes place under the action of the Hamiltonian (3) (the corresponding propagator $U(\tau)=exp(-iH_{eff}\tau))$, and during the mixing period τ' *the development* takes place under the action of some, generally speaking another Hamiltonian H'_{eff} (the corresponding propagator $V(\tau')=exp(-iH'_{eff}\tau'))$, the total magnetization amplitude is described by the expression [4]:

$$G_0(\tau,t,\tau') \propto Sp\left\{S_z\rho(\tau,t,\tau')\right\} \propto Sp\left\{S_zV^+(\tau')\times\right.$$
$$\left.\times\exp\left(-iH_d(t)U^+(\tau)S_zU(\tau)\exp\left(iH_d(t)V(\tau')\right)\right)\right\}.$$

Let us calculate the trace of this expression in the basis of the eigenfunctions of the secular dipole-dipole Hamiltonian (2), denoting them by $|i\rangle$, $|j\rangle$. Writing the complex matrix elements in the form:

$$P_{ij}(\tau) = \langle i\,U|^+(\tau)S_zU(\tau)|j\rangle;\ Q_{ij}(\tau') = \langle i\,V|^+(\tau')S_zV(\tau')|j\rangle,$$

we obtain

$$G_0(\tau,t,\tau)' \propto \sum_{i,j}P_{ij}(\tau)Q_{ji}(\tau')exp\{-i(\omega_i-\omega_j)t\}.$$

Here ω_i, ω_j are the eigenvalues (in frequency units) of the Hamiltonian (2). From the above it is clear that if the Hamiltonians controlling the development of the spin system at the preparatory period and at the mixing period are different, then the MQ-coherence created at the preparatory period will undergo only an additional transformation at the mixing period. If the operator controlling the development of the system at the mixing period is designed so that $V^+(\tau')= U(\tau)$, or it differs from $U(\tau)$ only by the phase multiplier φ, i.e. $V^+= exp(-i\varphi S_z)$ $U\,exp(i\varphi S_z)$, which is the situation realized by means of time reversal, the observed signal acquires the form of a Fourier series of coherences of different order [4]:

$$G_0(\tau,t,\tau)' \propto \sum_n \sum_{i,j} |P_{ij}|^2 \exp(in\varphi)\exp\{-i(\omega_i - \omega_j)t\}.$$

Thus, under the above developments, each of the partial coherences includes contributions from all coherences of a given order, differing from its neighbors in phase by $\pm\varphi$.

3. GROWTH DYNAMICS AND EVOLUTION OF CLUSTERS OF COHERENT STATES

In the proposed work we assume to consider only the direct and reverse influence on the nuclear spin system of the non-secular Hamiltonian (3) leading to the development of spin correlations. That is, the effect on the spin system is assumed to be two-stage: the preparatory period is replaced directly by the mixing period after time reversal. A possible intermediate period of free evolution (relaxation) between these stages is absent [4–6]. Moreover, we will not consider here the processes of degradation of coherent states (decoherentization processes). We will consider in general, not taking into account the possible separation by "quantumness", M. The restrictions put forward will allow us to study in a pure, though somewhat idealized form, the dependence of the rate of development of correlated clusters on the time of the preparatory period.

We will further consider the process of correlation expansion as a process of merging (aggregation) of clusters. As noted in textbooks [26]- "aggregation processes are ubiquitous: from milk souring and blood coagulation to star formation by gravitational accretion". It should be noted that in describing aggregation processes the concepts and methods of nonequilibrium statistical mechanics are widely used and many of its basic concepts, such as scaling, phase transitions, etc., are realized.

The description of aggregation relies on an infinite set of basic kinetic equations describing the evolution of the cluster mass distribution $c_k(t)$. It is important for us that if all "monomolecular units" have the same mass, the symbol k becomes simply the number of particles in the corresponding cluster and the equation below [26] becomes an equation for the distribution over the number of particles in the cluster:

$$\frac{dc_k}{dt} = \frac{1}{2}\sum_{i+j=k} D_{ij}c_i c_j - c_k \sum_{i\geq 1} D_{ik}c_i. \qquad (5)$$

Let us list the main assumptions underlying equation (5), [26]:

1. Spatial homogeneity. The system is assumed to be well mixed, so that the probabilities that reactants in close proximity to each other factorize into the product of single-particle densities is a mean-field approximation.
2. Only "pairwise" cluster interactions are assumed.
3. Mass (number of particles in a cluster) is the only dynamical variable. The shape of the cluster is immaterial for evolution.
4. thermodynamic limit: the system is large enough to neglect the influence of discretization.

The mean-field approximation is usually asymptotically accurate in the physical case of three dimensions [26]. The basic kinetic equation (5) is an extremely complex infinite set of interdependent differential equations, which are solved only for a few special kinds of $D_{i,j}$ kernels. The solution was first studied by Smoluchowski [21] for kernels $D_{i,j}$=const. In general, however, the kind of kernel $D_{i,j}$ is unknown. Sometimes it is tried to determine it from the obtained experimental data.

In the case of continuous distribution, when the sizes of particles involved in aggregation processes are continuous variables the discrete system (5) can be replaced by an integro-differential equation:

$$\frac{\partial f(k,t)}{\partial t} = \frac{1}{2}\int_0^k D(k-y,y)f(k-y,t)f(y,t)dy - \int_0^\infty D(k,y)f(x,t)f(y,t)dy \qquad (6)$$

The operator D *is* called the coagulation/ aggregation kernel. It describes the rate at which particles of size k_1 coagulate with particles of size k_2. An analytical solution to equation (6) exists by now for three kinds of kernel: D= const, $D = k_1 + k_2$, $D = k_1 \cdot k_2$. For each of the listed fixed kernel functions there exists a single solution of this equation [27].

Further we will consider an integro-differential equation of the type (6) with a constant kernel (constant equal to $D = p$). Then, equation (6) takes the form [22]:

$$\frac{\partial f(k,t)}{\partial t} = -pf(k,t) + p\int_0^k f(k',t)f(k-k',t)dk'. \qquad (7)$$

Here the distribution function is normalized by the condition $\int_0^\infty f(k,t)dk = 1$ p is the aggregation rate constant. We emphasize that, as we assume here, it does not depend on the size of associating clusters and, consequently, on the number of particles

in the cluster. For the convenience of the reader, the solution of equation (7) is given in the Appendix and has the form:

$$f(k,t) = \frac{1}{K}\exp(-\frac{k}{K}). \quad (8)$$

Here $K = \int_0^\infty kf(k,t)dk$ is the average number of particles in the cluster at a given time. Note that the solution (8) of equation (7) is valid at times $t \gg 1/p$ and at these times the above solution is automodelic [22].

The automodel solution does not depend on the initial conditions and is "self-similar" when evolving in time. Substitution of (8) into (7) further gives:

$$\frac{dK}{dt} = pK, \quad (9)$$

That entails, in general (if the parameter p does not depend on time), a simple exponential growth of the average number of correlated spins in the sample with time, observed experimentally under the conditions described at the beginning of this section of the paper in [17–20].

It follows from our [15,16] treatment of experimental results obtained in [17–20] that for crystals of adamantane ($C_{10}H_{16}$) and calcium fluoride (CaF_2), which have quite different crystal structures, the growth of the number of correlated spins is very well described by an exponential dependence:

$$N(t) = A_e\exp\{a_e t\}, \quad (10)$$

and

$$a_e = 0.3(M_2)^{1/2}. \quad (11)$$

For adamantane, the parameters found [15,16] by the least squares method are: $A^{(A)}{}_e = 3.24$, $a_e = 0.0083$ (1/μsec). The second moment of adamantane, was calculated in [28]: $(M_2)^{1/2} = 4.19$ kHz. Unfortunately, for calcium fluoride, it is not possible to determine the numerical values of the constants a_e and A_e directly based on the experimental results of [20], because the experiment in [20] was performed on a single-crystal sample and the crystal orientation is not specified. Meanwhile, the second moment in CaF_2 single crystals depends very significantly on the orientation of the crystal with respect to the external magnetic field [23]. However, if we associate the exponent with the Lyapunov exponent, the value of the constant a_e for at least three main orientations of the external magnetic field agrees well [29] with formula (11).

4. CONCLUSION

Above we have considered the growth processes of correlated spin clusters under ideal conditions, when nothing prevents their growth. However, in principle, there are many reasons causing loss of coherence and, thus, degradation of clusters of correlated spins. The study of these processes is very important for understanding/researching quantum information propagation processes. This is one of the reasons why very often in the intervals between the preparatory period and the mixing period in the standard MQ NMR technique [4] include a period of free evolution. During this interval, the system evolves under the influence of the usual dipole-lipole interaction (2). In order to investigate the coherence loss processes, the standard MQ NMR technique was significantly modified for the first time in [30]. The declared purpose of the modification is to investigate the question: "How far quantum information can be transmitted in the presence of gates of finite (and experimenter-controlled) "precision"?. In other words, the authors investigated the question: how large a cluster of correlated spins can grow under such conditions. In this regard, the authors [31,32] observed the growth of clusters of correlated spins by introducing a controlled perturbation to the Hamiltonian (2) that creates them. As expected [30,31], the maximum cluster size in such a situation will be bounded, with clusters of maximum size being in a state of dynamical equilibrium with their surroundings. If the initial cluster size is larger than its equilibrium value, it decreases under the action of the perturbative Hamiltonian (according to the authors [29,30]), while the unperturbed Hamiltonian leads only to an unbounded growth of the cluster size. The above equilibrium cluster size, according to the authors, decreases with the increase of the perturbation intensity. All of the above, in accordance with the concept of the papers [30, 31], means the localization process according to Anderson [32] in spite of the actually infinitely high temperature of the spin system (see formula (*2a*)).

In connection with the above, it is reasonable to note that the approach to the above problems

developed in the present work opens new possibilities for studies of the propagation of correlated states and their possible degradation in the spin system, including possible localization. In particular, one can (and probably even should) assume that the aggregation rate constant p from equation (6) depends on time, which seems to have nontrivial consequences.

Finally, we note that the present study can be useful both for other sections of spectroscopy [33] including femtosecond spectroscopy) [34] and for applied structural studies [35–37].

ACKNOWLEDGEMENTS

We thank V. E. Zobov and V. S. Posvyansky for helpful discussions and comments.

FUNDING

This work was performed within the framework of the state assignment of the Ministry of Science and Higher Education of the Russian Federation (topic # 122040500060–4).

This work was financed from the budget of the Federal Research Center of Chemical Physics named after N. N. Semenov, Russian Academy of Sciences, (Moscow). N. N. Semenov Federal Research Center for Chemical Physics of the Russian Academy of Sciences, (Moscow).

APPENDIX

Consider the original equation

$$\frac{\partial f(k,t)}{\partial t} = -pf(k,t) + p\int_0^k f(k',t)f(k-k',t)dk'. \quad \text{(App. 1)}$$

normalized

$$\int_0^\infty f(k,0)dk = 1; p - \text{any}. \quad \text{(App. 2)}$$

Let's

$$g(s,t) = \int_0^\infty f(k,t)\mathrm{e}^{-sk}\,dk; \quad \text{(App. 3)}$$

Typically, the Fourier transform is used in the form:

$$\frac{\partial g(i\omega,t)}{\partial t}\Big|_{\omega=0} = -K(0)\exp(pt). \quad \text{(App. 4)}$$

If we put $f(k, t)=0$ at $k<0$ then at $s = i\omega$ the difference between (App. 4) and (App. 3) will be only in the multiplier $1/\sqrt{2\pi}$. Thus, taking into account the convolution theorem [36], we obtain Eq:

$$\frac{\partial}{\partial t}g(s,t) = -pg(s,t) + pg^2(s,t); \quad \text{(App. 5)}$$

This equation is easy to solve:

$$g(i\omega,t) = \frac{g(i\omega,0)}{g(i\omega,0) - (g(i\omega,0)-1)e^{pt}}. \quad \text{(App. 6)}$$

Then it follows from the solution of (App. 6) that $g(0, t) = 1$ and finally we obtain:

$$f(k,t) = \frac{1}{2\pi}\int_{-\infty}^{\infty} g(i\omega,t)\exp(i\omega k)d\omega. \quad \text{(App. 7)}$$

Let us show that the function $f(k, t)$ from (App. 7), where $g(i\omega,t)$ is written in the form (App. 6) under condition tp>>1 has the following form

$$f(k,t) = \frac{1}{K}\exp(-\frac{k}{K});$$

$$K \equiv K(t) = \int_0^\infty kf(k,t)dk. \quad \text{(App. 8)}$$

Let us differentiate $g(i\omega,t)$ from (App. 3) by ω and put $\omega = 0$. Then

$$\frac{\partial g(i\omega,t)}{\partial t}\Big|_{\omega=0} = -\int_0^\infty kf(k,t)dk = -K(t). \quad \text{(App. 9)}$$

On the other hand, by differentiating $g(i\omega,t)$ from (App. 6) and putting $\omega=0$ we obtain,

$$\frac{\partial g(i\omega,t)}{\partial t}\Big|_{\omega=0} = -K(0)\exp(pt) \quad \text{(App. 10)}$$

Comparing (App. 9) and (App. 10) we find:

$$K(t) = K(0)\exp(pt). \quad \text{(App. 11)}$$

Since $\int_0^\infty f^2(k,t)dk < M = 1$ and provided that $\int_0^\infty f^2(k,t)dk < M$, where M *is* not too large, we can assume that $g(i\omega,t)$ is close to 1 only in the neighborhood of 0. Therefore, in formula (App. 6) at tp>>1 *we should* take into account the following term in the expansion of $g(i\omega,0)$ at small ω. We obtain

$$g(i\omega,0) \approx 1 - K(0)i\omega \quad \text{(App. 12)}$$

Thus, the formula (App. 6) for $g(i\omega,t)$ at small ω can be rewritten in the form

$$g(i\omega,t) \approx \frac{1 - i\omega K(0)}{1 - i\omega K(0) + i\omega K(0)e^{pt}}. \quad \text{(App. 13)}$$

Since ω is small, we finally obtain

$$g(i\omega,t) \approx \frac{1}{1 + i\omega K(0)e^{pt}}. \quad \text{(App. 14)}$$

Now, using (App. 11), the function $f(k, t)$ using the inverse Fourier transform of the function $g(i\omega,t)$ from (App. 14) can be rewritten as

$$f(k,t) \approx \frac{1}{2\pi}\int_{-\infty}^{\infty} \frac{exp(i\omega k)}{1 + i\omega K(t)} d\omega. \quad \text{(App. 15)}$$

Having calculated this integral (for example, with the help of tables [38]) we obtain the relation (8).

REFERENCES

1. *Heberlen W., Mehring M.* High-resolution NMR in solids. Selective averaging High-resolution NMR spectroscopy in solids. Mir, Moscow, 1980.
2. *Ivanov Yu. N., Provotorov B. N., Fel'dman E. B.*// Zh. Eksp. Teor. Fiz. 1978. Vol. 75. P. 1847.
3. *Erofeev L. N., Shumm B. A., Manelis G. B., //* Zh. Eksp. Teor. Fiz. 1978. Vol. 75., P. 1837.
4. *Baum J., Munovitz M., Garroway A. N., Pines A.*// J. Chem. Chem. Phys.1985. Vol. 83. P. 2015. https://doi.org/10.1063/1.449344
5. *Munovitz M., Pines A.*//Adv.Chem.Phys. 1987. Vol. 66. P. 1.
6. *Ernst R., Bodenhausen J., Vokoun A.* NMR in one and two dimensions. M.: World, 1990.
7. *Wang P.-K., Ansermet J.-P., Rudaz S. L., Wang Z., Shore S., Slichter Ch. P., Sinfelt J. M.*// Science. 1986. Vol. 234. P. 35. https://doi.org/10.1126/science.234.4772.35
8. *Baumand J., Pines A.*//J. Am. Chem. Soc. 1986. Vol. 108. P. 7447.
9. *Doronin S. I., Fedorova A. V., Fel'dman E. B., Zenchuk, A. I. //* J. *Chem*. Chem. Phys. 2009. Vol. 131. P. 104109; https: //doi.org/10.1063/1.3231692
10. https://www.nobelprize.org/prizes/chemistry/2002/8873-the-nobel-prize-in-chemistry-2002-2002-4
11. *Preskill D.* Quantum information and quantum computing Vol. 1. M.:- Izhevsk: SIC Regular and Chaotic Dynamics 2008.
12. *Zobov V. E., Lundin A. A. //* ZHETF. 2020. Vol. 158. No. 2. P. 300; https: //doi.org/10.31857/S0044451020080076
13. *Domínguez F. D., Rodríguez M. C., Kaiser R., Suter D., Álvarez G. A.*//Phys. Rev. A. 2021. Vol. 104. P. 012402; https://doi.org/10.1103/PhysRevA.104.012402
14. *Zobov V. E., Lundin A. A. //* ZHETF. 2022. Vol. 162. No. 11. P. 1; https: //doi.org/10.7868/S0044451000000000.
15. *Zobov V. E., Lundin A. A.*// ZHETF. 2006. T.130. P. 1047.
16. *Zobov V. E., Lundin A. A.*//Chemical Physics. 2008. T.27. P. 18.
17. *Krojanski H. G., Suter D.*//Phys.Rev.Lett. 2004. Vol. 93. P. 090501 https://doi.org/10.1103/PhysRevLett.93.090501.
18. *Krojanski H. G., Suter D.*//Phys.Rev.Lett. 2006. Vol. 97. P. 150503 https://doi.org/10.1103/PhysRevLett.97.150503.
19. *Krojanski H. G., Suter D.*//Phys.Rev.A. 2006. Vol. 74. P. 062319 https://doi.org/10.1103/PhysRevA.74.062319.
20. *Cho G., Cappelaro P., Cory D. G., Ramanathan C.* //Phys. Rev. B. 2006 Vol. 74. P. 224434; https://doi.org/10.1103/PhysRevB.74.224434
21. *Smoluchovwski M. V.* //Zs. Phys. 1916. Vol. 17. P. 585.
22. *Smirnov B. M.*, Physics of Fractal Clusters, M: Nauka, 1991.
23. *Abraham A.* Nuclear magnetism. Chapters. 4, 6,10. Moscow: Izd. of Foreign Literature, 1963.
24. *Schneder R. H., Schmiedel H.* //Phys.Lett.A.1969. Vol. 30. P. 298; https://doi.org/10.1016/0375–9601(69) 91005–6Get rights and content
25. *Rhim W. K., Pines A., Waugh J. S. //* Phys.Rev.B. 1971. Vol. 3. P. 684; https: //doi.org/10.1103/PhysRevB.3.684
26. *Krapivsky P., Redner S., Ben-Naim E.* A kinetic view of statistical physics. M; Scientific World. 2012.
27. Collection: *Fractals in Physics*. Proceedings of the VI International Symposium on Fractals in Physics (ICTP, Trieste, Italy, 1985. Part VI. M: Mir, Moscow, (1988).
28. *Levy D. H., Gleason K. K.. //* J. Phys.Chem. 1992. Vol. 96. P. 8126.
29. *Bodneva V. L., Lundin A. A. //* ZhETF 2013. Vol. 143, No. 6, P. 1217; https: //doi.org/10.7868/S0044451013060220.
30. *Alvarez G. A., Suter D.* //Phys. Rev. Lett. 2010. V.104, P. 230403 https://doi.org/10.1103/PhysRevLett.104.230403.
31. *Alvarez G. A., Suter D., Kaiser R.* //Science. 2015. Vol. 349. P. 846. https://doi.org/doi 10.1126/science.1261160.

32. *Anderson P. W.* Basic Notions of Condensed Matter Physics, The Benjamin/Cummings Publishing Company, Inc. Advanced Book Program 1984.
33. *Lundin A. A., Zobov V. E.*// Chemical Physics. 2021.T.40. No. 9. P. 41; https: //doi.org/10.31857/S0207401x21090077
34. *Umansky S. Ya. et al.* // Chemical Physics. 2023. Vol. 42. No. 4. P. 31 https: //doi.org/10.31857/S0207401X23040143
35. *Kirilov V. E. et al.* // Chemical Physics. 2023. VOL. 42. NO. 11, P. 39. https: //doi.org/10.31857/S0207401X23110043
36. *Morozov E. V., Ilyichev A. V., Buznik V. M.* // Chemical Physics. 2023 Vol. 42. no. 11, P. 54. https: //doi.org/10.31857/S0207401X23110067
37. Shushin A. I., Umansky S. Y., Chaikina Yu.A. // Chemical Physics. 2023, Vol. 42. No. 12. P. 75. https: //doi.org/10.31857/S0207401X23120105
38. *Ditkin V. A., Prudnikov A. P.* Integral transformations and Operational calculus. M: Izd. of Phys.-Mat. literature, 1961.

ADVANCES IN CHEMICAL PHYSICS, 2025, Vol. 44, No. 1, pp. 22–30

EFFECT OF EXTERNAL FACTORS ON PHYSICOCHEMICAL CONVERSIONS

KINETICS OF THE REACTION OF HYDROGEN EVOLUTION ON STEEL IN A HYDROCHLORIC ACID SOLUTION CONTAINING CORROSION INHIBITORS

© 2025 Ya. G. Avdeev*, T. A. Nenasheva, A. Yu. Luchkin, A. V. Panova, A. I. Marshakov, and Yu. I. Kuznetsov

Frumkin Institute of Physical Chemistry and Electrochemistry, Russian Academy of Sciences, Moscow, Russia

**e-mail: avdeevavdeev@mail.ru*

Received February 23, 2024

Revised March 11, 2024

Accepted March 20, 2024

Abstract. The kinetics of cathodic reduction of hydrogen on low-carbon steel in 2 M HCl (t = 25 °C) containing corrosion inhibitors – catamine AB and IFKhAN-92 – was studied. The main rate constants for the stages of hydrogen gas evolution and the introduction of hydrogen atoms into steel are determined. The additions of catamine AB and IFKhAN-92 inhibited the cathodic reduction of hydrogen and its permeation into steel in an HCl solution. The most effective inhibitor of hydrogen absorption is IFKhAN-92. The inhibitory effect of this compound is due to a decrease in the ratio of the hydrogen concentration in the metal phase to the degree of hydrogen filling of the surface. The reduction of hydrogen concentration in the volume of metal by IFKhAN-92 addition determines the preservation of the plastic properties of steels during corrosion in HCl solutions. The high efficiency of IFKhAN-92, as an inhibitor of cathodic reduction of hydrogen and its absorption, is the result of chemisorption of this compound on the surface of the steel and the formation of a polymolecular protective layer.

Keywords: *acid corrosion, corrosion inhibitors, hydrogen permeation into metal, triazole, low-carbon steel, high strength steel, hydrochloric acid*

DOI: 10.31857/S0207401X250103e9

1. INTRODUCTION

Earlier [1] we studied the effect of nitrogen-containing organic corrosion inhibitors (CIs) – catamine AB and IFKhAN-92 on the kinetics of cathodic release and hydrogen introduction on steel in sulfuric acid solution. These substances were shown to be effective inhibitors of both the corrosion process and hydrogenation of steel. The absorption of hydrogen by an array of steel can significantly reduce its mechanical characteristics, making the metal brittle. Molecular hydrogen is formed through the adsorption stage of atomic hydrogen, which partially penetrates into the metal volume. Theoretical aspects of atomic hydrogen adsorption on metallic materials of different nature are discussed in [2–6]

Hydrochloric acid solutions are used in many technological processes. The influence of CIs on the corrosion process is widely studied, but when a steel structure comes into contact with aqueous acid solutions, in addition to corrosion damage, metal hydrogenation may occur, which will affect the mechanical properties of the material. This is especially important for metal structures operating under load (gas and oil pipelines, etc.). Few studies [7–9] have shown that nitrogen-containing organic CIs in acidic media inhibit the rate of hydrogen introduction into steel.

In connection with the above, it seems important to reveal the regularities of the influence of nitrogen-containing organic CIs on the kinetics of cathodic release and introduction of hydrogen into steel in hydrochloric acid solutions. Two previously studied CIs, catamine AB and IFKhAN-92, were chosen for the present study.

2. EXPERIMENT

2.1 Materials

As working electrodes, samples from low-carbon steel (composition, % by mass: 0.05 C, 0.03 Si, 0.38 Mn,

0.09 Ni, 0.04 S, 0.035 P, 0.05 Cr, 0.15 Cu and 0.16 Al) and from high-strength steel (composition,% by mass: 0.7 C, 1.52 Si, 0.52 Mn and 0.3 Cr) were used.

Aqueous 2 M HCl solution was used as a background electrolyte, which was prepared from concentrated acid of b.h. grade and distillate. Deaerated solutions with argon were used in electrochemical studies. Corrosion tests were carried out with free access to air. As retarders of steel corrosion we used commercially available product – catamine AB, which is a mixture of alkylbenzyl dimethylammonium chlorides ($[C_nH_{2n+1}N^+(CH_3)_2CH_2C_6H_5]Cl^-$, where n = 10–18) and inhibitor IFKhAN-92 (derivative of 3-substituted 1,2,4-triazole). It was previously shown [1] that the maximum effect is achieved when the concentration of the mixed inhibitors in H_2SO_4 solution is 5 mM. Due to the low solubility of IFKhAN-92 in the acid solution, it was introduced in the form of a concentrated ethanol solution, with the concentration of ethanol in the etching solution being 0.24 mol/L.

All experiments were performed at room temperature (25 ± 1 °C).

2.2 Methods

2.2.1 Bipolar electrode (membrane) method

The rate of hydrogen introduction into the metal was measured in a Devanathan-Stachursky cell [10, 11]. Membranes made of low-carbon steel with a thickness of 0.1 mm and a working surface area of 4.25 cm^2 were used. The technique of preparing the working electrode and conducting the experiment are described in detail in [1].

2.2.2 IPZ analysis method

The reaction of cathodic hydrogen release on iron in acidic media proceeds by the mechanism of discharge – chemical recombination, coupled rate control or slow discharge – irreversible chemical recombination [1, 12, 13]. The IPZ analysis method allows us to calculate the constants of the main stages of cathodic discharge and hydrogen introduction into steel using experimental data: the cathodic polarization curve and the dependence of the current of hydrogen introduction into the metal on the potential [12]. IPZ analysis can also be applied in cases when a part of the electrode surface is blocked by some adsorbed substance, such as CIs [8]. In this case, it is assumed that the discharge of H^+ ions$^+$ occurs on the metal surface not occupied by adsorbed atomic hydrogen, the introduction of a corrosion inhibitor into the solution does not change the mechanism of the cathodic reaction

To calculate the rate constants of the $H^+(k_{1,i})$ ion discharge stage, chemical recombination of hydrogen atoms (k_r), kinetic-diffusion constants (k), as well as the degree of hydrogen filling of the electrode surface (θ_H) and the concentration of diffusion-mobile hydrogen in the metal phase (C_H^s.), we used a variant of the IPZ analysis method, which is described in detail in [1].

2.2.3 Electrochemical impedance spectroscopy

The CIs adsorption studies were carried out by electrochemical impedance spectroscopy (**EIS**) in a three-electrode cell on a rotating disk electrode (n = 1000 rpm) made of mild steel with a working area of 0.64 cm^2.

The degree of surface filling with inhibitor (θ_{inh}) was determined by the formula:

$$\theta_{inh} = \frac{C_{dl}^0 - C_{dl}}{C_{dl}^0 - C_{dl}'}, \quad (1)$$

where C_{dl}^0, C_{dl} and C_{dl}' – are the capacitance of the double electric layer of the steel electrode in the background solution, in the inhibited solution and under the conditions of the limiting degree of adsorption of the inhibitor on the metal, respectively.

2.2.4 Gravimetric method

The corrosion rate of high-strength steel was determined by mass loss of samples with a working surface area of 17.6 cm^2:

$$\rho = \Delta m S^{-1} \tau^{-1}, \quad (2)$$

where Δm is the change in mass of the specimen; S is the area of the specimen, τ is the duration of corrosion tests.

The effectiveness of inhibitors was evaluated by the value of the degree of inhibition

$$Z = (\rho_0 - \rho_{inh})\rho_0^{-1} \cdot 100\%, \quad (3)$$

where ρ_0 and ρ_{inh} are the corrosion rates in the background solution and in the solution with the studied additive, respectively.

2.2.5 Determination of the amount of hydrogen absorbed by the metal by vacuum extraction method

The hydrogen concentration in the volume of high-strength steel (C_H^v.) was determined by vacuum extraction. After corrosion tests, the sample was placed in a vessel from which air was evacuated to a residual pressure of $1.33 \cdot 10^{-4}$ Pa, and heated to a temperature t = 500 °C. The amount of hydrogen released during heating of the sample in vacuum was estimated by the pressure change over 10 min (P_{total}) measured by a McLeod manometer at constant volume of the vacuum part of the system. The pressure of released hydrogen (P_{H2}) was calculated from the change in total pressure (P_{total}) by the formula:

$$P_{\text{H}_2} = P_{\text{total}} - P_{\text{correct}}, \quad (4)$$

where $P_{\text{correct.}}$ is the correction of the idle experience.

The molar concentration of hydrogen atoms in the steel volume was calculated by the formula:

$$C_H^v. = F P_{\text{H2}} V^{-1} \quad (5)$$

where F *is* a constant related to the volume of the analytical part of the unit; V is the volume of the steel sample.

The values of hydrogen concentration in the volume of metals are given corrected for metallurgical hydrogen, which for high strength steel is $2.4 \cdot 10^{-6}$ mol/cm^3.

2.2.6 Determination of the degree of protection of steel against hydrogenation

The effectiveness of inhibitor action was determined using the values of subsurface concentration of diffusible mobile hydrogen C_H^v. (method 2.2.2).

$$Z_H^s. = [(C_H^s. - C_{H,inh}^s) C_H^s.{}^{-1}] 100\%, \quad (6a)$$

and molar concentration of hydrogen atoms in the steel volume (C_H^v.) (Method 2.2.5.)

$$Z_H^v. = [(C_H^v. - C_{H,inh}^v) C_H^v.{}^{-1}] 100\%, \quad (6b)$$

where C_H^s. and $C_{H,inh}^s$ are the subsurface concentrations of diffusively mobile hydrogen in the background solution and in the inhibited solution, respectivel; C_H^v. and $C_{H,inh}^v$ are molar concentrations of hydrogen in the steel volume after exposure in the background solution and in the inhibited solution, respectively.

2.2.7 Determination of mechanical properties of steel (ductility)

The ductility of high-strength steel was evaluated on the device NG-1-3M, comparing the number of kinks before fracture of strip samples (length – 110 mm, width – 8 mm, thickness – 0.5 mm) in the initial state (P_0) and after their exposure in the working solution of different composition (P). Plasticity of steel was determined by the formula:

$$p = \frac{P}{P_0} \cdot 100\%. \quad (7)$$

For the steel under study, the average value of P_0 = 87.

2.2.8 Voltammetric studies

Electrochemical measurements were performed on flat specimens made of high-strength steel (S = 0.16 cm^2). The sample was kept in the test solution for 30 min at a current-free potential. The sweep rate of the steel electrode potential was 0.0005 V·s^{-1}

2.2.9 X-ray photoelectron studies of steel surface

The quantitative and qualitative composition of surface layers formed by inhibitors on the surface of mild steel was analyzed by X-ray photoelectron spectroscopy (XPS) on disk electrodes with a diameter of 10 mm. For this purpose we used Auger microscope HB100 (VG, UK), equipped with an additional camera for registration of XPS spectra.

The characteristic peaks of the following elements were measured: C(1*s*), O(1*s*), Fe(2*p*), N(1*s*), and Cl(2p). The photoionization cross sections of the corresponding electron shells given in [14] were used for quantitative evaluation. The integral peak intensities were obtained after background subtraction using the Shirley method [15] and by fitting the observed peaks by Gaussian curves with the contribution of the Lorentz component. The integral areas under the peaks of C(1*s*), O(1*s*), Fe(2*p*), N(1*s*), and Cl(2p) were used to calculate the film thicknesses.

An important element of such studies is a long (up to 18 min) ultrasonic washing in distilled water or acid solutions of the surface of metal samples from CIs. During this procedure, the CI molecules held on the metal surface by physical forces are removed from the surface of the samples preliminarily aged in an inhibited acid solution. CI molecules bound

to the metal surface by chemical forces are not removed during ultrasonic surface cleaning.

IPC-PRO MF potentiostats (Cronas Ltd., Moscow, Russia) were used for electrochemical studies. A platinum electrode was used as an auxiliary electrode and a silver chloride electrode as a reference electrode. All electrode potentials are given relative to standard hydrogen electrode.

3. DISCUSSION OF RESULTS

3.1 Kinetics of cathodic release and introduction of hydrogen into iron in the presence of corrosion inhibitors

Polarization curves and dependences of the rate of hydrogen introduction into steel on the potential in hydrochloric acid solution and with additives (5 mM) of organic CIs (catamine AB and IFKhAN-92) were obtained (Fig. 1). As we can see, in the presence of CIs the cathodic current and the rate of hydrogen introduction into the metal significantly decreases.

To calculate the constants of the main stages of hydrogen release and introduction of hydrogen into the metal in media containing catamine AB and IFKhAN-92, it is necessary to know the degree of filling of the metal surface by the inhibitor itself (θ_{inh}). In 2 M HCl solutions containing CIs, the EIS method was used to determine θ_{inh}. The steady-state values of θ_{inh} calculated from Eq. (1) were 0.95 for catamine AB and 0.99 for IFKhAN-92. In all the studied solutions, both background and CI containing, applying the IPZ analysis method [1] (Fig. 1), the kinetic constants of the reaction of hydrogen release and hydrogen permeation into the metal were calculated (Table 1).

Using the values of kinetic constants, (Table 1) we calculated the degrees of hydrogen filling of the surface of cathodically polarized steel (θ_H), the values of subsurface hydrogen concentration in the metal (C^s_H.), as well as the degree of protection of steel from hydrogen absorption (Z^s_H).

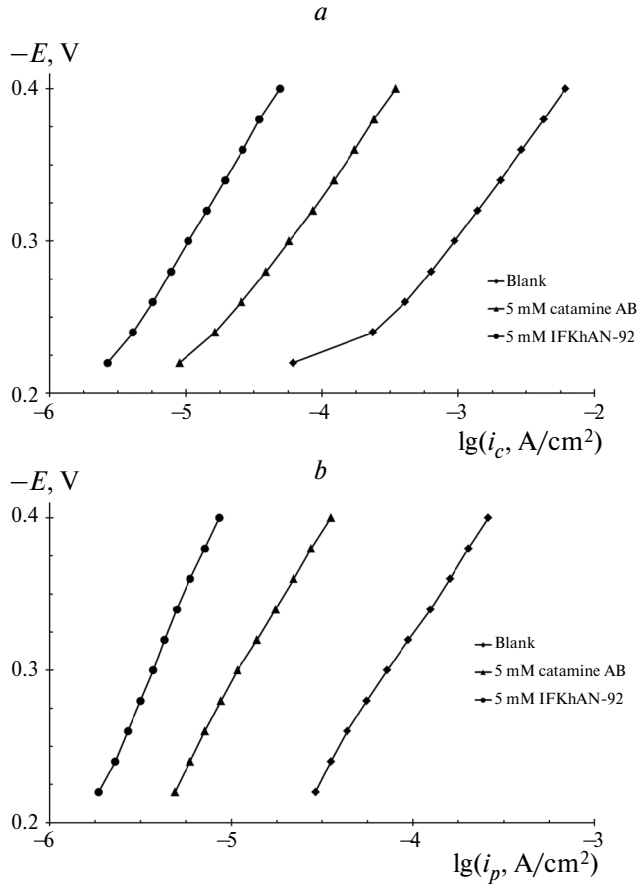

Fig. 1. Cathodic polarization curves on steel in 2 M HCl solution containing 5 mM CI (a) and plot of the rate of hydrogen permeation into steel vs. potential (b).

As follows from Table 1, the introduction of corrosion inhibitors into hydrochloric acid solution significantly reduces the hydrogen concentration in the metal. The influence of CIs on the degree of hydrogen filling of the surface is ambiguous. When 5 mM catamine AB is introduced into HCl solution, the value of θ_H increases slightly. This is due to a decrease in the hydrogen monolization constant (k_r), which can be explained by the inhibition of surface diffusion of hydrogen atoms during adsorption of inhibitor particles on the metal. In the presence of IFKhAN-92, the value of θ_H decreases because

Table 1. **The values of kinetic constants, the degree of filling of the metal surface with hydrogen atoms (θ_H), the subsurface concentration of diffusively mobile hydrogen (C^s_H.), and the degree of protection of steel against hydrogen absorption (Z^s_H.) during cathodic polarization ($E = -0.3$ V) of steel in 2 M HCl solution containing 5 mM CI**

Solution	$k_{1,i}$, mol/(cm² s)	k, cm³/mol	k_r, mol/(cm²s)	θ_H	C^s_H., mol/cm³	Z^s_H.,%
Blank	9.73×10^{-9}	3.5×10^{5}	7.5×10^{-6}	3.4	1.0×10^{-7}	–
Catamine AB	1.50×10^{-9}	2.6×10^{6}	3.0×10^{-7}	3.9	1.5×10^{-8}	85,0
IFKhAN-92	1.10×10^{-10}	2.5×10^{6}	6.0×10^{-7}	1.1	$5.5\times10^{-(9}$	94.5

the discharge rate of H^+ ions decreases to a greater extent than the rate of H atoms monolization.

The studied compounds are inhibitors not only of corrosion but also of hydrogenation, because they decrease the rate constant of H^+ ion discharge ($k_{1,\,i}$) and increase the kinetic-diffusion constant (k), i.e., they change the ratio between the values of θ_H and C_H^s. (Table 1). The latter effect is probably related to the fact that CI blocks hydrogen absorption centers and impedes the transition of H atoms from the surface to the metal phase.

Catamine AB and IFKhAN-92 are effective inhibitors of hydrogen absorption. When its 5 mM is introduced into the solution, the degree of protection of steel from hydrogen absorption is 85.0 and 94.5%. Significant decrease in the concentration of diffusion-mobile hydrogen in the metal should have a positive effect on the mechanical properties of steel, which is especially important for high-strength steels prone to hydrogen cracking under mechanical stresses.

3.2 Effect of corrosion inhibitors on the rate of electrode reactions of steel

The introduction of corrosion inhibitors into hydrochloric acid solution leads to a decrease in the rate of cathodic and anodic reactions of high-strength steel (Fig. 2). The observed Tafel slope angles of the anodic curves (b_a) in the presence of catamine AB and IFKhAN-92 are 0.15 and 0.16 V, which is higher than the value of $b_a = 0.12$ V observed in the background. For the cathodic reaction, this effect is more significant since a limiting current is observed in the presence of both CIs, although in the background the Tafel slope is $b_c = 0.16$ V. The additions of these CIs reduce the anodic dissolution rate of steel, for example at $E = -0.10$ V, by a factor of 8.8 and 15 for catamine AB and IFKhAN-92, respectively. The rate of cathodic reaction at $E = -0.30$ V decreases in the presence of these CIs by 9.4 and 13 times. It can be seen that under other equal conditions the influence

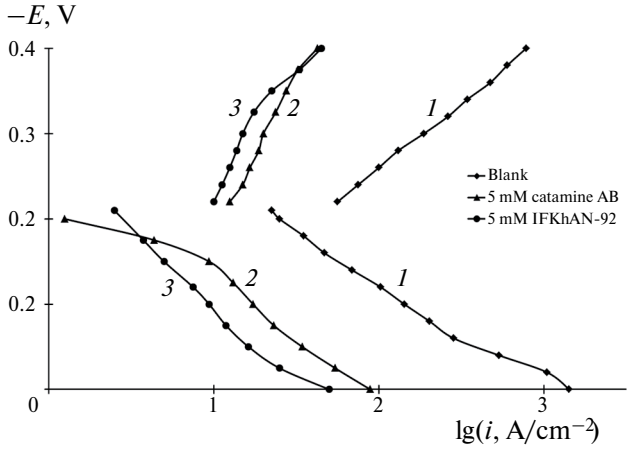

Fig. 2. Polarization curves on high-strength steel in 2M HCl (1) with 5 mM additives: catamine AB (2) and IFKhAN-92 (3).

of the inhibitor IFKhAN-92 on electrode reactions of high-strength steel is more significant than for catamine AB. The conducted corrosion studies confirm it.

3.3 Influence of inhibitors on corrosion and mechanical properties of high-strength steel

The study of corrosion of high-strength steel in 2 M HCl solution showed that these CIs reduce corrosion mass loss of metal (ρ) and hydrogen concentration in the metal volume (C_H^s.) (Table 2). As we can see, the minimum mass loss of steel samples is observed in HCl solutions containing IFKhAN-92 (Table 2). It should be emphasized that in the presence of 5 mM IFKhAN-92 the plastic properties of metal (p) practically do not change (Table 2). Consequently, IFKhAN-92 is the most effective inhibitor of corrosion and hydrogenation of steel. The obtained results agree with the data of Section 3.1, i.e., both inhibitors reduce both diffusively mobile hydrogen concentration (C_H^s.) and total hydrogen content (C_H^v.) in the metal, and IFKhAN-92, as a more effective inhibitor, allows maintaining the ductility of high-strength steel.

Table 2. **Effect of 5 mM CI on corrosion, hydrogen absorption and ductility of high strength steel in 2 M HCl.**

Solution	ρ, g/(m^2 · h)	Z_{cor},%	C_H^v., mol / cm^3	Z_H^v.,%	p,%
Blank	11,4	–	3,2 x10^{-5}	–	–*
Catamine AB	6,36	44,2	1,2 x10^{-5}	62,7	–*
IFKhAN-92	0,59	94,8	3,9x10^{-7}	87,2	100

* total loss of plasticity.

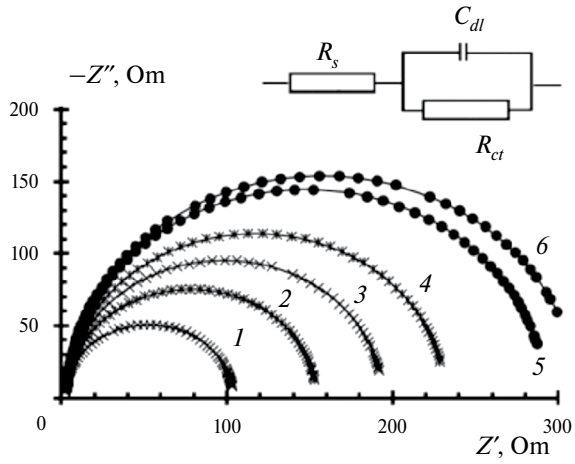

Fig. 3. Equivalent electrical circuit and Nyquist diagrams of steel electrode in 2 M HCl (*1*), taken after introduction of 0.01 mM IFKhAN-92 into the solution with exposure time (min): *2*–5, *3*–15, *4*–60, *5*–120, *6*–180

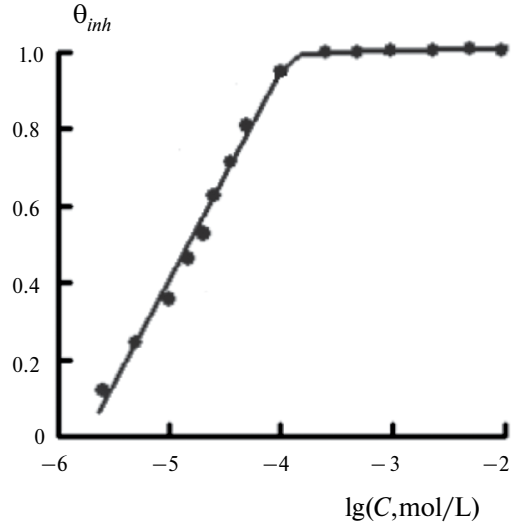

Fig. 4. Adsorption isotherm of IFKhAN-92 (1) on steel (E = –0.30 V) in 2 M HCl solution.

3.4 Nature of adsorption interaction of IFKhAN-92 inhibitor with steel surface

To understand the reasons of effective inhibition of electrode reactions of steel by the inhibitor IFKhAN-92, it is necessary to determine the nature of its adsorption interaction with the steel surface. In solutions containing IFKhAN-92, the EIS method was used to determine θ_{Inh}. The impedance spectra of the steel electrode in background and IFKhAN-92 inhibited solutions of 2 M HCl, presented as Nyquist diagrams, are perfect half circles and are described by a simple equivalent circuit that includes the capacitance of the electrical double layer (C_{dl}), the reaction resistance (R_{ct}), and the resistance of solution (R_s) (Fig. 3). In the acid solution in the presence of IFKhAN-92, the increase in the holding time of the steel electrode leads to an increase in the radius of the hodograph, which indicates the slow adsorption of the inhibitor in time. The dependence of the degree of filling of the steel surface by the inhibitor IFKhAN-92 on its concentration in the corrosive medium (adsorption isotherm) is given in Fig. 4.

As follows from Fig. 4, the adsorption of IFKhAN-92 on the surface of low-carbon steel at medium degrees of filling of the metal surface with CI obeys the Temkin isotherm:

$$\theta_{inh} = f^{-1} \ln\left(BC_{inh}\right), \qquad (8)$$

where f is the surface inhomogeneity factor, B is the adsorption equilibrium constant, C_{inh} is the concentration of inhibitor in solution. The calculated value of f is 4.25 and B is 5.31×10^5 L/mol. The free energy of adsorption ($-\Delta G_{ads}$) was determined using the relation:

$$-\Delta G_{ads} = RT \ln\left(55.5B\right) \qquad (9)$$

and equals 42 kJ/mol.

The obtained value of the free energy of adsorption of IFKhAN-92 on the surface of low-carbon steel suggests the chemisorption character of interaction between the metal surface and inhibitor molecules, since ($-\Delta G_{ads}$) > 40 kJ/mol [16]. It is this character of interaction of the inhibitor with the surface of steels that allows to obtain the highest protective effect, which we observed.

3.5 Composition and structure of protective layers formed by IFKhAN-92 inhibitor on steel surface

The XPS spectroscopy data provide valuable information on the composition and structure of protective layers formed on steel in HCl solutions containing IFKhAN-92. Based on the position of complex peaks Fe($2p_{3/2}$) and Fe($2p_{1/2}$) of the XPS spectra of iron and their satellite peaks observed at high binding energies (Fig. 5), we can assume that on the steel surface there is a layer consisting of Fe_3O_4 (E_b = 710.8 eV). The presence of oxygen of different types is indicated by the *O1s* spectrum, which can be decomposed into three peaks due to adsorbed water molecules (E_b = 533.5 eV), hydroxyl groups (531.8 eV),

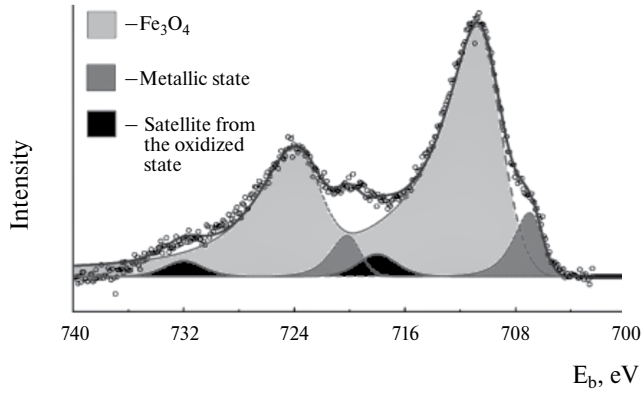

Fig. 5. Standard XPS electron spectrum of *Fe2p* (spin orbital splitting—doublet) of the steel surface, after preliminary adsorption of the inhibitor (2 M HCl + 5 mM IFKhAN-92, 24 h).

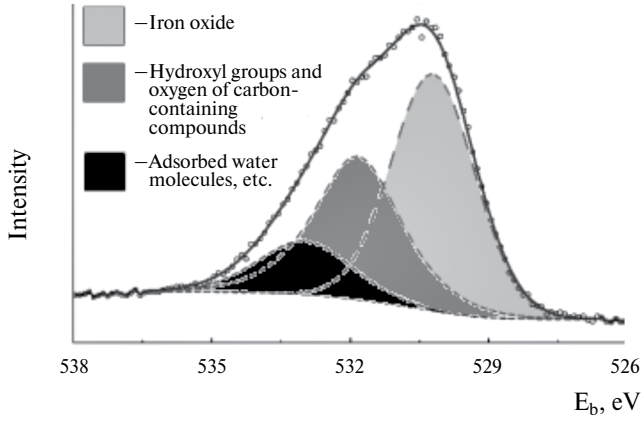

Fig. 6. XPS spectrum of *O1s* electrons from the surface of steel, after preliminary adsorption of the inhibitor (2 M HCl + 5 mM IFKhAN-92, 24 h).

and oxygen incorporated into the iron oxide lattice (530.3 eV) (Fig. 6).

Despite ultrasonic washing of the samples in distilled water, which removes physically bound inhibitor layers from the metal surface, the complex XPS spectrum of *N1s* electrons (Fig. 7) indicates the presence of an inhibitor film on the surface of steel aged for 24 h in 2 M HCl + 5 mM IFKhAN-92. The observed *N1s* spectrum can be decomposed into 2 peaks (401.4 and 399.5 eV) with the ratio ~ 1: 3 ± 0.5, and the second peak should be attributed to the nitrogen atoms of the triazole group.

Based on the quantitative ratios of XPS spectra of atoms of the steel surface aged in the inhibited HCl solution without and with subsequent ultrasonic cleaning, it can be concluded that an organic polymolecular layer with a thickness of more than 4 nm is formed on the steel. After ultrasonic cleaning of the samples, only a monolayer of inhibitor with a thickness of no more than 2 nm remains on the steel surface. Such a layer is firmly retained on the metal due to the chemisorption interaction of surface iron atoms and nitrogen atoms of the triazole cycle, which are part of the inhibitor. The inhibitor layers above the chemisorbed layer are weakly bound to it and to each other by physical interaction and are removed by such washing. The chemisorbed layer is not removed from the metal surface during ultrasonic washing and in the course of XPS studies under deep vacuum conditions. There is no peak of Cl (*2p*)-electrons in the XPS spectrum of the steel surface, which indicates the absence of chloride anions in the composition of the film. The metal surface under such a layer is oxidized to iron oxide, which occurs on the steel during washing of samples in air.

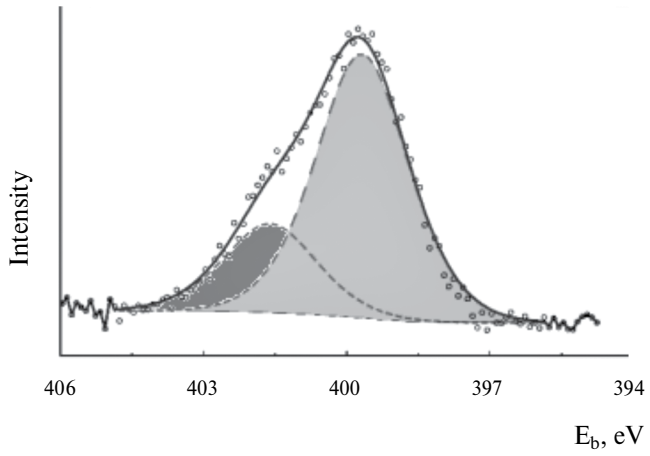

Fig. 7. XPS spectrum of N1s electrons of the steel surface, after preliminary adsorption of the inhibitor (2 M HCl + 5 mM IFKhAN-92, 24 h) followed by cleaning in an ultrasonic bath.

4. CONCLUSIONS

1. Additions of the inhibitors catamine AB and IFKhAN-92 inhibit the cathodic reduction of hydrogen and its penetration into the metal during cathodic polarization of steel in HCl solution. Using the IPZ analysis method, the kinetic constants of both processes were calculated both in the background medium and in the presence of the inhibitors. In the presence of CIs, the reaction rate of H^+ ion discharge decreases and the ratio between the degree of hydrogen filling of the surface and its concentration in the metal phase (kinetic-diffusion constant) increases. As a result, the amount of hydrogen absorbed by steel decreases. The most effective inhibitor of hydrogenation is IFKhAN-92.

2. As a result of reduction of the rate of hydrogen penetration into steel by the inhibitor IFKhAN-92, its plastic properties during corrosion in HCl solutions practically do not change and its resistance to cracking increases significantly.

3. Inhibitor IFKhAN-92 significantly reduces the rate of anodic dissolution of steel in HCl solution. This effect, in combination with inhibition of the rate of cathodic hydrogen release, determines the effectiveness of IFKhAN-92 as an inhibitor of acid corrosion of steels.

4. High efficiency of IFKhAN-92 is determined by the peculiarities of the mechanism of protective action of this inhibitor. When protecting steels in HCl solutions, this compound forms a polymolecular protective layer of triazole molecules up to 4 nm thick on the metal. The triazole monolayer directly adjacent to the metal is chemically bound to it, the overlying layers are bound to it and among themselves by physical interaction.

This work was supported by the Ministry of Science and Higher Education of the Russian Federation.

REFERENCES

1. *Avdeev Ya.G., Nenasheva T.A., Luchkin A. Yu. et al.* // Russ. J. Phys. Chem. B. 2024. Vol. 18. No 1. P. 111; https://doi.org/10.1134/S1990793124010044
2. *Rudenko E. I., Dokhlikova N. V., Gatin A. K., et al.* // Russ. J. Phys. Chem. B. 2023. Vol. 17. No. 4. P. 845; https://doi.org/10.1134/S1990793123040164
3. *Dokhlikova N. V., Ozerin S. A., Doronin S. V., et al.* // Russ. J. Phys. Chem. B. 2022. Vol. 16. No. 3. P. 461; https://doi.org/10.1134/S1990793122030137
4. *Dokhlikova N. V., Gatin A. K., Sarvadiy S. Yu. et al.* // Russ. J. Phys. Chem. B. 2021. Vol. 15. No. 4. P. 732; https://doi.org/10.1134/S1990793121040023
5. *Dokhlikova N. V., Gatin A. K., Sarvadiy S. Yu. et al.* // Russ. J. Phys. Chem. B. 2022. Vol. 16. No. 2. P. 361; https://doi.org/10.1134/S1990793122020166
6. *Dokhlikova N. V., Gatin A. K., Sarvadiy S. Yu. et al.* // Russ. J. Phys. Chem. B. 2020. Vol. 14. No. 5. P. 733; https://doi.org/10.1134/S1990793120050036
7. *Muralidharan S., Quraishi M. A., Iyer S. V. K.* // Corros. Sci. 1995. Vol. 37. P. 1739; https://doi.org/10.1016/0010-938X(95)00068-U

8. *Marshakov A. I., Nenasheva T. A., Rybkina A. A. et al.* // Prot. Met. 2007. Vol. 43. No. 1. P. 77; https://doi.org/10.1134/S0033173207010110
9. *Hari Kumar S., Vivekanand P. A., Kamaraj P.* // Mat. Today: Proceed. 2021. Vol. 36. P. 898; https://doi.org/10.1016/j.matpr.2020.07.027
10. *Devanathan M. A. V., Stachurski Z.* // Proceeding of the royals society. Ser. A. Mathematical and Physical Science. 1962. V. 270A. P. 90; https://doi.org/10.1098/rspa.1962.0205
11. *Devanathan M. A. V., Stachurski Z.* // *J. Electrochem.* Soc. 1964. Vol. 3. P. 619; https://doi.org/10.1149/1.2426195
12. *Iyer R. N., Pickering H. W., Zamanzadeh M.* // *J. Electrochem.* Electrochem. Soc. 1989. Vol. 136. P. 2463; https://doi.org/10.1149/1.2097429
13. *Popov B. N., Lee J.-W., Djukic M. B.* / Handbook of Environmental Degradation of Materials (Third Edition). Elsevier Inc. 2018. P. 133; https://doi.org/10.1016/B978-0-323-52472-8.00007-1
14. *Wagner C. D., Davis L. E., Zeller M. V., Taylor J. A., Raymond R. H., Gale L. H.* // Surf. Inter. Analysis. 1981. Vol. 3. P. 211; https://doi.org/10.1002/sia.740030506
15. *Shirley D. A.* // Phys. Rev. B. 1972. Vol. 5. P. 4709; https://doi.org/10.1103/PhysRevB.5.4709
16. *Harvey T. J., Walsh F. C., Nahlé A. H.* // J. Mol. Liq. 2018. Vol. 266. P. 160; https://doi.org/10.1016/j.molliq.2018.06.014

ADVANCES IN CHEMICAL PHYSICS, 2025, Vol. 44, No. 1, pp. 31–37

KINETICS AND MECHANISM OF CHEMICAL REACTIONS, CATALYSIS

QUASI-STATIONARY APPROXIMATION FOR ANALYZING THE GEMINATE AND BIMOLECULAR STAGES OF SINGLET FISSION IN MOLECULAR SEMICONDUCTORS

© 2025 A. I. Shushin*

Semenov Federal Research Center for Chemical Physics, Russian Academy of Sciences, Moscow, Russia

**e-mail: shushin@chph.ras.ru*

Received January 17, 2024

Revised February 07, 2024

Accepted February 20, 2024

Abstract. The work concerns the studying the accuracy of the quasi-static approximation for the calculation of the kinetics of singlet fission (SF) in molecular semiconductors. The SF is known to be accompanied by inverse TT-annihilation (TTA), which essentially controls the specific features of the SF-kinetics. The analysis of the SF-kinetics in the wide time region has been made, which covers both short times usually associated with the stage of geminate TTA and long times typical for the bimolecular TTA. The simple models have been proposed, analysis of which demonstrated good accuracy of formulas, derived within the quasistatic approximation, in the description of SF kinetics. High accuracy of interpolation formulas, which combine the obtained expressions and allow for describing the kinetics at different stages of the process, is also demonstrated. The proposed formulas are shown to significantly simplify the description of the experimental results.

Keywords*: singlet fission, triplet-triplet annihilation*

DOI: 10.31857/S0207401X250104e5

1. INTRODUCTION

Photophysical processes in molecular semiconductors are very important for many applications and especially for the development of efficient technologies concerning solar energy conversion. The mechanisms of these processes have been actively investigated for many years [1–3]. In particular, it has been found that the significant manifestation of the above-mentioned photophysical processes is usually due to efficient energy transfer processes in the investigated processes and, for example, the efficient migration and interaction of singlet (S) and triplet (T) excitons. Efficient energy transfer, in particular, essentially controls the fluorescence kinetics, as well as a number of important phenomena accompanying this process, such as up- and down-conversion of absorbed energy [1–15].

In our work we consider the kinetic features of a very important type of these processes, the spontaneous splitting of a singlet excited state (S_1^*) into a pair of triplet (T) excitons, called in the literature "singlet fission (SF)". Further in the paper we will use the abbreviation "SF" to denote the splitting of singlet state. The T-exiton pairs formed in the considered process are assumed to be able to either recapture [and react back by geminate TT annihilation (g-TTA)] or dissociate to form pairs of free T-exitons [and nevertheless annihilate by bimolecular TTA (b-TTA)]. It is important to note that in the realistic limit of low T-exiton concentrations, the geminate (short-time) and bimolecular (long-time) stages of the TTA-processes are essentially separated in time, which leads to a similar essential separation in time of the corresponding geminate (g-SF) and bimolecular (b-SF) stages of the overall SF-process.

Traditionally, SF kinetics has been studied using a kinetic scheme [1–3]:

$$S_0 + S_0 \overset{k_r}{\leftarrow} (S_0 + S_1^*) \underset{k_s}{\overset{k_{-s}}{\rightleftarrows}} [TT] \underset{k_{-e}}{\overset{k_e}{\rightleftarrows}} [T+T]. \quad (1)$$

The first stage of the SF-process is the transition (at the rate k_{-s}) from the initial state ($S_0 + S_1^*$) to the [TT]-state of a pair of interacting T excitons (hereafter referred to as the *c-state*). The evolution of the TT pairs in the [TT]-state is controlled by TTA (at the rate k_s), as well as by the dissociation into

the [T+T]-*state* (or *e-state*) of a pair of free T-exitons and recapture into the [TT]-state at the rates k_e and k_{-e}, respectively. The SF process is also accompanied by deactivation of the S_1^*-state with the velocity k_r.

Within this scheme, the geminate g-SF-stage kinetics (at short times) is described in terms of the fluorescence intensity $I_g(t)$ from the S_1^* state at times corresponding to the (short-time) g-SF-stage. As for the (long-time) bimolecular b-SF-stage, i.e., the fluorescence intensity $I_b(t)$ at long times, this part of the fluorescence arises from the splitting of S_1^*-states that are generated by the reversible bimolecular TTA reaction (in the [T+T]-state). Experimental SF kinetics is usually analyzed in terms of normalized fluorescence intensity from the S_1^*-state [1,2]:

$$y_\nu(t) = I_\nu(t)\,/I_g(0),\ .(\nu = g, b) \qquad (2)$$

In this definition, the function $I_\nu(t) = k_r n_s^\nu(t)$ represents the observed fluorescence intensity, $n_s^\nu(t)$ the concentration of excited states S_1^* at the stage v, $(\nu = g, b)$, $n_s^g(t = 0) = n_{s_i}$ the initial concentration of S_1^*-states, and $y_\nu(t)$ -the corresponding normalized populations of S_1^* -states. The normalization (2) implies the initial condition $y_g(t = 0) = 1$.

This work is devoted to analyzing the kinetic properties of the SF process (1) over a wide range of times. We will analyze it within the framework of the two-state model (TSM) [16–18], which allows us to describe quite accurately the effect of diffusive migration of T-exitons on TTA and, thus, on SF kinetics. In the TSM framework, migration effects are treated in terms of transitions between kinetically bound states: [TT]-states of interacting TT pairs and [T+T]-states of exciton pairs performing isotropic relative diffusion in three-dimensional (3D) space.

Using the proposed approach, expressions for the g-SF and b-SF kinetic dependences $y_g(t)$ and $y_b(t)$ are obtained. These expressions are combined into one interpolation formula for kinetics $y(t)$, which correctly describes SF kinetics at both small and large times. In particular, this formula allows us to describe with good accuracy the SF kinetics measured in films of rubren-containing nanoparticles [distributed in poly(vinyl-alcohol) (PVA)] [7] over a wide range of times. The derived expression for $y(t)$ predicts a marked effect of diffusion-assisted TTA in the form of SF kinetics, manifested by a smooth transition from $y_g(t)$ to $y_b(t)$ -kinetics with increasing time.

2. KINETIC MODELS OF THE SF-PROCESS

In this chapter, the kinetics of SF processes (1) in amorphous molecular semiconductors is analyzed within the framework of two models over a wide range of times, including both small times corresponding to geminate processes and large times at which SF kinetics is determined by bimolecular processes.

It should be noted that SF-processes are spin-selective (and causes, in particular, the magnetodependence of their kinetics [19]). The kinetics of such processes are described by the stochastic Liouville equation (SLE) for the spin density matrix of the system, which is a complex system of many equations describing the evolution of a large number of spin states of the system. To simplify the analysis, we consider the kinetics of SF processes in the realistic limit of fast spin-lattice relaxation (in TT pairs), usually realized in processes in amorphous semiconductors. This limit is observed due to strong fluctuations of the zero-field interaction in T excitons [20], caused by the migration of excitons through the sample volume. In the limit of fast relaxation, leading to almost complete averaging of the spin-selectivity effects, the SLS simplifies considerably, being reduced to a much smaller number of equations for functions (averaged density matrices) [20,21].

The two models mentioned can be visualized as follows:

1) The first model is a semi-empirical kinetic model based on the use of nonlinear kinetic equations, the right-hand side of which is a combination of contributions from linear terms controlling the short-time (geminate) g-SF stage of the process and nonlinear (quadratic in T-exciton concentration) terms determining the long-time (bimolecular) b-SF stage of the kinetics. This model will be used to analyze approximations and evaluate the accuracy of methods for treating process kinetics;

2) The second model is a realistic two (kinetically coupled) state (TSM) model [16–18] describing the effect of the relative motion of diffusing T excitons, which are generated by the dissociation of TT pairs born from the primary splitting of S_1^* -states at a rate k_{-s} [see (1)]

A semi-empirical kinetic model.

In a simplified formulation, the kinetic equations of the semiempirical model describing SF kinetics in accordance with the kinetic scheme (1) over a wide

range of geminate and bimolecular TTA-stage times are written as:

$$\begin{aligned} d\bar{n}_s/dt &= -(\bar{k}_r + \bar{k}_{-s})\bar{n}_s + \bar{k}_a\bar{n}_T^2 \\ d\bar{n}_T/dt &= 2\bar{k}_{-s}\bar{n}_s - k_d\bar{n}_T - 2\bar{k}_a\bar{n}_T^2. \end{aligned} \quad (3)$$

Equations (3) describe a simplified version of the SF process (3), in which the effect of [TT]-state of interacting T excitons is not taken into account.

In these equations, $\bar{n}_s(t)$ and $\bar{n}_T(t)$ are the concentrations of excited S_1^* -states and T-exitons in the sample, respectively, $\bar{k}_r$ and $\bar{k}_{-s}$ are the rate constants defined in scheme (1), k_d is the gobelite rate of T-exitons, and $\bar{k}_a$ is the rate constant of the bimolecular TTA process.

According to the kinetic scheme of the process (1), equations (3) must be solved with the initial condition:

$$\bar{n}_s(t = 0) = \bar{n}_{s_i} \text{ and } \bar{n}_T(t = 0) = 0. \quad (4)$$

In this paper we will analyze the most realistic limit of small initial concentrations n_{s_i}, defined by the inequality:

$$n_{s_i} \ll \bar{k}_{rs}/\bar{k}_a, \quad (5)$$

where $\bar{k}_{rs} = \bar{k}_r + \bar{k}_{-s}$.

It is important to note that condition (5) guarantees the smallness of both $\bar{n}_s(t)$ and $\bar{n}_T(t)$ at all times, which, in turn, results in the essential separation in time of the two stages of the SF-process described by equations (3): short-time g-SF and long-time b-SF (see below).

In what follows, it is instructive to analyze the system of equations (3) in the adiabatic (quasi-stationary) approximation based on the use of a significant difference in the characteristic times $\bar{\tau}_g = \bar{k}_{rs}^{-1}$ and $\bar{\tau}_b = (\bar{k}_a n_{s_i})^{-1}$ of the g-SF and b-SF stages (respectively) in the limit (5):

$$\bar{\theta} = \bar{\tau}_g/\bar{\tau}_b = \bar{k}_a n_{s_i}/\bar{k}_{rs} \ll 1 \quad (6)$$

In this approximation, in the lowest order of small-parameter decomposition $\bar{\tau}_g/\bar{\tau}_b \ll 1$ the SF kinetics is represented as the sum of two contributions: geminate (at small times $t < \bar{\tau}_g$) and bimolecular (at large times $t > \bar{\tau}_b$) [22] [22]:

1. *Geminate stage.* The contribution of this stage is determined from the solution of equations (3) obtained in neglecting the bimolecular TTA process (i.e., at $\bar{k}_a = 0$):

$$\bar{n}_s^g(t) = n_{s_i} e^{-\bar{k}_{rs}t},$$

$$\bar{n}_T(t) \approx 2\bar{k}_{-s}\int_0^t d\tau \bar{n}_s(\tau) = (1 - e^{-\bar{k}_{rs}t})\bar{n}_T^0. \quad (7)$$

In these expressions, $\bar{k}_{rs} = \bar{k}_r + \bar{k}_{-s}$ and $\bar{n}_T^0 = \bar{Y}_T n_{s_i}$, where $\bar{Y}_T = 2\bar{k}_{-s}/\bar{k}_{rs}$. (8)

Note that the initial concentration of T-exitons $\bar{n}_T^0$ essentially determined by their yield $\bar{Y}_T$ in the geminate SF process (at $t \sim \bar{\tau}_g$).

2. *Bimolecular stage.* The bimolecular contribution is formed in the process of adiabatic evolution of the above discussed geminate subsystem (treated by equations (3) with $\bar{k}_a = 0$). The evolution is due to nonlinear summands proportional to $\bar{n}_T^2$.

In the adiabatic approximation in the lowest order expansion in of $\bar{\tau}_g/\bar{\tau}_b \ll 1$, the evolution of $\bar{n}_s^b(t)$ is determined by the stationary version of the first of equations (3) (i.e., in which $d\bar{n}_s^b/dt = 0$):

$$\bar{n}_s^b(t) = (\bar{k}_a/\bar{k}_{rs})\bar{n}_T^2(t). \quad (9)$$

Substituting relation (9) into the second of equations (3), leads to an equation describing the kinetics of the evolution of the T-exiton concentration [22]:

$$d\bar{n}_T/dt = -k_d\bar{n}_T - 2\bar{K}_a\bar{n}_T^2, \quad (10)$$

where $\bar{K}_a = \bar{k}_a\bar{k}_r/\bar{k}_{rs}$.

In this equation $\bar{K}_a$ is the effective rate of TTA. Solving equation (10), we obtain:

$$\bar{n}_T(t) = \bar{n}_T^0/\bar{\Phi}(t), \quad (11)$$

where $\bar{\Phi}(t) = e^{k_d t} + \bar{\kappa}_a(e^{k_d t} - 1)$ and $\bar{\kappa}_a = 2(\bar{K}_a\bar{n}_T^0/k_d)$.

The corresponding concentration of states S_1^* $\bar{n}_s^b(t)$ at the bimolecular stage is determined from relation (9)

$$\begin{aligned} \bar{n}_s^b(t) &= (\bar{k}_a/\bar{k}_{rs})(\bar{n}_T^0)^2\bar{\Phi}^{-2}(t) = \\ &= (\bar{K}_a\bar{n}_{s_i}^2/\bar{k}_r)\bar{Y}_T^2\bar{\Phi}^{-2}(t). \end{aligned} \quad (12)$$

Expressions (7) and (12) for $\bar{n}_s^g(t)$ and $\bar{n}_s^b(t)$, obtained in the framework of the simple kinetic model (3), are conveniently represented in terms of the populations of S_1^*, i.e. the states at the geminate

(g-SF) and bimolecular (b-SF) stages of the process $\bar{y}_\nu(t) = n_s^\nu(t)/n_{s_i}$ ($\nu = g, b$):

$$\bar{y}_g(t) = e^{-k_{rs}t} \text{ and, } y_b(t) = \bar{y}_b^0 \bar{\Phi}^{-2}(t) \qquad (13)$$

where $\bar{y}_b^0 = (\bar{K}_a n_{s_i}/\bar{k}_r)\bar{Y}_T^2$ and $\bar{K}_a = \bar{k}_a\bar{k}_r/\bar{k}_{rs}$.

3. *Interpolation formula.* The obtained kinetic g-SF- and b-SF-functions $\bar{y}_{g,b}(t)$ can be combined into an interpolation formula for $\bar{y}(t) = n_s(t)/n_{s_i}$, describing both limits:

$$\bar{y}(t) = \left(\bar{y}_g(t) + \bar{y}_b^0\right)\bar{\Phi}^{-2}(t) = \\ = \frac{\bar{y}_g(t) + \bar{y}_b^0}{\left[e^{k_d t} + \bar{\kappa}_a(e^{k_d t} - 1)\right]^2} \quad . \qquad (14)$$

A two-state diffusion model

We will formulate the kinetic equations of a more realistic TSM separately for the geminate g-SF- and bimolecular b-SF-stages.

1. Geminate stage. In the considered TSM at the g-SF stage of the process (1), the primary splitting of the S_1^* -state, $(S_0 + S_1^*) \leftrightarrow [TT]$, is interpreted as a first-order reaction. In contrast, the second stage, $[TT] \leftrightarrow [T+T]$, is interpreted in the two-state approximation developed earlier [16–18]. In this approximation, the spatial evolution of TT pairs is modeled by transitions between two states: the intermediate [TT]-state of interacting excitons and the [T+ T]-state of freely diffusing T excitons.

In TSM, the time-dependent population of -state S_1^* $y_g(t)$ is controlled by the space-time evolution of TT pairs in [TT] and [T+ T]-states, described by the populations $\sigma(t)$ and $\rho(r,t)$ of these two states, respectively (where r is the interexciton distance). The populations satisfy the stochastic Liouville equation [19], which in the TSM is written in the form of three equations [16–18]

$$dy_g/dt = -(k_r + k_{-s})y_g + k_s\sigma, \\ d\sigma/dt = -(k_s + K_-)\sigma + S_l K_+ \rho_l + k_{-s} y_g, \qquad (15) \\ d\rho/dt = \hat{\mathbf{L}}_r \rho + (S_l^{-1} K_- \sigma - K_+ \rho_l)\delta(r - l),$$

where $S_l = 4\pi l^2$ is the area of the spherical surface of the [TT]-state with radius, l $\hat{\mathbf{L}} = D_r r^{-2}\partial_r(r^2\partial_r)$ is the radial part of the relative diffusion operator of T-exitons and $\rho_l(t) = \rho(l, t)$.

The terms proportional to $K_\pm$, represent the transitions between the [TT] and [T+ T] states [16–18]. In what follows, we consider the limit of fast thermalization of TT pairs in the [TT]-state, in which [16–18]:

$$K_\pm \to \infty \text{ and } K_+/K_- = Z_w/l^2. \qquad (16)$$

In the second of relations (16), Z_w is the partition function in the [TT]-state.

The scheme of the process (1) implies for the equations the initial condition:

$$y_g(t = 0) = 1 \text{ and } .\sigma(t = 0) = \rho(r, t = 0) = 0 \qquad (17)$$

Equations (15) must be solved with the total reflection boundary condition for $\rho(r,t)$ at:$r = l$ $\partial_r\rho|_{r=l} = 0$.

Solving equations (15) by the Laplace time transformation method, defined as $\tilde{\varphi}(\varepsilon) = \int_0^\infty dt\, \varphi(t) e^{-\varepsilon t}$, gives [16–18]:

$$y_g(t) = \frac{1}{2\pi i}\int_{-i\infty}^{i\infty} d\varepsilon \left[\varepsilon + k_{rs} - \frac{k_{-s}\kappa_s}{\varepsilon + \kappa_s + k_e + \xi_e(k_e\varepsilon)^{1/2}}\right]^{-1} e^{\varepsilon t}, \qquad (18)$$

in which, $k_{rs} = k_r + k_{-s}\kappa_s = \frac{1}{9}k_s$ is the average rate of the TTA

$$k_e = D_r l \,/\, Z_w \text{ and } \xi_e = \sqrt{l^2 k_e \,/\, D_r}. \qquad (19)$$

In formula (19), k_e is the dissociation rate of the [TT]-state (bound T-exitons), and ξ_e is a dimensionless parameter that determines the anomalous splitting of the amplitude of the geminate function $y_g(t) \sim \xi_e t^{-3/2}$ at large times due to the non-analytic behavior of the Laplace transform in time $\tilde{y}_g(\varepsilon)$ at small: $\varepsilon\tilde{y}_g(0) - \tilde{y}_g(\varepsilon) \sim \xi_e\varepsilon^{1/2}$ [16–18].

2. Bimolecular stage. The kinetics of the long-time b-SF stage is controlled by the bimolecular TTA described by equation (10):

$$dn_T/dt = -k_d n_T - 2K_a n_T^2, \qquad (20)$$

for the concentration of T-exitons $n_T(t)$, reacting at the rate [22]:

$$K_a = (4\pi D_r l)(k_r k_s)[k_{rs}(k_e + k_s) - k_{-s}k_s]^{-1}. \qquad (21)$$

As in the previously analyzed simple model (3), in the more realistic model (15), which takes into account diffusion of T-excitons, at the bimolecular

stage (at large times) the evolution of the concentration $n_s^b(t)$ can be determined in the quasi-stationary (adiabatic) approximation from a relation like (9), represented as [22]:

$$k_r n_s^b(t) = K_a n_T^2(t). \quad (22)$$

Using the solution of equation (20) and relation (22), we obtain

$$y_b(t) = y_b^0 \Phi^{-2}(t), \quad (23)$$

where, $\Phi(t) = e^{k_d t} + \kappa_a(e^{k_d t} - 1)$ as well as $y_b^0 = (K_a n_{s_i}/k_r)Y_T^2$, $\kappa_a = 2(K_a n_{s_i} Y_T)/k_d$ and $Y_T = 2(k_e k_{-s})(k_{rs} k_e + k_r k_s)^{-1}$.

3. Interpolation formula. Similar to the simplified model, the obtained g-SF- and b-SF-functions $y_{g,b}(t)$ can be conveniently combined into an interpolation formula for $y(t) = n_s(t)/n_{s_i}$ [close in form to formula (14)], reproducing the limits g-SF- and b-SF [22]:

$$y(t) = \left(y_g(t) + y_b^0\right)\Phi^{-2}(t) = \frac{y_g(t) + y_b^0}{\left[e^{k_d t} + \kappa_a(e^{k_d t} - 1)\right]^2}. \quad (24)$$

3. DISCUSSIONS OF RESULTS

The results obtained within the framework of the simplified model (3) allow us to draw important conclusions regarding the accuracy of the adiabatic approximation and, in particular, of the interpolation formula (14) obtained within this approximation. Comparison of the functions $\bar{y}(t)$, found by numerical solution of equations (3), with the approximate ones calculated using the interpolation formula (14), shows high accuracy of the formula even at relatively large values of the initial concentrations of -states $S_1^* \underline{n}_{s_i}$, corresponding to the values of $\bar{\theta} = \bar{\tau}_g/\bar{\tau}_b = (\bar{k}_a n_{s_i})/\bar{k}_{rs} < 0.2$ (Fig. 1).

The given estimates of the accuracy of the used quasi-stationary (adiabatic) approximation suggest a sufficiently high accuracy of the proposed interpolation formula derived not only in the framework of simple models of type (3) [formula (14)], but also in the realistic model (15) [formula (24)].

The high accuracy is also confirmed by the good agreement found between the theoretical SF function calculated using expression (24) and the SF function experimentally measured in films of rubren-

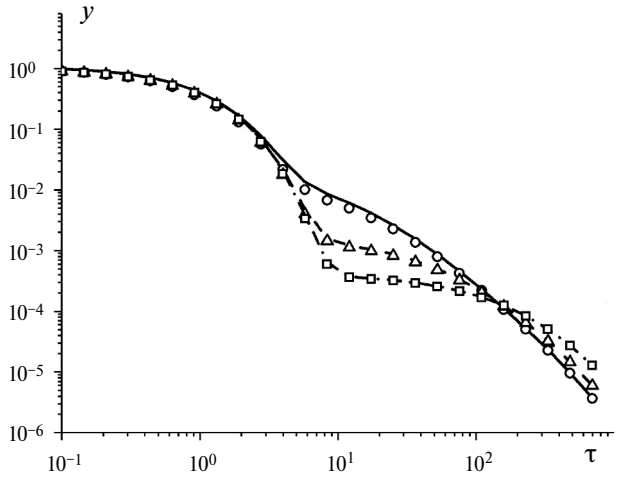

Fig. 1. Comparison of the exact dependence of the SF-kinetic function $y(\tau) = \bar{y}(\tau)$ on the dimensionless time $\tau = k_{rs}t$, obtained by numerical solution of the equations within the simple kinetic model (3) (lines), with those approximated using the interpolation formula (14) (points) for three sets of model parameters, $\bar{q}_{-s} = \bar{k}_{-s}/\bar{k}_{rs}$ $\bar{q}_d = \bar{k}_d/\bar{k}_{rs}$ and $\bar{\kappa}_a$ (defined in (11)). The three sets of parameters used, denoted as vectors $\mathbf{q} = (\bar{q}_{-s}, \bar{q}_d, \bar{\kappa}_a)$ [and the corresponding obtained functions $y(\tau) = \bar{y}(\tau)$] can be represented as: $\mathbf{q}_1 = (0.2, 0.001, 0.1)$ [solid lines and circles], $\mathbf{q}_2 = (0.1, 0.001, 0.04)$ [dashed lines and triangles], and $\mathbf{q}_3 = (0.1, 0.001, 0.01)$ [dashed lines and squares]

containing nanoparticles of 200 nm diameter [7] over a wide range of times, as shown in Fig. 2.

In the calculation of the geminate kinetic function, the parameters of the diffusion TSM model were used, which are conveniently represented as a vecto r $\mathbf{z} = (z_{-s}, z_s, z_r, z_e)$, where $z_\alpha = k_\alpha/k_{rs}$, as well as the parameters, $k_{rs} = k_r + k_{-s}\xi_e$ and the dimensionless time $\tau = k_{rs}t$. In the calculation of the bimolecular kinetic function, the initial concentration of singlet excitations n_{s_i} and the radius *l of* the [TT]-state of interacting TT pairs were variable quantities. The full kinetic curve $y(t) = n_s(t)/n_{s_i}$ shown in Fig. 2 was calculated using the interpolation formula (24) and the following parameter values: $k_{rs} = 0.37$ ns, $\mathbf{z} = (0.8, 0.16, 0.2, 0.14)$ and $\xi_e = 1.7$. The values of $l \approx 1.2$ nm and $n_{s_i} l^3 = 3.2 \cdot 10^{-4}$ were also used.

Fig. 2 also shows, to further illustrate the results, the characteristic geminate kinetic function $y_g(t)$, (dashed curve) calculated in neglecting T-exiton migration, i.e., with the same diffusion model parameters (TSM) but at $\xi_e = 0$. It can be seen that neglecting migration leads to a significant difference in the behavior of the experimental and theoretical functions $y_g(t)$.

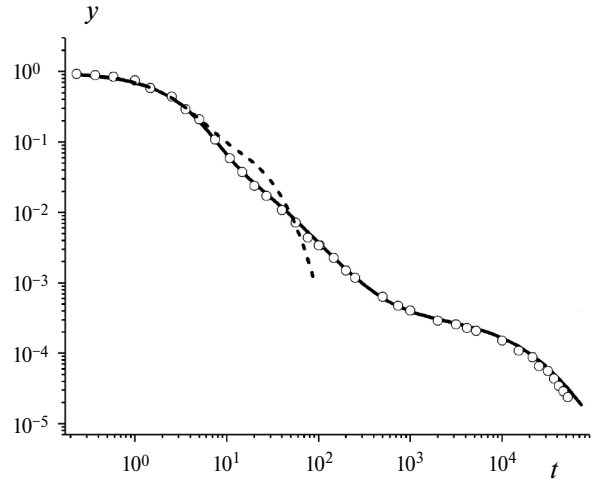

Fig. 2. Comparison of experimental SF kinetics [7] (circles) measured in films of rubren-containing nanoparticles with the (full) SF kinetic function $y(t)$, calculated using the interpolation formula (24). The characteristic geminate kinetic function $y_g(t)$, (dashed curve) calculated in neglecting T-exciton migration, i.e., for the above-mentioned diffusion model parameters (TSM) but at $\xi_e = 0$ is also shown (see Chapters 2 and 3). The function $y(t)$ was calculated with a single fitting parameter: $n_{s_i} l^3 = 3.2 \cdot 10^{-4}$. The value of $k_d = 10^{-5}$ ns is given in [7]. The other parameters were previously found by analyzing the geminate kinetics of SF processes of ordinary rubren films [14, 15]: $k_{rs} = 0.37$ нс, $\mathbf{z} = (0.8, 0.16, 0.2, 0.14)$ and $\xi_e = 1.7$

4. CONCLUSION

In this work, we analyze the accuracy of the quasi-stationary approximation for the calculation of SF-kinetic functions over a wide range of times, including both small times characteristic of the g-TTA geminate stage (which essentially controls the behavior of SF-kinetics) and large times typical of the bimolecular b-TTA stage. Simple phenomenological models of SF-processes are formulated, the analysis of which made it possible to demonstrate quite good accuracy of formulas for SF-kinetics obtained within the framework of the models. Special attention is paid to analyzing the accuracy of the proposed interpolation formulas for SF-kinetic functions. These formulas are found to describe a number of experimental results with good accuracy, reducing the calculations to the simplest algebraic operations. Particularly important are the formulas that make it possible to generalize the results to the case of realistic models, for example, describing the effect of diffusive migration of T-excitons. It is shown that the proposed generalized expressions describe with good accuracy recent experimental studies of the kinetics of SF processes in amorphous rubren films [14, 15], in which exciton migration plays an important role.

In conclusion, it should be noted that the developed method of approximate description of SF-processes allows us to analyze in detail complex effects in these processes, for example, magnetic effects [19]. The proposed approaches can be used to describe the magnetic in SF-processes of interest for practical applications.

FUNDING

This work was financially supported by the Ministry of Science and Higher Education of the Russian Federation under the State Assignment, (project No. 125012200611-5).

CONFLICT OF INTEREST

The authors of this paper declare that they have no conflicts of interest.

REFERENCES

1. *K. Miyata, F. S. Conrad-Burton, F. L. Geyer et al.* Chem. Rev. 119, 4261 (2019). https://doi.org/10.1021/acs.chemrev.8b00572
2. *D. Casanova,* Chem. Rev. 118, 7164 (2018). https://doi.org/10.1021/acs.chemrev.7b00601
3. *M. B. Smith, J. Michl,* Annu. Rev. Phys. Chem. 64, 361 (2013). https://doi.org/10.1146/annurev-phy-schem-040412–110130
4. *R. E. Merrifield.* J. Chem. Phys. 48, 4318 (1968). https://doi.org/10.1063/1.1669777
5. *A. Suna*, Phys. Rev. B. 1, 1716 (1970). https://doi.org/10.1103/PhysRevB.1.17166.
6. *A. I. Shushin,* J. Chem. Phys. 156, 074703 (2022). https://doi.org/10.1063/5.00781587
7. *D. G. Bossanyi, Y. Sasaki, S. Wang, D. Chekulaev, N. Kimizuka, N. Yanai, J. Clark,* J. Mater. Chem. C. 10, 4684 (2022). https://doi.org/10.1039/d1tc02955j
8. *A. S. Vetchinkin, S. Ya. Umanskii, Ju. A. Chaikina et al.* Russ. J. Phys. Chem. B. 16, 945 (2022). https://doi.org/10.1134/S19907931220501049
9. *A. I. Shushin, S. Y. Umanskii, Y. A. Chaikina.* Russ. J. Phys. Chem. B. 17, 860 (2023). https://doi.org/10.1134/S1990793123040176
10. *A. I. Shushin, S. Y. Umanskii, Y. A. Chaikina.* Russ. J. Phys. Chem. B. 17, 1403 (2023). https://doi.org/10.1134/S199079312306021011

11. *S. Y. Umanskii, S. O. Adamson, A. S. Vetchinkin et. al.* // Russ. J. Phys. Chem. B. 17. 346 (2023). https://doi.org/10.1134/S199079312302032X
12. *A. Ryansnyanskiy, I. Biaggio.* Phys. Rev. B. 84, 193203 (2011). https://doi.org/10.1103/PhysRevB.84.19320313
13. *T. Barhoumi, J. L. Monge, M. Mejatty et al.* Eur. Phys. J. B. 59, 167 (2007).
14. *G. B. Piland, J. J. Burdett, D. Kurunthu et al.* J. Phys. Chem. 117, 1224 (2013). https://doi.org/10.1021/jp309286v 1
15. *G. B. Pilland, J. Burdett, R. J. Dillon et al.* J. Phys. Chem. Lett. 5, 2312 (2014). https://doi.org/10.1021/jz500676c
16. *A. I. Shushin*. Chem. Phys. Lett. 118, 197 (1985). https://doi.org/10.1016/0009-2614(85)85297-017
17. *A. I. Shushin*. J. Chem. Phys. 95, 3657 (1991). https://doi.org/10.1063/1.46081718
18. *A. I. Shushin*. J. Chem. Phys. 97, 1954 (1992). https://doi.org/10.1063/1.46313219
19. *U. E. Steiner, T. Ulrich*. Chem. Rev. 89, 514 (1989). https://doi.org/10.1021/cr00091a003
20. *A. I. Shushin*. Chem. Phys. Lett. 678, 283 (2017). https://doi.org/10.1016/j.cplett.2017.04.068
21. *A. I. Shushin,* J. Chem. Phys. 151, 034103 (2019). https://doi.org/10.1063/1.509966722
22. *A. I. Shushin*. Chem. Phys. Lett. 811, 140199 (2023). https://doi.org/ 10.1016/j.cplett.2022.140199

ADVANCES IN CHEMICAL PHYSICS, 2025, Vol. 44, No. 1, pp. 38–44

KINETICS AND MECHANISM OF CHEMICAL REACTIONS, CATALYSIS

QUANTUM CHEMICAL SIMULATION OF REACTIONS IN A NANOGOLD–OXYGEN–HYDROGEN SYSTEM

© 2025 M. V. Grishin, D. T. Baimukhambetova, A. K. Gatin, S. Y. Sarvady, V. G. Slutsky*, and V. A. Kharitonov

Federal Research Center of Chemical Physics named after N. N. Semenov of the Russian Academy of Sciences. N. N. Semenov Federal Research Center for Chemical Physics, Russian Academy of Sciences, Moscow, Russia

**e-mail: slutsky@chph.ras.ru*

Received April 22, 2024

Revised May 13, 2024

Accepted May 20, 2024

Abstract. Quantum chemical calculations are performed to determine the heats of adsorption of H_2 and O_2 on the simplest electrically neutral Au_3 cluster or the negatively charged Au_3- cluster. A detailed mechanism is proposed for reaction between O_2 and (Au_3H_2) adsorbate, and the energy budget for the elementary reactions producing (Au_3O)_ and H_2O is calculated. The energy budget is also calculated for the elementary steps involved in the reaction between $(Au_3O)^-$ and H_2 producing Au_3^- and H_2O. Based on the calculated results, an explanation is proposed for the experimental data on interaction of hydrogen and oxygen with gold nanoparticles deposited on pyrolytic graphite. Since the gold nanoparticles located on graphite are negatively charged, the calculations are performed accordingly for negatively charged gold-containing particles.

Keywords: *quantum chemical simulation, nanogold, reactions H_2 and O_2*

DOI: 10.31857/S0207401X250105e3

1. INTRODUCTION

Many currently used catalysts include nanoparticles. In particular, gold nanoparticles are contained in catalysts for low-temperature oxidation of CO [1], production of vinyl acetate and vinyl chloride [2], isomerization of epoxides into unsaturated alcohols [3], hydrogenation of carbonyl [4] and nitro [5] compounds, and many other processes involving hydrocarbons.

An extended experimental study of reactions in the nanogold-oxygen-hydrogen system was performed in [6]. In the first series of experiments, gold nanoparticles 2–3 nm in size were electrodispersed [7] onto a substrate of highly oriented pyrolytic graphite (HOPG) and placed in this form in a tunneling microscope chamber, where at room temperature they were sequentially exposed to 1) oxygen, 2) hydrogen, 3) repeatedly O_2, and 4) repeatedly H_2. The time of each exposure was 30 min at a gas pressure of 10^{-6} Torr. After each exposure, the pressure in the microscope chamber was reduced to a deep vacuum of 10^{-10} Torr and after 14 h of exposure at this pressure, the volt-ampere characteristics (VAC) of the nanocontact with gold nanoparticles were measured.

In the absence of adsorbed atoms O, H or their combinations on the surface of particles, the S-shape characteristic of the nanocontact formed by conductors was observed. The appearance of a forbidden zone with zero current in a certain range of applied voltages on the VAC indicated the presence of O- or H-containing adsorbates on the surface of particles.

According to the results of the first series of experiments, the following was found: 1) 14 hours after exposure to O_2, no adsorbed oxygen was found on the nanoparticle surface; 2) 14 hours after exposure to H_2, the volt-ampere characteristics of the nanoparticles had a forbidden zone, indicating the presence of H-containing adsorbates on the nanogold surface; 3) after repeated exposure to oxygen, the VACs also had a forbidden zone after a 14-hour exposure, but the width of the forbidden zone (0.5–1 eV) was different from the forbidden band width for adsorbed hydrogen (1.5–2 eV). This

means that repeated exposure to O_2 after H_2 led to the formation of a new adsorbate on the surface of gold particles, the nature of which was not revealed in [6]; 4) finally, in the last experiment of the series, repeated exposure to H_2 led to the purification of the nanogold surface from any adsorbates after 14-hour exposure of the sample in vacuum: about 97% of the WAC measured on the nanoparticles had an S-shape characteristic of pure metal. Reactions leading to the removal of adsorbates upon repeated exposure to H_2 were also not detected.

In the second series of experiments, the influence of the substrate material on the adsorption of oxygen and hydrogen on a single gold nanoparticle was determined. For this purpose, the tungsten electrode with a nanoscale tip used in the first series of experiments (the second electrode was a gold nanoparticle on HOPG) was replaced by a gold electrode also with a nanoscale tip, and the role of the second electrode was played by a plate of pure HOPG. In this case, the gold tip modeled the gold nanoparticle located on the massive gold. The further mode of experiments was completely identical to the mode of experiments in the first series described above, when gold nanoparticles were on the surface of the HOPG. According to the results of the second series, it was found that for the case of gold nanoparticles on massive gold, all the effects of hydrogen or oxygen adsorption detected in the first series (gold nanoparticles on carbon) were absent. The authors [6] suggested that the different reactivity of gold nanoparticles on carbon or gold substrate is related to the charge of gold nanoparticles located on the surface of the HOPG. The charging is associated with different values of electron yield work of graphite (4.75 eV) and gold (5.1–5.5 eV). The difference leads to electron flow from the material with lower yield work to the material with higher yield work, resulting in negative charge of gold nanoparticles on the HOPG. For the case of gold nanoparticles on massive gold, there is no particle charging.

The influence of charging of gold nanoparticles on their catalytic activity in CO oxidation was investigated in [8, 9]. The charge on nanoparticles was created by applying a voltage to an electrically conductive substrate with particles deposited on it. It was found experimentally that the creation of both negative and positive charge on the nanoparticles accelerates CO oxidation, but the effect of positive charging exceeds that of negative charging. An explanation based on quantum chemical calculations for the results obtained is proposed. In [10], the interaction of CO and H_2 with gold nanoparticles in the presence of an electric field was investigated. It was shown that depending on the direction of the electric field vector, the adsorption of molecules from the gas phase is accelerated or decelerated. Quantum-chemical modeling of adsorption of H atom on Au_nNi_m and Au_nCu_m clusters was performed in [11].

The objectives of the present work are to obtain on the basis of quantum-chemical calculations 1) data on the heats of adsorption of H_2 and O_2 on electroneutral and negatively charged gold nanoparticles and 2) data on the sequence and energetics of elementary reactions on the surface of negatively charged gold nanoparticles when hydrogen, oxygen, and hydrogen again are supplied to them under the experimental conditions described above [6]. Calculations were performed for the simplest electrically neutral or negatively charged gold nanoparticles, Au_3 or Au_3^-, using the OpenMX-3.7 software package [12, 13]. The basis sets were the sets recommended in [12, 13] for the most accurate calculations – *s3p3d2f*1 for Au, *s3p2d2* for O, and *s2p2d*1 for H.

2. DISCUSSION OF RESULTS

Fig. 1 shows the calculated structures of electroneutral and negatively charged gold particles Au_3 and Au_3^-, as well as the structures of isomers formed by adsorption of H_2 on these particles. The calculated heats of adsorption are also indicated in the same figure. Electrically neutral Au_3 and adsorbates Au_3H_2 model pure and coated gold nanoparticles adsorbed with hydrogen on a solid gold substrate, while negatively charged Au_3^- and adsorbates $(Au_3H_2)^-$ model gold nanoparticles and H-containing adsorbates on a carbon substrate. As follows from Fig.1, the most stable is the negatively charged isomer $(H\text{-}Au_3\text{-}H)^-$ with calculated adsorption heat Q = 43.7 kcal/mol, while for electrically neutral Au_3H_2 isomers the adsorption heat is significantly lower and does not exceed 16.4 kcal/mol. Note that the calculated for $(H\text{-}Au_3\text{-}H)^-$ heat of adsorption Q = 43.7 kcal/mol agrees with the experimentally estimated $Q_{exptl.} \geqslant 37$ kcal/mol for adsorption of H_2 on nanogold deposited on a carbon substrate [6].

The calculated heats allow us to estimate the adsorbate lifetime τ on the nanogold surface using Frenkel's formula [14]:

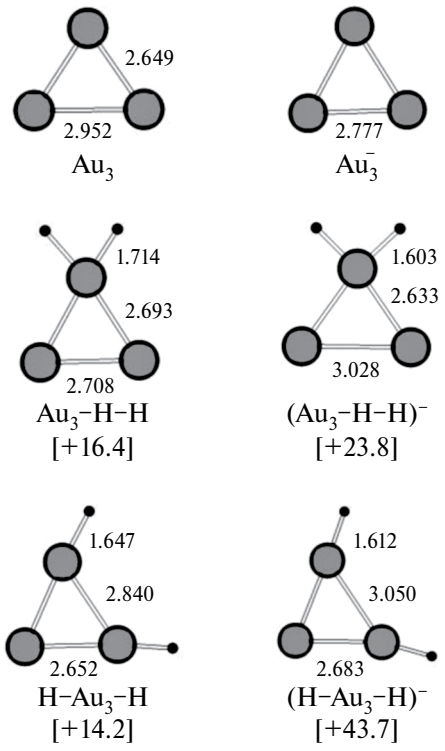

Fig. 1. Structures of Au_3 and Au_3^-, as well as the structures of the electroneutral and negatively charged adsorbate isomers Au_3H_2 and $(Au_3H_2)^-$. Gray labels are Au, black labels are H. Distances are in Angstroms. Heats of adsorption in kcal/mol are given in square brackets.

$$\tau = \tau_0 \exp(E_a/RT), \quad (1)$$

where $\tau_0 = 10^{-13}$s, is the characteristic period of adsorbate oscillations, E_a is the desorption activation energy, which for estimations can be taken equal to the heat of adsorption Q. If the sample residence time t in deep vacuum is much less than τ, $t << \tau$, then hydrogen adsorbed on nanogold is retained on the gold surface, and if $t >> \tau$, then hydrogen is completely desorbed and the gold surface becomes clean. For the case of nanogold on carbon, Q = 43.7 kcal/mol and under the experimental conditions [6] (t = 14 h at room temperature) $t/\tau \sim 10^{-14}$. In this case, the adsorbed hydrogen should be retained on the surface of nanogold, which is consistent with and explains the experiment. However, for the case of nanogold on gold, Q = 16.4 kcal/mol and $t/\tau \sim 10^6$. In this case, hydrogen should be completely desorbed from the nanogold, which was observed in the experiments.

Fig. 2 shows the calculated structures of isomers formed by adsorption of O_2 on electrically neutral Au_3 (modeling nanogold on massive gold) and negatively charged Au_3 particles (modeling nanogold on graphite). The calculated heats of adsorption are also given there. Just as for the adsorption of H_2, the appearance of negative charge on Au_3 leads to an overall increase in the heat of adsorption of O_2. The negatively charged isomer 4_$(O\text{-}Au_3\text{-}O)^-$ possesses the highest heat of adsorption Q = 38.3 kcal/mol. For such a large heat of adsorption, the lifetime of the isomer is 10 orders of magnitude greater than the residence time of the nanogold sample on graphite in deep vacuum, $t/\tau \sim 10^{-10}$, and if O_2 adsorption were to occur, the presence of oxygen on the nanogold would be experimentally detected. However, in the experiments, the gold surface remained clean. This means that no oxygen adsorption occurred during the time that the nanogold/graphite sample was exposed to oxygen (30 min at $Po_2 = 10^{-6}$ Torr). This is possible only when adsorption occurs with some activation energy E_a, the value of which can be estimated as follows. For the above-mentioned parameters of oxygen exposure on nanogold, each surface gold atom experiences approximately 2000 collisions with O_2 molecules during the entire exposure time. In order that at such a number of collisions the adsorption probability does not exceed 10% (which in experiments would allow to define the gold surface as clean), it is necessary to fulfill the following condition

$$0.1 \leqslant = 2000\exp(-E_a/RT), \quad (2)$$

i.e., $E_a \geqslant 6$ kcal/mol.

As for the adsorption of O_2 on electrically neutral Au_3 (modeling nanogold on massive gold), the maximum heat of adsorption Q = 25.6 kcal/mol is inherent to the 2_$(Au_3\text{-}O_2)$ isomer. For this heat, the calculated ratio t/τ = 0.2, which theoretically means the adsorption of O_2 under the conditions of the experiment. However, in the actual experiment, no adsorption was detected after 14 hours of the sample in vacuum. Such a discrepancy between the calculation and the experiment can be explained by an error in the calculation of the heat of adsorption, since a reduction of Q by only 2 kcal/mol leads to t/τ = 5, which is sufficient for almost complete desorption of oxygen for 14 hours in a deep vacuum.

Fig. 3 shows the detailed mechanism of interaction of oxygen with stable negatively charged isomer $(H\text{-}Au_3\text{-}H)^-$ established by calculations.

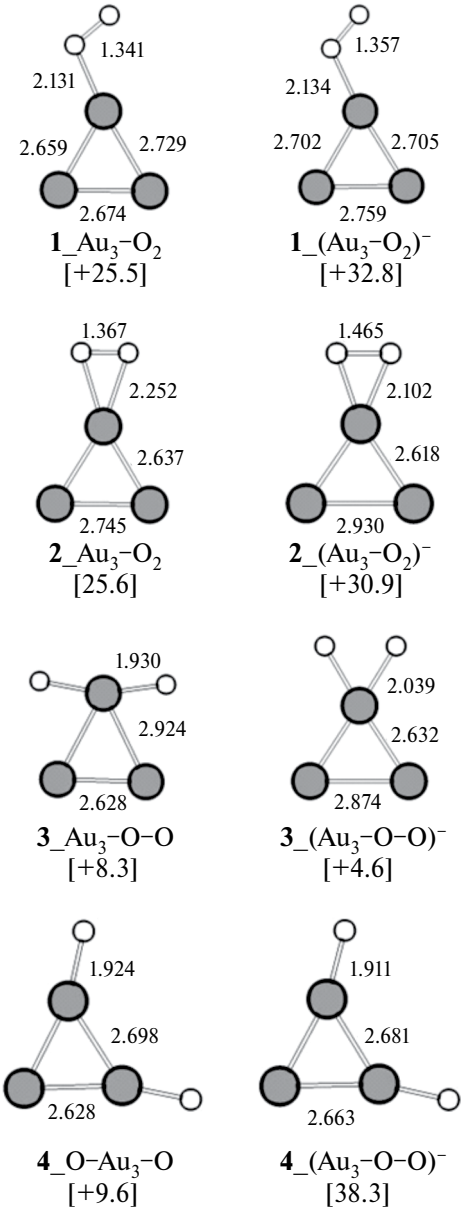

Fig. 2. Structures of the electroneutral and negatively charged adsorbate isomers Au_3O_2 and $(Au_3O_2)^-$. Gray labels are Au, white labels are O. Distances are in Angstroms. Heats of adsorption in kcal/mol are given in square brackets.

The calculated heats of the elementary reactions of the interaction are also given there. The interaction of oxygen with $(H\text{-}Au_3\text{-}H)^-$ models the interaction of oxygen with negatively charged gold hydride formed on the surface of the nanogold/graphite sample after exposure of the sample in hydrogen.

According to Fig. 3, two O_2 molecules are involved in the interaction. When interacting with the first O_2 molecule, complex ***1***_$(H–Au_3–H–O_2)^-$ is formed first. Subsequent migration of the H atom from the Au atom to the adsorbed O_2 molecule leads to the formation of the energetically favorable compound ***3***_$(H–Au_3–O_2H)^-$ with the HO_2 group.

The interaction with the second O_2 molecule also begins with the formation of the $O_{(2)}$-containing complex ***4***_$(O_2\text{-}H\text{-}Au_3\text{-}O_2H)^-$. However, in this complex, it is energetically more favorable for the H atom to migrate not to the adsorbed O_2 molecule but to the previously formed HO_2 group to form the H_2O-complex ***8***_$(O_2\text{-}Au_3\text{-}O\text{-}H_2O)^-$. Subsequent desorption of H_2O and O_2 from this complex leads to the formation of negatively charged oxide $(Au_3O)^-$. The total heat effect of the reaction is 45.1 kcal/mol kcal/mol,

$$(Au_3H_2)^- + O_2 \rightarrow (Au_3O)^- + H_2O. \qquad (3)$$

The limiting step is the desorption of O_2 from compound ***9***_$(O_2\text{-}Au_3O)^-$.

Fig. 3 explains the mechanism of oxidation of hydrides on the surface of nanogold on a graphite substrate. In the resulting gold oxide, each O atom is bonded to one gold atom. The structures obtained and not identified in [6] after the interaction of oxygen with surface hydrides of nanogold belong to such oxides.

Note that during the formation of oxide $(Au_3O)^-$ from two gold atoms bound to H, one Au atom bound to O is formed, and the second Au atom becomes free from external bonds. In this case, the oxide-free fraction of the nanogold surface should be equal to 50%, which was observed in the experiments [6].

Fig. 4 demonstrates the mechanism of interaction of H_2 with negatively charged oxide $(Au_3O)^-$ established in the calculations. The heats of elementary reactions are also given in the same figure. The interaction of $(Au_3O)^-$ with H_2 simulates the final stage of the experiments [6], when the gold oxide formed earlier on the nanogold/graphite sample was exposed to hydrogen.

According to Fig. 4, first, the complex ***1***_$(H_2\text{-}Au_3\text{-}O)^-$ is formed on the oxygen-free gold atom. Subsequent dissociation of H_2 in the complex leads to the formation of hydride ***2***_$(H\text{-}H\text{-}Au_3\text{-}O)$-. Then migration of one of the H atoms to the oxygen atom leads to the formation of hydroxyl 4_$(H\text{-}Au_3\text{-}OH)^-$, and migration of the second H atom to the O atom leads to the formation of water and a reduced pure Au_3 cluster. The total heat effect of the reaction is 40.0 kcal/mol,

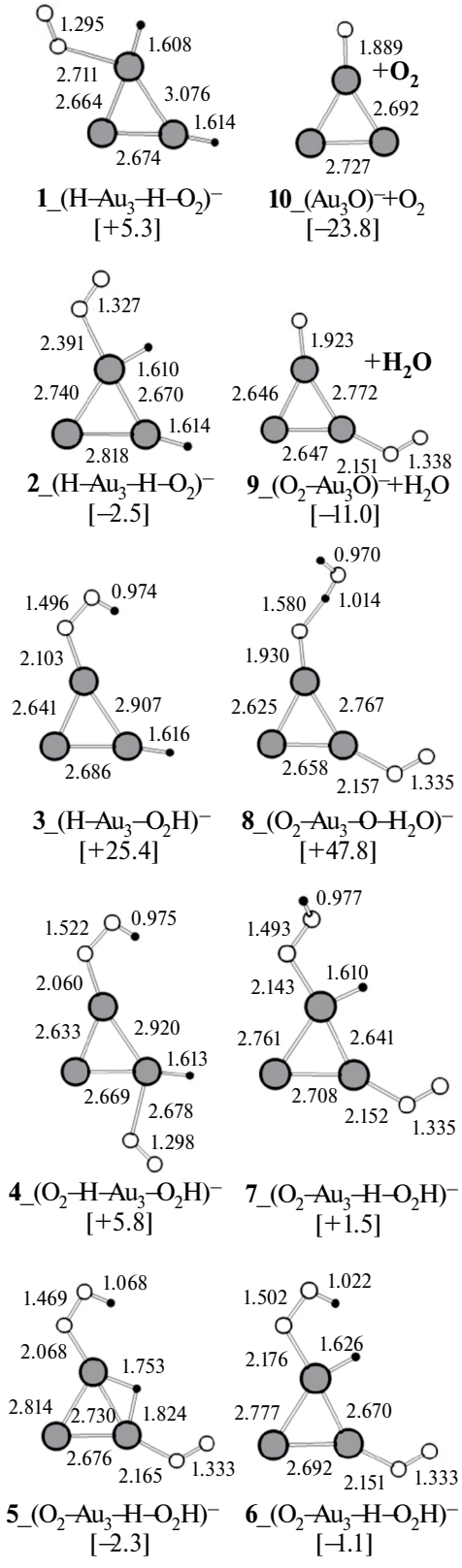

Fig. 3. Mechanism of interaction of a stable negatively charged adsorbate $(H–Au_3–H)^–$ with two O_2 molecules. Gray labels are Au, white labels are O, and black labels are H. Distances are in Angstroms. Heats of elementary reactions in kcal/mol are given in square brackets.

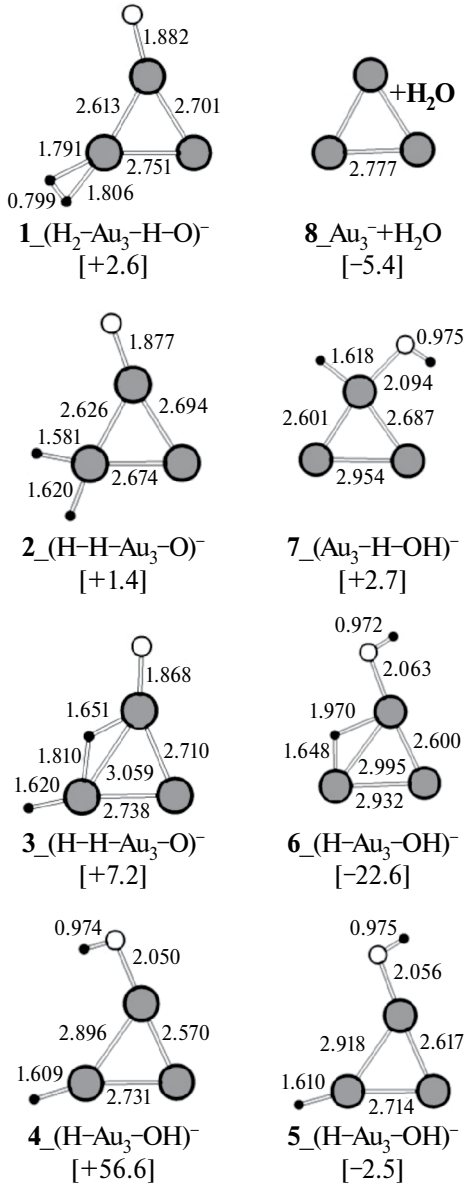

Fig. 4. Mechanism of interaction of negatively charged oxide $(Au_3O)^–$ with H_2 molecule. Gray marks are Au, white marks are O, black marks are H. Distances are in Angstroms (Å). Heats of elementary reactions in kcal/mol are given in square brackets.

$$(Au_3O)^– + H_2 \rightarrow Au_3^– + H_2O. \qquad (4)$$

The limiting step is the migration of the H atom from the Au atom in the Au-H group (compound ***5***) to the Au atom in the Au-OH group (compound **6**).

CONCLUSION

On the basis of quantum-chemical calculations, we proposed an explanation of the experimental data

on the interaction of hydrogen and oxygen with gold nanoparticles placed on substrates made of carbon or massive gold. Nanogold on solid gold is electrically neutral, while nanogold on carbon has a negative charge because the work of electron yield from gold exceeds the work of electron yield from carbon. In calculations, the mechanism of interaction of H_2 and O_2 with electroneutral or negatively charged gold nanoparticles, as well as the energetics of elementary reactions were determined on the examples of reactions of the simplest gold nanoparticles Au_3 and Au_3^-. According to the results of calculations, the following was found:

1. The heat of adsorption of H_2 on Au_3^- is $Q = 43.7$ kcal/mol, while the heat of adsorption of H_2 on Au_3 is significantly lower and does not exceed 16.4 kcal/mol. At $Q = 43.7$ kcal/mol, the adsorbate lifetime on the adsorbing surface with room temperature is $\tau 10^{15}$ hours. In this case, 14 hours after the hydrogen exposure of the nanogold/graphite sample is completed, almost the entire surface of the nanogold should be covered with adsorbed hydrogen, which is consistent with and explains the experiment [6]. However, at $Q = 16.4$ kcal/mol $\tau < 10^{-4}$ hours and after 14 hours exposure, the surface of nanogold in the nanogold/massive gold sample should be completely cleared of hydrogen, which also agrees with and explains the experiment [6].

2. The heat of adsorption of O_2 on Au_3^- is $Q = 38.6$ kcal/mol with the adsorption activation energy $E_a \geqslant 6.0$ kcal/mol. The presence of the above activation energy prevents the adsorption of O_2 under the experimental conditions [6], which explains the oxygen free gold surface in the nanogold/graphite system 14 hours after the end of oxygen exposure [6].

Within the accuracy of the calculation, the heat of adsorption of O_2 on Au_3 is $Q = 23.6$ kcal/mol. When Q = 23.6 kcal/mol, the adsorbate lifetime is $\tau \sim 3$ hours. In this case, 14 hours after the completion of oxygen exposure of the nanogold/massive gold sample, almost the whole surface of the nanogold should be free of oxygen, which is also consistent with and explains the experiment [6].

3. The detailed mechanism of interaction of oxygen with negatively charged gold hydride $(Au_3H_2)^-$ has been established. It is shown that the interaction products are negatively charged gold oxide $(Au_3O)^-$ and water H_2O, $(Au_3H_2)^- + O_2 \rightarrow (Au_3O)^- + H_2O$, $Q = 45.1$ kcal/mol.

The energetics of elementary reactions leading to the formation of $(Au_3O)^-$ and H_2O has been calculated. The interaction of O_2 with $(Au_3H_2)^-$ simulates the interaction of O_2 with negatively charged gold hydride formed on the surface of nanogold/graphite sample after exposure of the sample in hydrogen [6].

4. The detailed mechanism of interaction of hydrogen H_2 with negatively charged gold oxide $(Au_3O)^-$ has been established. The interaction leads to the reduction of gold and formation of water, $(Au_3O)^- + H_2 \rightarrow Au_3^- + H_2O$, $Q = 40.0$ kcal/mol. The energetics of elementary reactions leading to the formation of Au_3^- and H_2O has been calculated. The interaction of H_2 with $(Au_3O)^-$ simulates the interaction of H_2 with negatively charged gold oxide formed on the surface of the sample nanogold/graphite as a result of sequential supply of hydrogen and then oxygen to the sample [6].

The data obtained in the present work can be used to model the interaction of hydrogen and oxygen with both electrically charged nanogold and electrically charged massive gold. For massive gold, the charge can be created by applying an electric voltage to the gold.

REFERENCES

1. *Wittstock A., Zielasek V., Biener J., Friend C. M., Baumer M.* // Science. 2010. Vol. 327. P. 319. https://doi.org/10.1126/science.1183591
2. *Raptis C., Garcia H., Stratakis M.* // Angew. Chem. Int. Ed. 2009. Vol. 48. P. 3133. https://doi.org/10.1002/anie.200805838
3. *Taylor S. F. R., Sa J., Hardacre C.* // ChemCatChem. 2011. Vol. 3. P. 119. https://doi.org/10.1002/cctc.201000337
4. *Zhu Y., Tian L., Jiang Z., Pei S., Xie S., Qiao M., Fan K.* // J. Catal. 2011. Vol. 281. P. 106. https://doi.org/10.1016/j.jcat.2011.04.007
5. *Corma A., Serna P.* // Science. 2006. Vol. 313. P. 332. https://doi.org/10.1126/science.1128383
6. *Gatin A. K., Grishin M. V., Gurevich S. A., Dohlikova N. V., Kirsankin A. A., Kozhevin V. M., Kolchenko N. N., Rostovshchikova T. N., Kharitonov V. A., Shub B. R., Yavsin D. A.*. // Izv. AN. Ser. Chemical. 2014. № 8. P. 1696.
7. *Kozhevin V. M., Yavsin D. A., Kouznetsov V. M., Busov V. M., Mikushkin V. M., Nikonov S. Yu.*, Vac. Sci. Techn. B. 2000. Vol. 18. P. 1402. https://doi.org/10.1116/1.591393

8. *Grishin M. V., Gatin A. K., Slutsky V. G., Fedotov A. S., Kharitonov V. A., Shub B. R.* // Chemical Physics. 2022. Vol. 41. № 6. P. 3. https://doi.org/10.31857/S0207401X22060048
9. *Grishin M. V., Gatin A. K., Slutsky V. G., Fedotov A. S., Kharitonov V. A., Shub B. R.* // Chemical Physics. 2023. Vol. 42. № 1. P. 3. https://doi.org/10.31857/S0207401X23010053
10. *Grishin M. V., Gatin A. K., Kharitonov V. A., Ozerin S. A., Sarvadii S. Yu., Shub B. R.//* Russian Journal of Physical Chemistry B. 2022. Vol. 16. № 2. P. 211. https://doi.org/10.1134/S199079312232001X
11. *Dokhlikova N. V., Gatin A. K., Sarvady S. Yu., Ozerin S. A., Rudenko E. I., Grishin M. V., Shub B. R.* // Chemical Physics. 2022. Vol. 41. № 4. P. 72. https://doi.org/10.31857/S0207401X22040021
12. *Ozaki T.* // Phys. Rev. B. 67, 155108(2003). https://doi.org/10.1103/PhysRevB.67.155108
13. *Ozaki T., Kino H.* // Phys. Rev. B. 69, 195113 (2004). https://doi.org/10.1103/PhysRevB.69.195113
14. *L. N. Rozanov.* Vacuum Technique. 2nd ed. // M.: Vysh. shk. 1990. P. 220

ADVANCES IN CHEMICAL PHYSICS, 2025, Vol. 44, No. 1, pp. 45–53

COMBUSTION, EXPLOSION AND SHOCK WAVES

THE EFFECT OF THE METAL BINDER CONTENT AND MECHANICAL ACTIVATION ON COMBUSTION IN THE (TI+2B)+(TI+C)+ *x*(FE+CO+CR+ NI+ Al) SYSTEM

© 2025 N. A. Kochetov*

Merzhanov Institute of Structural Macrokinetics and Materials Science, Russian Academy of Sciences, Chernogolovka, Russia

**e-mail: kolyan_kochetov@mail.ru*

Received December 26, 2023

Revised April 18, 2024

Accepted April 22, 2024

Abstract. The paper investigates the effect of the content of the Fe + Co + Cr + Ni + Al metal binder and mechanical activation (MA) on the combustion rate, elongation of samples during synthesis, mixture yield and size of composite particles after MA, morphology and phase composition of combustion products and activated mixtures in the system (Ti + 2B) + (Ti + C) + x(Fe + Co + Cr + Ni + Al. In the process of the mixture MA, a multicomponent highentropy alloy is formed – a solid solution based on γ-Fe with a FCC lattice (MHEA). A composite material consisting of ceramics and a high-entropy alloy was obtained by the method of self-propagating high-temperature synthesis (SHS). MA increases the maximum content of the metallic binder in the mixture, at which SHS is carried out at room temperature, from 60 to 80%. After MA, the elongation of the product samples and the combustion rate (in the case of a metal binder presence) of mixtures (Ti + 2B) + (Ti + C) + x(Fe + Co + Cr + Ni + Al) increases. For a mixture (Ti + 2B) + (Ti + C) without a binder, the combustion rate decreases after MA. With an increase in the content of the metal binder Fe + Co + Cr + Ni + Al in mixtures (Ti + 2B) + (Ti + C), the size of composite particles increases, the combustion rate, the yield of the activated mixture and the elongation of the samples of the reaction products of MA mixtures decreases. For the initial mixtures, the dependence of the elongation of the combustion product samples on the content of the binder is nonmonotonic, has a maximum.

Keywords: *combustion, mechanical activation, SHS, multicomponent high-entropy alloy, cermet, TiB_2, TiC*

DOI: 10.31857/S0207401X250106e8

1. INTRODUCTION

Materials based on TiB_2 and TiC are in demand due to such properties as high values of elastic modulus (more than 450 GPa) and hardness (more than 25 GPa), rather low density values (4.52 and 4.93 g/cm^3 for TiB_2 and TiC, respectively), good resistance to oxidation and elevated temperatures [1–3]. Self-propagating high-temperature synthesis (SHS) makes it possible to obtain ceramic materials based on titanium carbide and diboride in one technological operation [3]. Combustion of powder mixtures of titanium with boron was studied in [4, 5], titanium with carbon – in [6–10].

The method of mechanical activation (MA) is often used to change the reactivity and properties of powder mixtures [11–16]. The combustion behavior of activated powders of titanium with carbon was studied in [17, 18], and titanium with boron studied in [19, 20].

Multicomponent high-entropy alloys (MHEAs) containing five or more metallic components that can form a single-phase crystalline alloy are a new class of materials with unique microstructure and attractive properties [21–24]. The Fe-Cr-Co-Ni-Al system, which belongs to the family of MHEAs based on 3d – transition metals, is of interest due to its high values of tensile strength and ductility [25], ultimate fracture strain at reduced and even cryogenic temperatures [26], strength and hardness [27], and superplasticity 28].

High-entropy alloys are produced by induction melting [21, 29], electric arc melting in vacuum [30, 31], mechanical alloying or mechanical activation (MA) [32, 33] and other methods. There are published works in which SHS method is used to obtain HEAs. [20, 34, 35].

Metal-ceramic materials combining the properties of metal alloys and ceramics are widely used. Materials based on metal-ceramics are often used as high-temperature structural materials, cutting tools, wear-resistant materials, etc. [36–38]. Studies have been published in which HEAs are used as a binder in metal-ceramics and materials such as: TiB_2-CoCrFeNiAl [20, 39], TiB_2-CoCrFeNiTiAl [40], TiB_2-TiC–CoCrFeNiTiAl [41] are obtained. These materials are supposed to be the origin of a new family of metalloceramics [42].

In the present work, the aim was to synthesize cermet with high-entropy TiB_2-TiC-FeCoCrNiAl bond by SHS method and to investigate the influence of mechanical activation and bond content on the synthesis process.

2. EXPERIMENT

Experiments were performed using aluminum powder ASD-4 with an average particle size of 10 μm, nickel powder NPE-1 with an average particle size of 150 μm, carbonyl radio-technical iron powder P-10 with an average particle diameter of 3.5 μm, chromium powder PH-1M with particle size less than 125 microns, cobalt powder PK-1u with particle size less than 71 microns, boron powder black, amorphous, particle size less than 1 micron, titanium powder grade PTM-1 with average particle size 120 microns and carbon black powder grade P-803 with dispersity 1–2 microns.

High-entropy binder Fe+Co+Cr+Ni+Al was added to the powder mixture (Ti+2B) + (Ti+ C) (60 wt.% Ti+2B and 40 wt.% Ti+C) (all metals of the binder in equimolar ratio, i.e. Fe – 22.12 wt.%, Co – 23.34 wt.%, Cr – 20.6 wt.%, Ni – 23.25 wt.%, Al – 10.69 wt.%). The binder content varied from 0 to 90 wt%. Mixtures of powders (Ti+2B)+ (Ti+ C) +x(Fe+Co+Cr+Ni+Al) were prepared by mixing the initial components in a porcelain mortar in a given amount (x varied from 0 to 90 wt.%). The Fe+Co+Cr+Ni+Al bond will be denoted for convenience as 5Me.

MA of powder mixtures was carried out in a water-cooled AGO-2 mechanoactivator at an acceleration of 90 *g* using steel balls with a diameter of 9 mm in an air atmosphere. The ratio of ball mass to powder mass in the activator drums was 20:1, activation duration was 5 min.

To study the combustion process, cylindrical samples with a diameter of 10 mm and a height of 12–17 mm were obtained from the initial and activated powders by cold double-sided pressing. The mass of samples varied from 2 to 4 g, pressing pressure was 95–130 Kg/cm^2. The mass of the samples increased with the growing HEA content in the mixture to maintain relative density values in the range of 0.56–0.6.

The combustion process of compressed samples was carried out in a constant pressure chamber in an inert argon environment at a pressure of 760 mm Hg. [11, 13, 15, 17, 19, 20, 34, 35]. The process was videotaped through a viewing glass on a video camera. By frame-by-frame viewing of the video recordings of the combustion process, the combustion rate of the samples was determined. The synthesis was initiated by a heated tungsten spiral through a Ti+2B ignition tablet from the upper end of the sample to ensure stable ignition conditions.

The relative elongation of the burned samples was taken as the ratio of their height to the height of the original samples.

The values of pressing pressure, relative elongation and combustion rates of the samples, as well as the yield of the mixture after MA were determined as an average of the results of several experiments, the error of determination did not exceed 10%.

X-ray phase analysis (XRD) was performed on a DRON 3 diffractometer (Cu$K\alpha$ radiation).

The fractional composition and particle size distribution of the mixture were determined according to the standard method on the laser analyzer "Microsizer-201C". The measurement error did not exceed 1.2%.

3. DISCUSSION OF RESULTS

X-ray phase analysis (XRD) of the activated powders (Ti+2B)+(Ti+ C)+x(5Me) showed that during the MA process lasting 5 min a multicomponent high-entropy alloy – solid solution based on γ-Fe with FCC lattice (HEA) was formed. Reflexes of initial titanium (boron and carbon black are amorphous) were also observed on X-ray diffraction images of activated mixtures. Reflexes of individual metals included in the binder (iron, cobalt, chromium, nickel, and aluminum) are not observed, thus it can be concluded that transition metals formed the MHEAs (Fig. 1).

Part of the powder adheres (sticks) to the walls of the activator drums and the surface of the balls in the process of MA [20, 13]. As the yield of the mixture after activation, we take the ratio of the mass of non-sticky activated mixture, which can be easily

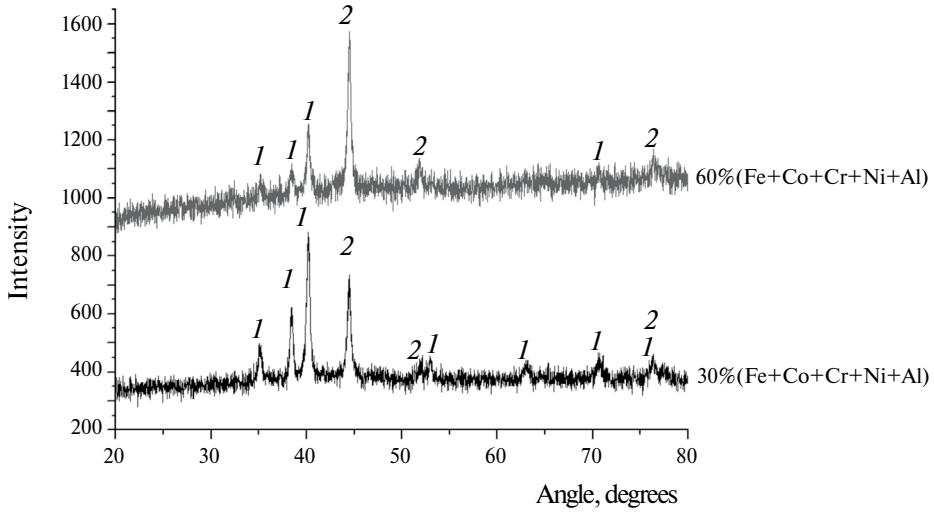

Fig. 1. XRD results of activated mixtures of (Ti+2B)+(Ti+C)+ x(5Me). X= 30 and 60 wt%. Numbers indicate phase reflections: 1 – Ti, 2 – FCC phase (HEA)

removed after MA from the drum, to the mass of the initial powder mixture put into the drum before MA. Addition of 5Me metal binder, in which plastic metals are present, to the activated mixture increases the powder sticking during the MA process on the drum walls and ball surface. As a result, as the content of metal binder increases, the yield of the mixture after MA decreases (Fig. 2).

During the MA process, the particles of the initial components deform, collapse and agglomerate among themselves, forming composite particles [13–16, 20]. The size of composite particles of the activated mixture (Ti+2B)+(Ti+C)+x(5Me) increases with the increase in the metal bond content, but this increase does not exceed 12.5% (from 28 to 32 μm) (Fig. 3).

In the case of specimens pressed from activated mixtures, the values of pressing pressure applied to obtain specimens of a given density decrease, indicating that the compaction of the mixtures improves with increasing metal binder content (Fig. 4).

The maximum metal bond content x, at which the combustion of pressed samples could be initiated and the samples burned to the end, in the case of initial mixtures (Ti+2B)+(Ti+ C)+x(5Me) was 60 wt.%. Activation increased the limiting value of x at which combustion was realized to 80 wt%.

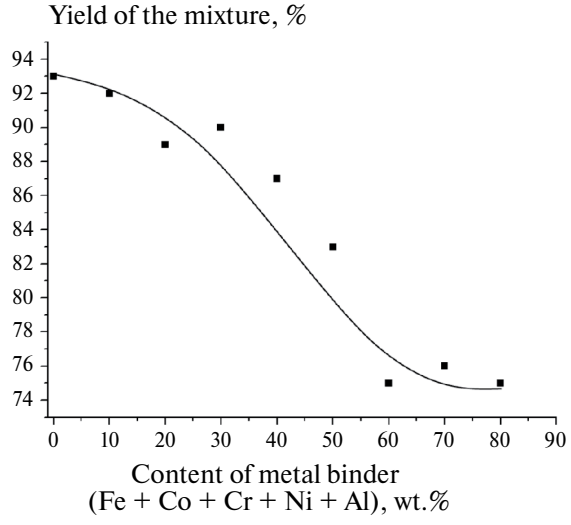

Fig. 2. Dependence of the activated mixture yield on the content of metal binder in the mixture 60%(Ti+2B)+ 40%(Ti+C)+x(5Me)

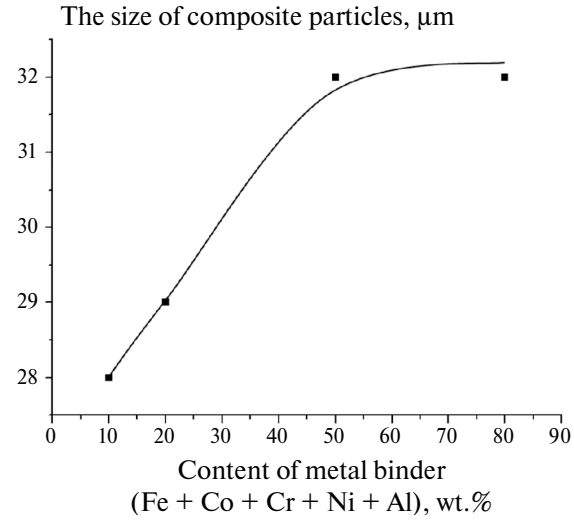

Fig. 3. Dependence of the average particle size of the activated mixture 60%(Ti+2B)+40%(Ti+C)+x(5Me) on the metal bond content x

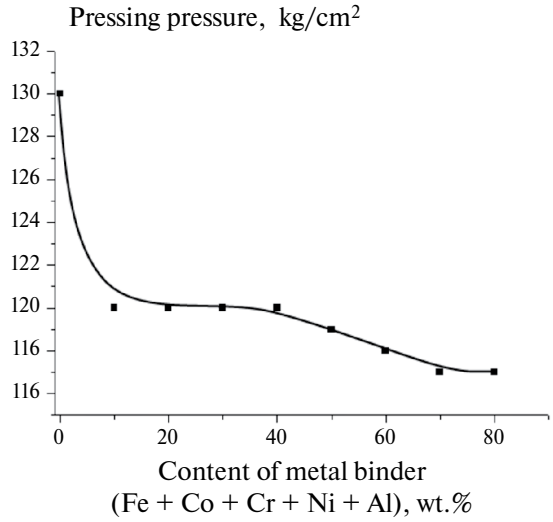

Fig. 4. Dependence of pressure used for pressing of samples from MA mixture 60%(Ti+2B)+ 40%(Ti+C)+x(5Me) on the content of metal binder in the mixture

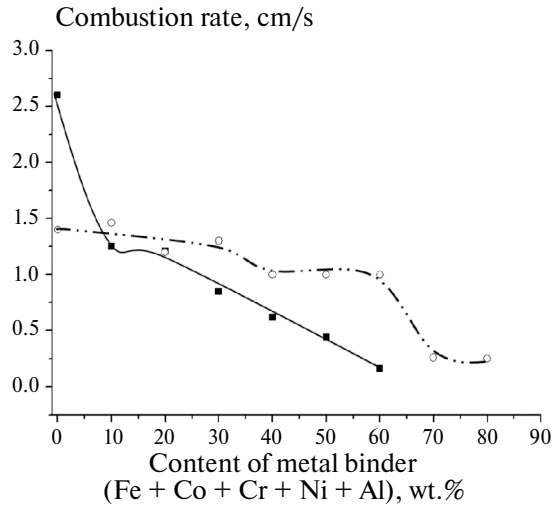

Fig. 5. Dependence of the combustion rate of samples on the content of metal binder in ■ – initial mixture 60%(Ti+2B)+40%(Ti+C)+x(5Me), **O** – activated mixture 60%(Ti+2B)+ 40%(Ti+C)+x(5Me)

Similar results were obtained earlier on the system (Ti+2B)+x(5Me) [20].

The dependences of the experimentally measured combustion rate of the samples on the content of metal binder (5Me) for the initial and activated powders are presented in Fig. 5. It can be seen that for all mixtures the combustion rate of the samples decreases with the increase in the content of metal binder in the mixture. These trends are expected, because after the addition of metal binder to the mixture (Ti+2B)+(Ti+C), in addition to the main exothermic reactions between titanium and boron and titanium and carbon, there is also melting of metals with the subsequent formation of a multicomponent high-entropy alloy, which does not lead to the release of significant amounts of heat.

The combustion rate of MA powders exceeds the combustion rate of initial powders in the case of the presence of metal binder (5Me) in the mixture. Moreover, this excess increases with the increase in the content of metal binder in the mixtures. For the mixture (Ti+2B)+(Ti+C) without bonding, the combustion rate decreases after MA (Fig. 5).

It was noted earlier that during the MA process additional impurity gases enter the processed powder [13, 15, 19, 20, 43, 44]. The release of these gases during combustion of samples from MA mixtures leads to their destruction at a binder content of 50 wt.% and less (Fig. 6).

A part of impurity gases can be released in front of the combustion front, slowing down its propagation rate, in accordance with the convective-conductive model of combustion [45]. Thus, there are factors that increase the combustion rate of the mixture after MA (increase in the contact area and removal of diffusion difficulties between components of the activated mixture), and there are factors that decrease the combustion rate after MA (increase in the amount of impurity gases).

Probably, in the case of the mixture (Ti+2B)+(Ti+C) without binder, after MA, the effect of the factor decreasing the combustion rate (i.e., the increase of impurity gases in the activated powder) prevails. This leads to a decrease in the combustion rate of the samples after MA.

In the case of powders (Ti+2B)+(Ti+C) + x(5Me) with a metal bond, the effect of MA prevails, increasing the burning rate of the powder after activation (increasing the contact area and removal of diffusion difficulties between the components of the activated mixture). In favor of this is evidenced by the decrease in the content of impurity gases and the maximum combustion temperature of powders (Ti+2B)+(Ti+C) + x(5Me) with increasing content of metal bond. Earlier it was found that dilution of powder mixtures Ti+C and Ti+2B with metals not participating in the exothermic reaction (Fe, Co, Cr, Ni, Al, Cu) reduces the amount of impurity gases emitted during combustion of these powders and decreases their maximum combustion temperature [20, 34, 35, 46–50]. According to XRD

Fig. 6. Photograph of samples of combustion products of activated mixtures 60%(Ti+2B)+40%(Ti+C)+x(5Me), x=: 1–0%, 2–10%, 3–20%, 4–30%, 5–40%, 6–50%, 7–60%, 8–70%, 9–80% wt.%

data, only reflexes of titanium carbide and titanium diboride phases, as well as high-entropy alloy, are observed in the combustion products of activated mixtures (Fig. 7b). That is, the addition of a metallic bond (5Me) to the system (Ti+2B)+(Ti+C) can be considered as inert. As a result, for (Ti+2B)+(Ti+C) + x(5Me) powders, the combustion rate after MA increases, and this increase increases with the increase in the content of metal bond (5Me) (Fig. 5).

It should be noted that at combustion of the initial mixture Ti+2B + Ti+C without a metallic binder, the reflexes of TiB_2 and TiC phases are observed in the product. When the binder is added, the X-ray diffraction patterns of both MA products and initial powders show reflections corresponding to the solid solution based on γ-Fe with FCC lattice (HEA), as well as those corresponding to the solid solution based on α-Fe with BCC lattice (HEA) (Fig. 7a, b).

It was noted earlier that during the synthesis process behind the combustion front, elongation of samples often occurs due to the release of impurity gases [13, 15, 20, 51–53]. When adding to the initial powder (Ti+2B) + (Ti+C) a small amount (10 wt.%) of metal binder, which is more fusible than TiB_2 and TiC, the amount of liquid phase in the combustion front increases, which leads to an increase in the elongation of the sample in the combustion process (Fig. 8). With further increase in the amount of metal bonding in the initial mixture, probably, the effect of reducing the amount of impurity gases and decreasing the maximum reaction temperature begins to prevail, which leads to a decrease in the elongation of the reaction product samples [20, 34, 35, 46–50] (Fig. 8).

As noted above, during the MA process, additional impurity gases are introduced into the treated powders. The release of these gases during combustion of samples from activated mixtures led to their destruction (Fig. 6). Only at the content of metal binder in MA mixtures 60 wt.% and more reaction products retained their integrity, which allowed to measure their elongation (Fig. 8). Samples of synthesis products of initial powders containing less impurity gases, as compared to activated mixtures, retained their integrity at all values of the metal binder content (Fig. 9).

It can be seen that the elongation of samples of combustion products of activated powders significantly exceeds the elongation of samples of combustion products of initial mixtures. In addition, the elongation of samples of MA powder products, as well as in the case of the initial mixtures, decreases with increasing content of metal bonding in the mixtures

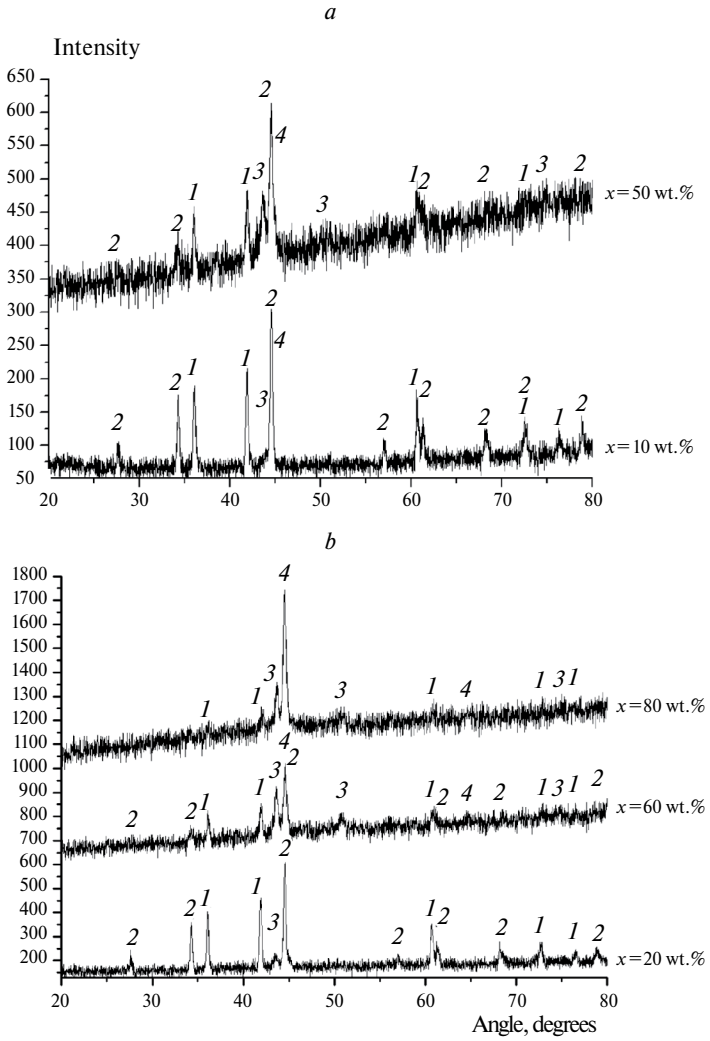

Fig. 7. XRD results of combustion products a – initial mixtures, b – activated mixtures 60%(Ti+2B)+40%(Ti+C)+x(5Me). X= 10 and 50 wt% for the initial and 20, 60 and 80 wt% for the activated mixtures. Numbers denote phase reflections: 1 – TiC, 2 – TiB_2, 3- FCC phase (HEA), 4 – OCC phase (HEA)

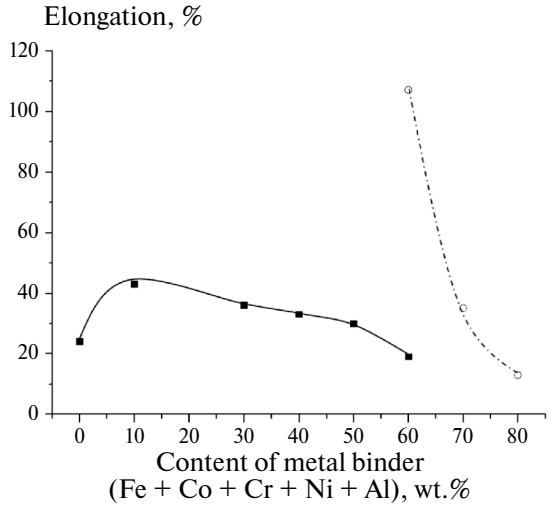

Fig. 8. Dependence of the relative change in specimen length on the metal bond content in ■ – initial and **O** – activated mixture 60%(Ti+2B)+40%(Ti+C)+x(5Me)

due to a decrease in the amount of impurity gases and a decrease in the maximum reaction temperature (Fig. 8).

The results of this work can be used to optimize the production of cermets based on MHEAs.

4. CONCLUSION

In the process of MA powders (Ti+2B)+ +(Ti+C)+x(5Me) lasting 5 min, a multicomponent high entropy alloy – solid solution based on γ-Fe with FCC lattice (MHEA) is formed.

With increasing content of 5Me metal bond in mixtures (Ti+2B)+(Ti+C) the size of composite particles after MA increases, the combustion rate, the yield of activated mixture and elongation of samples of reaction products of MA mixtures decrease. For initial powders, the dependence

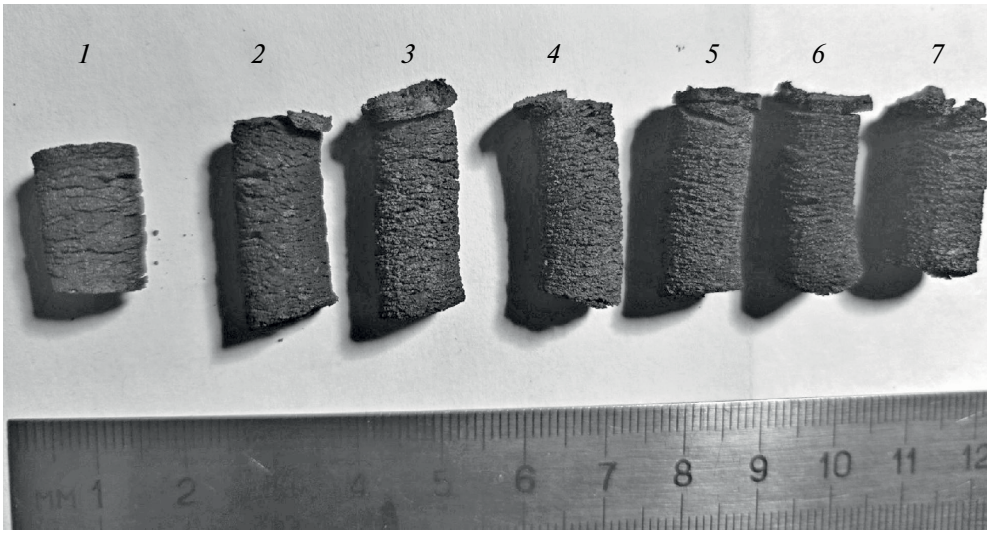

Fig. 9. Photograph of samples of combustion products of initial mixtures 60%(Ti+2B)+ 40%(Ti+C)+x(5Me), x=: 1–0%, 2–10%, 3–20%, 4–30%, 5–40%, 6–50%, 7–60%

of elongation of combustion product samples on the binder content is non-monotonic and has a maximum.

MA increases the mass content of 5Me metal bond in the mixture (Ti+2B)+(Ti+C), at which the combustion of samples at room temperature occurs, up to 80%.

The elongation of the combustion product samples and the combustion rate (in the case of metal bonding) of (Ti+2B)+(Ti+C)+x(5Me) mixtures increase after MA. For the mixture (Ti+2B)+(Ti+C) without a binder, the combustion rate decreases after MA.

A composite material consisting of ceramics and high-entropy alloy was obtained by SHS method.

ACKNOWLEDGEMENTS

The author is grateful to I. D. Kovalev for the X-ray phase study of the mixtures and their synthesis products, and to M. L. Busurina for the study of particle size distribution.

REFERENCES

1. *Basu B., Raju G. B., Suri A. K.*. // Int. Mater. Rev. 2006. Vol. 51. No. 6. P. 352. https://doi.org/10.1179/174328006X102529
2. *Vallauri D., Atías Adrián I. C., Chrysanthou A.* // J. Eur. Eur. Ceram. Soc. 2008. Vol. 28. No. 8. P. 1697. https://doi.org/10.1016/j.jeurceramsoc.2007.11.011
3. *Rogachev A. S., Mukasyan A. S.* Combustion for Material Synthesis. – New York: CRC Press, Taylor & Francis Group, 2015.
4. *Hardt A. P. and Phung P. V.* // Combustion and Flame. 1973. Vol. 21. No. 1. P. 77.
5. *Hardt A. P. and Holsinger R. W.* // Combustion and Flame.- 1973. – Vol. 21, No. 1.- Pp. 91–97.
6. *Shkiro V. M., Borovinskaya I. P.* Study of combustion patterns of titanium-carbon mixtures. In Collected Works: Combustion Processes in Chemical Technology and Metallurgy. Chernogolovka, 1975. P. 253.
7. *Seplyarsky B. S., Tarasov A. G., Kochetkov R. A.* // Combust. Explos. Shock Waves. 2013.V.49. No. 5. P. 555.
8. *Levashov E. A., Bogatov Yu. V., Milovidov A. A.* // Combust. Explos. Shock Waves. 1991. V.27. No. 1. P. 83.
9. *Seplyarsky B. S., Vadchenko S. G., Kostin S. V., et al. V.* et al. // Combust. Explos. Shock Waves. 2009. Vol. 45. No. 1. P. 25. https://doi.org/10.1007/s10573-009-0004-x
10. *Knyazik V. A., Merzhanov A. G., Solomonov B. V., et al.* // Combust. Explos. Shock Waves. 1985. Vol. 21. No. 3. P. 333.
11. *Kochetov N. A., Seplyarskiy B. S.* // Russ. J. Phys. Chem. B. 2020. T 14. No. 5. C. 791. https://doi.org/10.1134/S199079312005005X
12. *Korchagin M. A., Grigorieva T. F., B. B. Bokhonov, etc.* // Combust. Explos. Shock Waves. 2003. Vol. 39. No. 1. P. 43. https://doi.org/10.1023/A:1022145201911
13. *Kochetov N. A.* // Russ. J. Phys. Chem. B. 2022. Vol. 16. No. 4. P. 621. https://doi.org/10.1134/S1990793122040078

14. *Korchagin M. A.* // Combust. Explos. Shock Waves. 2015. V.51. No. 5. P. 578. https://doi.org/10.1134/S0010508215050093
15. *Kochetov N. A., Seplyarskiy B. S.* // Russ. J. Phys. Chem. B. 2022. Vol. 16. No. 1. P. 66. https://doi.org/10.1134/S1990793122010079
16. *Korchagin M. A., Filimonov V. Y., Smirnov V. E., et al.* // Combust. Explos. Shock Waves. 2010. Vol. 46. No. 1. P. 41. https://doi.org/10.1007/s10573-010-0007-7
17. Kochetov N. A., Seplyarskiy B. S. // Izv. of universities. Powder Metallurgy and Functional Coatings. 2017. No. 3. P. 4. https://doi.org/10.17073/1997-308X-2017-3-4-13
18. *Vyushkov B. V., Levashov E. A., Ermilov A. G., et al.* // Combust. Explos. Shock Waves. 1994. Vol. 30. No. 5. P. 630.
19. *Kochetov N. A., Vadchenko C. G.* // Combust. Explos. Shock Waves. 2015. Vol. 51. No. 4. P. 467. https://doi.org/10.1134/S0010508215040103
20. *Kochetov. N. A.* // Combust. Explos. Shock Waves. 2022. Vol. 58. No. 2. P. 169. https://doi.org/10.1134/S0010508222020058
21. *Cantor B., Chang I. T. H., Knight P. et al.* // Mater. Sci. and Eng.: A. 2004. Vol. 375. P. 213. https://doi.org/10.1016/j.msea.2003.10.257
22. *Zhang Y., Zuo T. T., Tang Z. et al.* // Prog. Mater. Sci. 2014. Vol. 61. P. 1. https://doi.org/10.1016/j.pmatsci.2013.10.001
23. *Tsai M.-H., Yeh J.-W.* // Mater. Res. Lett. 2014. Vol. 2. No. 3. P. 107. https://doi.org/10.1080/21663831.2014.912690
24. *Chou H.-P., Chang Y.-S., Chen. S.-K. et al.* // Mater. Sci. Eng.: B. 2009. Vol. 163. No. 3. P. 184. https://doi.org/10.1016/j.mseb.2009.05.024
25. *Gali A., George E. P.* // Intermetallics. 2013. Vol. 39. P. 74. https://doi.org/10.1016/j.intermet.2013.03.018
26. *Gludovatz B., Hohenwarter A., Catoor D., et al.* // Science. 2014. Vol. 345. Iss. 6201. P. 1153. https://doi.org/https://doi.org/10.1126/science.1254581
27. *Kilmametov A., Kulagin R., Mazilkin A, et al.* // Scr. Mater. 2019. Vol. 158. Pp. 29–33. https://doi.org/10.1016/j.scriptamat.2018.08.031
28. *Shahmir H., He J., Lu Z. et al.* // Mater. Sci. Eng. A. 2017. Vol. 685. No. 8. P. 342. https://doi.org/10.1016/j.msea.2017.01.016
29. Gu J., Ni S., Liu Y. *et al.* // Mater. Sci. Eng. A. 2019. Vol. 755. P. 289. https://doi.org/10.1016/j.msea.2019.04.025
30. *Bhattacharjee P. P., Sathiaraj G. D. et al.* // J. Alloys Compd. Alloys Compd. 2014. Vol. 587. P. 544. https://doi.org/10.1016/j.jallcom.2013.10.237
31. *Yeh J.-W., Chen Y.-L., Lin S.-J. et al.* // Mater. Sci. Forum. 2007. Vol. 560. P. 1. https://doi.org/10.4028/www.scientific.net/MSF.560.1
32. *Kochetov N. A., Rogachev A. S., Shchukin A. S. et al.* // Russ. J. Non-Ferr. Metals. 2019. Vol. 60. No. 3. P. 268. https://doi.org/110.3103/S106782121903009X
33. *Rogachev A. S., Vadchenko S. G., Kochetov N. A. et al.* // J. Alloys *Compd*. Alloys Compd.- 2019. – Vol. 805. – Pp. 1237–1245. https://doi.org/10.1016/j.jallcom.2019.07.195
34. *Rogachev A. S., Vadchenko S. G., Kochetov N. A. et al.* // J. Europ. Europ. Ceram. Soc. 2020. Vol. 40. P. 2527. https://doi.org/10.1016/j.jeurceramsoc.2019.11.059
35. *Rogachev A. S., Gryadunov A. N., Kochetov N. A. et al.* // Int. J. Self-Propag. High-Temp. Synth. 2019. Vol. 28.№ . 3. P. 196. https://doi.org/10.3103/S1061386219030117
36. *Rajabi A., Ghazali M. J., Syarif J. et al.* // Chem. Eng. J. 2014. Vol. 255. P. 445. https://doi.org/10.1016/j.cej.2014.06.078.
37. *Rajabi A., Ghazali M. J., Daud A. R.* // Mater. Des. 2015. Vol. 67. P. 95. https://doi.org/10.1016/j.matdes.2014.10.081.
38. Peng Y., Miao H., Peng Z. // Int. J. Refract. Met. H. Mater. 2013. Vol. 39. P. 78. https://doi.org/10.1016/j.ijrmhm.2012.07.001
39. *Zhang S, Sun Y, Ke B. et al.* // Metals. 2018. Vol. 8,No. 1:58. P. 1. https://doi.org/10.3390/met8010058
40. *Fu Z., Koc R.* // Mater. Sci. Eng. A. 2017. Vol. 702. P. 184. https://doi.org/10.1016/j.msea.2017.07.008.
41. *Fu Z., Koc R.* // Mater. Sci. Eng. A. 2018. Vol. 735. P. 302. https://doi.org/10.1016/j.msea.2018.08.058.
42. *de la Obra A. G., Avilés M. A., Torres Y. et al.* // Int. J. Refract. Met. H. Mater. 2017. Vol. 63. P. 17. https://doi.org/10.1016/j.ijrmhm.2016.04.011.
43. *Vadchenko S. G.* // Int. J. Self-Propag. High-Temp. Synth. 2016. Vol. 25. No. 4. P. 210

https://doi.org/10.3103/S1061386216016040105
44. *Vadchenko. S. G.* // Int. J. Self-Propag. High-Temp. Synth. 2015. Vol. 24. No. 2. P. 90. https://doi.org/10.3103/S1061386215020107
45. *Seplyarskiy B. S.* // Dokl. RAS. 2004. Vol. 396. No. 5. P. 640.
46. *Seplyarsky B. S., Kochetkov R. A., Lisina T. G., et al.* // Combustion, Explosion, and Shock Waves. 2023. Vol. 59. No. 3. P. 344. https://doi.org/10.1134/S0010508223030097
47. *Seplyarskiy B. S., Kochetkov R. A., Lisina T. G., et al.* // Russ. J. Phys. Chem. B. 2023. Vol. 17. No. 5. P. 1098. https://doi.org/10.1134/S199079312305010X
48. *Seplyarskiy B. S., Kochetkov R. A., Lisina T. G., et al.* //Russ. J. Phys. Chem. A.. 2023. Vol. 97. No. 3. P. 525. https://doi.org/10.1134/S003602442303024X
49. *Seplyarskii, B. S., Kochetkov, R. A., Lisina, T. G. et al.* // Int. J Self-Propag. High-Temp. Synth. 2022. Vol. 31. P. 195 https://doi.org/10.3103/S1061386222040100
50. *Seplyarsky B. S., Abzalov N. I., Kochetkov R. A., Lisina T. G.* // Russ. J. Phys. Chem. B. 2021. Vol. 15. No. 2. P. 242. https://doi.org/10.1134/S199079312102010X
51. *Kamynina O. K., Rogachev A. S., Sytschev A. E. et al.* // Int. J. Self-Propag. High-Temp. Synth. 2004. Vol. 13, No. 3. P. 193.
52. *Kamynina O. K., Rogachev A. S., Umarov L. M. // Physics of Combustion and Explosion. S., Umarov L. M.* // Combust. Explos. Shock Waves. 2003. Vol. 39. No. 5. P. 548.
53. *Kochetov N. A., Seplyarskiy B. S.* // Russ. J. Phys. Chem. B.. 2018. Vol. 12. No. 5. P. 883. https://doi.org/10.1134/S1990793118050172

ADVANCES IN CHEMICAL PHYSICS, 2025, Vol. 44, No. 1, pp. 54–66

COMBUSTION, EXPLOSION AND SHOCK WAVES

EFFECT OF ADDITIVE MODIFIERS ON THE COMBUSTION CHARACTERISTICS OF COMPOSITE ALUMINIZED PROPELLANTS

© 2025 O. G. Glotov[a, b, *], N. S. Belousova[a, b]

[a] *Voevodsky Institute of Chemical Kinetics and Combustion Siberian Branch of the Russian Academy of Sciences, Novosibirsk, Russia*

[b] *Novosibirsk State Technical University, Novosibirsk, Russia*

**e-mail: glotov@kinetics.nsc.ru*

Received February 07, 2024

Revised March 24, 2024

Accepted April 22, 2024

Abstract. The effect of TiB_2, $AlMgB_{14}$, $(NH_4)_2TiF_6$, NH_4BF_4 and $Ca_3(PO_4)_2$ additives-modifiers on the combustion parameters of composite propellants based on ammonium perchlorate (about 60%), powdered aluminum (about 20%), and a binder of the methylpolyvinyl tetrazole type (about 20%) was studied. The additives were introduced in an amount of about 2%. The burning rates of the propellants were measured and the condensed combustion products were studied at a pressure of 0.35 MPa. The effect of additives was assessed in terms of their influence on the burning rate, as well as on the mass, size and incompleteness of combustion of agglomerates. The most effective additives were TiB_2 and $AlMgB_{14}$. Conclusions were made on the possibility of regulating the specified combustion parameters by introducing small additives into the propellant and on the need for further research in this direction.

Keywords: *model composite propellant, aluminum, additives, combustion modifiers, titanium diboride, aluminum-magnesium boride, ammonium tetrafluoroborate, ammonium-titanium fluoride, calcium phosphate 3-substituted, burning rate, agglomeration, condensed combustion products, sampling method, agglomerates, oxide particles, granulometric composition, combustion completeness*

DOI: 10.31857/S0207401X250107e1

1. INTRODUCTION

The development of rocket technology is partly ensured by the improvement of fuel formulations. The purpose of rocket propellant is to release the required amount of energy and working fluid at a given rete during combustion under certain conditions. To date, many effective combustibles, oxidizers and binders are known [1–4], with a special place occupied by composite propellants containing metal particles as a fuel [5–7]. Aluminum has become the most widely used due to the successful combination of such qualities as high heat of combustion and density, safety of handling powder, harmlessness of combustion products, and commercial availability. However, aluminum is characterized by the phenomenon of agglomeration [8], which consists in the unification and merging of the original particles into agglomerates in the combustion wave. Agglomeration usually leads to undesirable consequences – a decrease in the completeness of metal combustion, accumulation of slag in the engine chamber, etc. Therefore, the search for ways to reduce agglomeration is the subject of many experimental studies. The main factors that affect the agglomeration and combustion of aluminum in the composition of propellants are listed below.

The formulation factors are the aluminum content [9–11], the granulometric composition of the components [9, 12], the nature of the binder [13–16], the presence of nitramines [17–19], ammonium nitrate [20–23] or other alternative oxidizers [24–29]. The physical factors are the pressure [30] and the burning rate [31]. The burning rate depends on the pressure and dispersion of ammonium perchlorate (AP) [11, 31], therefore, in order to reduce agglomeration while simultaneously meeting other propellant requirements, it is necessary to optimize a complex system with numerous direct and reverse dependesies. The following are promising

ways of influencing the behavior of the metal in the combustion wave, including agglomeration: modification of the properties of the metal in the volume, for example, by introducing a second metal [32–34]; preparetion of composite particles [35, 36]; modification of the particle surface or the oxide layer covering it [35, 37–44]; introduction of additives into the propellant composition [24, 45–47]. In this case, the introduction of nanosized aluminum [48, 49] can be considered both as an additive to the propellant and as a modification of the properties of aluminum. General ideas about the mechanism of action of additives introduced into the propellant or directly into the metal particles are presented in [50].

This work is aimed at experimentally assessing the effect of five additives on aluminum agglomeration in a typical propellant formulation with AP and an active binder. The essence of the work is to test the possibility of achieving beneficial effects by introducing additives. With regard to agglomeration, these include a decrease in the size and mass of large agglomerate particles, an increase in the completeness of metal combustion, and a decrease in the size of small oxide particles. The work is exploratory in nature and was performed using a simplified method for sampling combustion products. More detailed studies, in particular, of the mechanisms of action of additives, make sense only if the desired effects are detected.

2. PROPELLANTS AND ADDITIVES UNDER STUDY

The experiments were carried out with uncured model mixtures that had a paste-like consistency and contained the following components: Ammonium perchlorate of one of two fractions – coarse with particle sizes of 500–630 μm (APc), or medium with particle sizes of 180–250 μm (AP); active fuel-binder – methylpolyvinyltetrazole (MPVT) type [20]; micron-sized aluminum powder of the ASD-4 brand (Al). The mass ratio of the components AP/binder/Al = 60/20/20 or 62/20/18. The procedure for preparing the propellant mass samples included weighing the components on an MV 210-A analytical balance with an accuracy of 0.0001 g and mixing them manually in a bronze cup with a fluoroplastic spatula. When working with the spatula, they acted very carefully so as not to crumble of the large AP particles. The typical mass of the prepared portion of propellant is approximately 5 g, and in such a portion it is easy to visually control the homogeneity of mixing.

The granulometric characteristics of the powder components are presented in Table 1 and Fig. 1 in the form of normalized functions of the density distribution of the relative mass of particles by size. The normalization was carried out in such a way that the area under the curve (mass) was equal to 1.

The mean particle sizes of the powders D_{mn} were calculated using the formula

$$D_{mn} = {}_{m-n}\sqrt{\left(\sum_{i=1}^{k} D_i^m \cdot N_i\right) \Big/ \left(\sum_{i=1}^{k} D_i^n \cdot N_i\right)}, \quad (1)$$

where m, n are integers specifying the order of the mean size, k is the number of size intervals in the histogram, N_i is the number of particles in the i-th interval, D_i is the middle of the i-th interval. From here on, the calculated values of the mean diameters are given without rounding.

The scheme of variation of propellant compositions is presented in Fig. 2. There are base propellants P1, P2 and P3. Propellant P1 contains 20% of binder, 20% of Al and 60% of APc. Propellant P2 differs in the size of oxidizer particles and contains 20% of binder, 20% of Al and 60% of AP. Propellant P3 has a reduced Al content (18%), an increased AP content (62%) and the same amount of binder (20%). Following [51], additives-modifiers were introduced into each base propellant in an amount of about 2% (over 100%). Additives: titanium diboride TiB_2, aluminum and magnesium boride $AlMgB_{14}$, ammonium titanium(IV) fluoride $(NH_4)_2TiF_6$, ammonium tetrafluoroborate NH_4BF_4, calcium phosphate 3-substituted $Ca_3(PO_4)_2$. The choice of additives is due to the presence of "combustible" atoms of Al, Mg, B, Ti or an F atom as an oxidizer and at the same time an element capable of interacting with the oxide film covering aluminum particles. The compound $Ca_3(PO_4)_2$ is conditionally inert and is used for comparison. Below we will discuss three "lines" of formulation obtained from base propellants P1, P2 and P3 by introducing the listed

Table 1. Mean particle sizes of powdered propellant components (in μm)

Propellant	D_{10}	D_{30}	D_{32}	D_{43}
APc	712	723	734	746
AP	221	232	242	249
Al	4.2	5.8	8.7	15

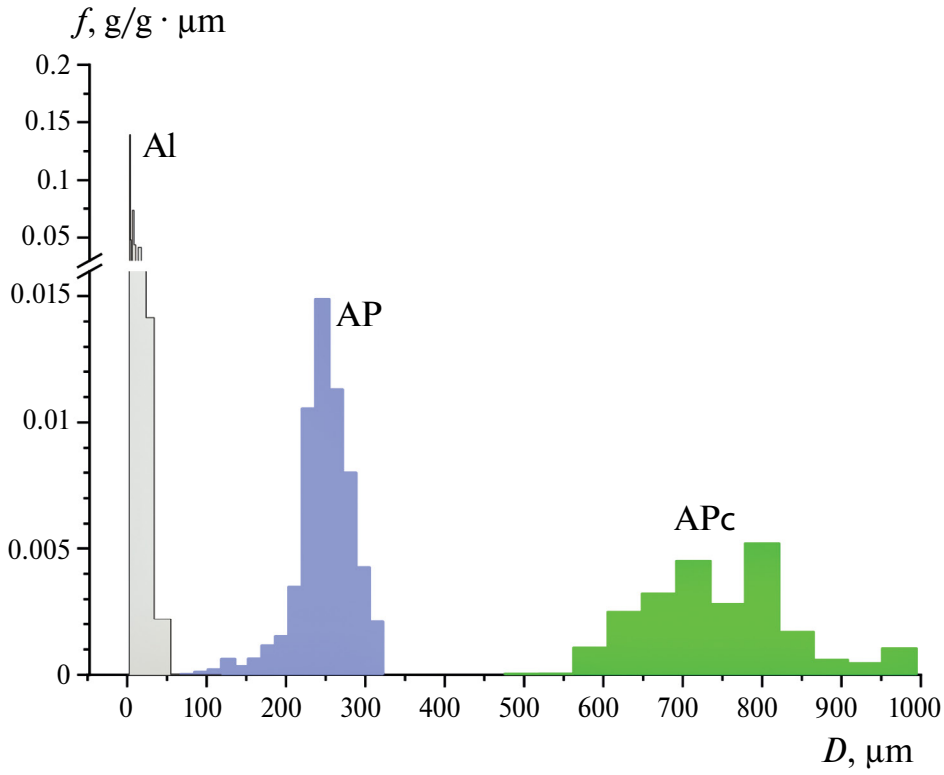

Fig. 1. Mass distribution functions of aluminum, coarse (APc) and medium (AP) ammonium perchlorate particles by size.

Table 2. Component composition (%.wt) of the studied propellants

Fuel	Binder	Al	APc	AP	$AlMgB1_4$	TiB_2	NH_4BF_4	$(NH4)_2TiF_6$	$Ca_3(PO_4)_2$
P1	20	20	60	–	–	–	–	–	–
P11	20	20	60	–	2	–	–	–	–
P12	20	20	60	–	–	2	–	–	–
P13	20	20	60	–	–	–	2	–	–
P14	20	20	60	–	–	–	–	2	–
P15	20	20	60	–	–	–	–	–	2
P2	20	20	–	60	–	–	–	–	–
P21	20	20	–	60	1.6				
P22	20	20	–	60		1.8	–	–	–
P23	20	20	–	60	–	–	2	–	–
P24	20	20	–	60	–	–	–	2.1	–
P25	20	20	–	60	–	–	–	–	2.5
P3	20	18	–	62	–	–	–	–	–
P31	20	18	–	62	2	–	–	–	–
P32	20	18	–	62		1.5			
P33	20	18	–	62	–	–	2.4	–	–
P34	20	18	–	62	–	–	–	1.5	–
P35	20	18	–	62	–	–	–	–	2.2

Note: Additives were introduced in excess of 100%

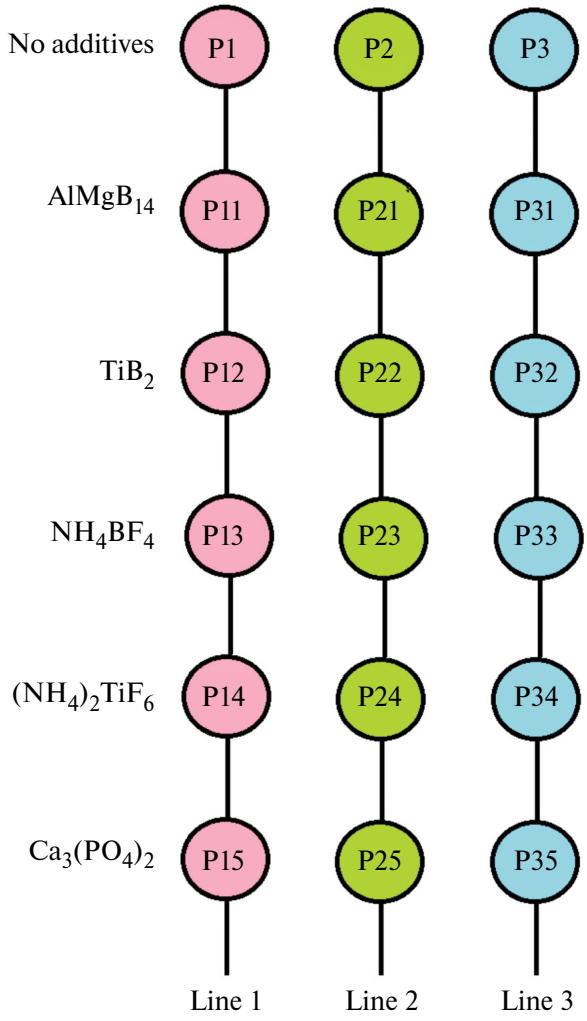

Fig. 2. Scheme of variation of propellant composition.

additives (Fig. 2). The compositions of the model propellants are presented in Table 2.

3. CONDUCTING AND PROCESSING THE RESULTS OF EXPERIMENTS

The experimental method is based on burning the test propellant sample in a small high-pressure vessel (mini-bomb) at a pressure of 0.35 MPa in nitrogen. At the same time, the combustion process is video-recorded through windows and condensed combustion products (CCP) are collected into the liquid.

The appearance of the high-pressure vessel (mini-bomb) is shown in Fig. 3. The outer diameter of the body is 90 mm, the effective diameter of the windows is 30 mm, the working pressure is up to 3 MPa, the volume is 0.33 L.

The sample is ignited using a nichrome wire heated by an electric current. A glass with a "freezing" liquid, distilled water, is placed under the sample. The glass diameter is 0.5 mm smaller than the inner diameter of the vessel. The sample in the form of a paste-like mixture is placed in a plexiglass cup with an inner diameter of 5 mm and a depth of 5 mm and fixed in the vessel so that the combustion torch is directed downwards. The distance from the surface of the sample to the surface of the liquid before the experiment was 1.5 cm. The pressure is created by gas from a cylinder and controlled by a manometer. The combustion process of the sample is recorded using a video camera. Burning metal particles-agglomerates flying out of the surface of the sample go out upon entering the liquid. Oxide particles in the free volume of the high-pressure vessel after combustion of the sample, upon sufficiently long exposure, settle on the surface of the liquid. The table 3 presents the results of the assessment of the velocity and time of settling of particles with a density of 3.7 g/cm^3 (aluminum oxide) in gas at a pressure of 0.35 MPa. The calculations were carried out using the AeroCalc aerosol calculator [52] to determine the holding time. The settling distance is 65 mm, which corresponds to the height of the free volume of the vessel, equal to the distance from the liquid surface to the top lid. The settling time was determined as the quotient of division the distance and the settling velocity. The settling velocity of spherical particles with a diameter of 2.2 μm and a density of 3.7 g/cm^3 is 0.54 mm/s. They will cover a distance of 65 mm in 120 s. The gas suspension was held in the vessel for 5 min so that particles larger than 2 μm guaranteed to have settled into the liquid.

Thus, in the conducted experiments, the agglomerates leaving the burning surface of the sample

Table 3. Estimation of the velocity and time of settling of particles in gas

Particle diameter, μm	Sedimentation velocity, mm/s	Re number	Sedimentation time, s
10	11.2	0.026	5.8
5	2.8	0.0032	23
3	1	0.0007	65
2.5	0.7	0.004	92
2.2	0.54	0.0027	120
2	0.4	0.0026	163

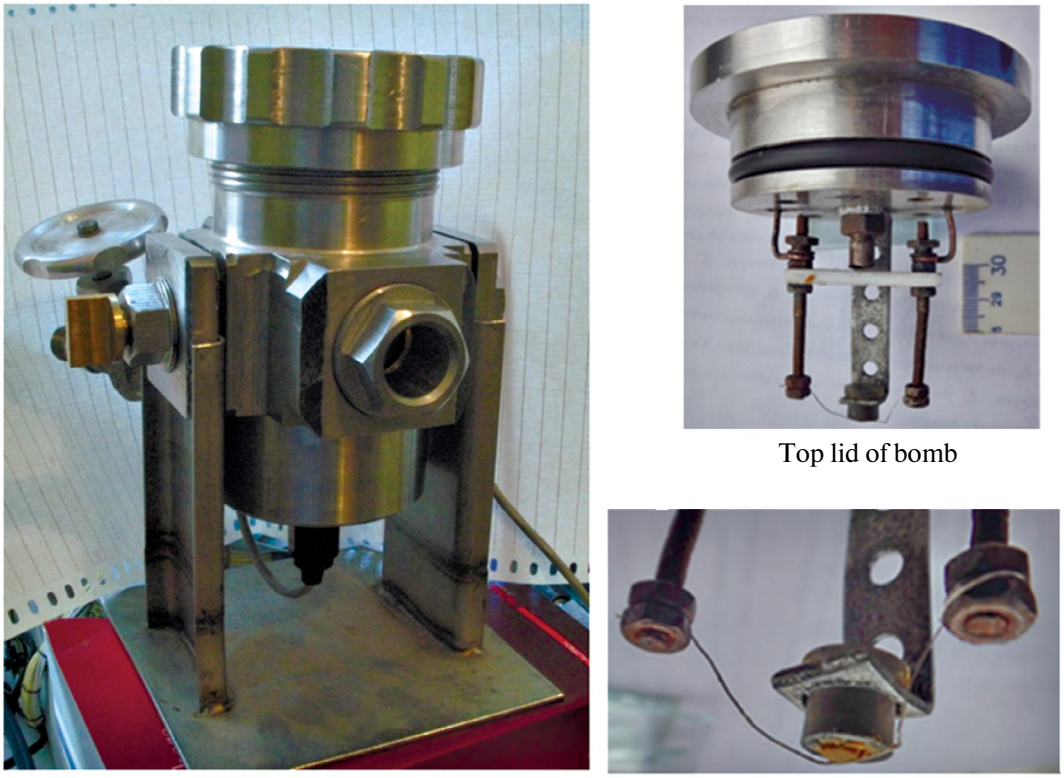

General external appearance

Top lid of bomb

Sample with igniting wire

Fig. 3. Photographs of a high-pressure vessel (mini-bomb) and its equipment.

are quenched and completely sampled. Oxide particles are not completely trapped. Some amount of oxide particles smaller than 2 μm exit with the gas when the pressure is released after the experiment. The "mass average" D_{43} was used as a characteristic size of the agglomerates, and the "surface average" d_{32} was used for the oxide particles. The specified sizes were calculated using formula (1).

4. PREPARATION AND ANALYSIS OF SAMPLED CCP PARTICLES

After removing the sampling glass, the suspension in it was filtered through a wire sieve with a mesh size of 80 μm. Particles larger than 80 μm were considered agglomerates. It is assumed that the boundary size D_L separating agglomerates and oxide particles depends on the propellant formulation and combustion conditions [53]. There are various values of D_L in the literature. For example, in [54, 55] agglomerates were considered to be particles larger than 30 μm, in [56] D_L = 49 μm was taken, in [17] the size of D_L was 119 μm. In this work, D_L = 80 μm is accepted as a certain "universal" value, justified also by considerations of practical convenience – "wet" sifting of an aqueous suspension of particles through an 80 μm sieve is carried out quite easily. The residue on the sieve was dried at room temperature, weighed and the dimensionless mass of the agglomerates m_{80} was determined as a relation the mass of particles larger than 80 μm to the mass of the propellant sample before the experiment.The absolute error in determining the value of m_{80} usually does not exceed 0.02.

The dried agglomerate particles were subjected to morphological, granulometric and chemical analyses. The morphology of the particles was studied under an MBS-10 optical microscope with a DCM-300 ocular camera. Particle size analysis was carried out using an Pictoval optical projection microscope (Carl Zeiss Jena, Germany) and a semi-automatic 23-channel counting device with measuring circles on a transparent template ruler [57, 58]. The absolute error in measuring the particle diameters is ±22 μm. The incompleteness of agglomerates combustion was determined by the cerimetric method of analytical chemistry [59, 60] using reducing number *RN*, which characterizes the ability of a material

to attach oxygen, that is, to oxidize. The measure of incompleteness of combustion η is the ratio of the RN numbers after combustion, that is, RN_{ccp} for combustion products, and RN_{prop} for propellant. The reducing number for CCP RN_{ccp} is calculated taking into account the mass of agglomerates:

$$RN_{ccp} = (RN \text{ for agglomerates}) \cdot m_{80}. \quad (2)$$

The reducing number for propellant RN_{prop} is calculated as the product of the reducing number for metallic fuel RN_{mf} determined as a result of chemical analysis and the mass fraction of metallic fuel m_{mf} in the propellant:

$$RN_{prop} = RN_{mf} \cdot m_{mf}. \quad (3)$$

As a result, the incompleteness of agglomerate combustion:

$$\eta = RN_{ccp}/RN_{prop}. \quad (4)$$

In this definition, incompleteness of combustion can vary from 1 (nothing burned) to 0 (everything burned). The ratio of the measured RN_{mf} and its theoretical value gives an idea of the "degradation" of the metallic fuel. For the used ASD-4 $RN = 10.14 \pm 0.28$ (averaged over 6 samples), while the theoretical value for aluminum is 11.12 [60]. The value 10.14/11.12 = 0.912, or 91.2%, can be interpreted as the content of active (unoxidized) metal in the original aluminum. The value $m_{mf} = 0.2$ for propellants of lines 1 and 2 and $m_{mf} = 0.18$ for propellants of line 3. Relative error of determination η typically 5%-7%.

The "pass" through the 80 μm sieve – a suspension of fine oxide particles in water – was analyzed on an automatic granulometer "Malvern-3600E" (Great Britain). Mode: size range 0.5–118 μm, ultrasonic treatment of suspension within 30 s before measurement, mechanical stirrer is on during measurement. Each sample was analyzed twice. The measurement was repeated after 3 minutes, the results were averaged. Relative measurement error of the sizes – 10%.

Based on the obtained empirical size distribution functions, we calculated mean diameters of fine oxide particles d_{mn} and agglomerate particles D_{mn} according to formula (1) in the ranges of 0.5–80 μm and 80–D_{max}, respectively. Here D_{max} is the right boundary of the last histogram interval in the distribution function of agglomerates.

Sample burning rate (r, mm/s) determined by dividing the length of the sample by its burning time. The length of the sample is the depth of the cup 5 mm; the burning time was determined by processing video recordings of the combustion process. The absolute error in determining the burning rate is 0.1 mm/s. Fig. 4 shows frames from a video recording of the sample combustion process.

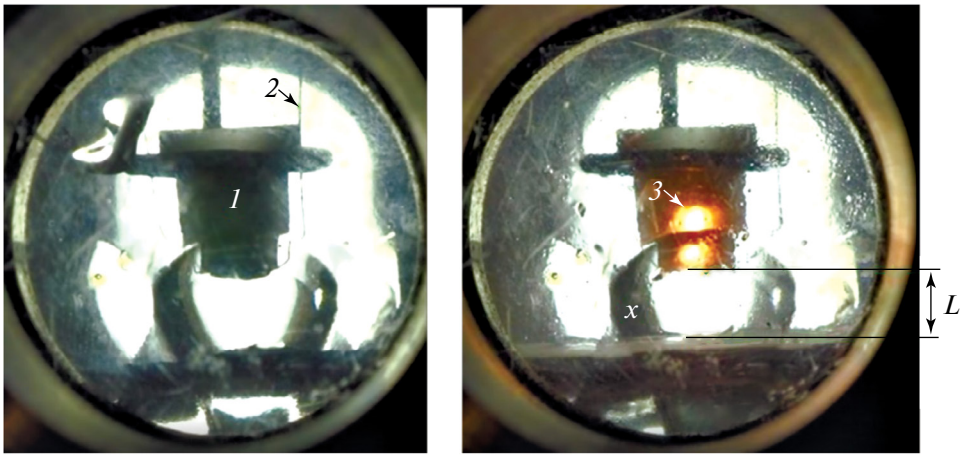

Fig. 4. Video footage of the combustion process of a miniature sample in a mini-bomb for the collection of combustion product particles. Shooting in the passing background light with illumination through the rear window of bomb: Left frame – view before combustion, right frame – during combustion: 1 – sample in a plexiglass cup, fixed to a bracket; 2 – ignition wire; 3 – burning surface. It is visible that it has shifted from the cut of the cup inward (upward); x – one of the parasitic reflections that form on the edges of the glass with freezing liquid; L – distance from the sample to the surface of the liquid before ignition of the sample.

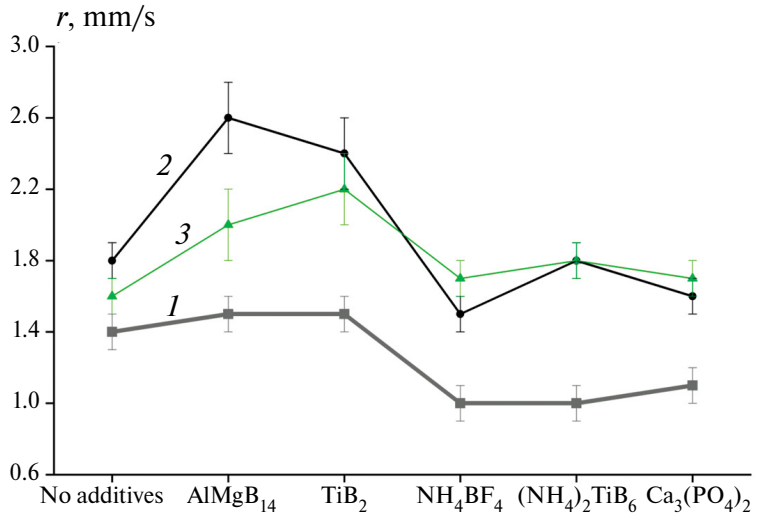

Fig. 5. Burning rates of the studied propellants at a pressure of 0.35 MPa: numbers 1, 2, 3 – correspond to propellants of lines 1, 2, 3.

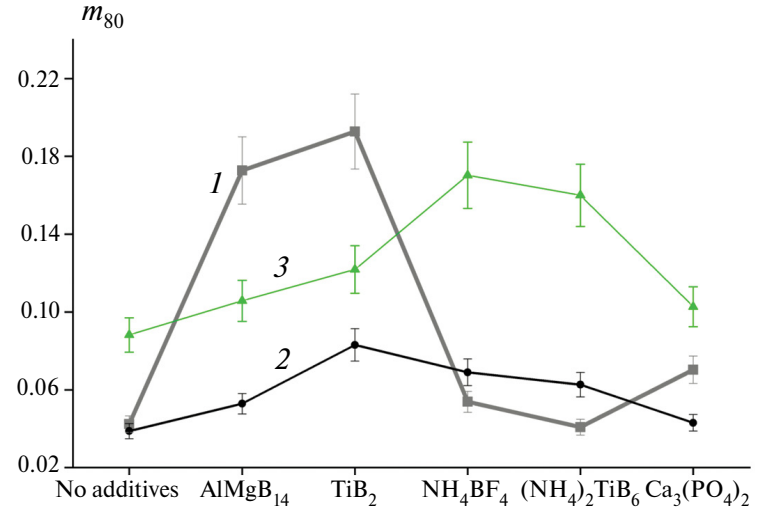

Fig. 6. Dimensionless mass m_{80} of agglomerate particles: numbers 1, 2, 3 – correspond to propellants of lines 1, 2, 3.

5. RESULTS AND DISCUSSION

5.1. Burning rate

Fig. 5 shows the burning rate levels of propellants with additives – modifiers. The additive formulas are signed under the abscissa axis, the burning rate is plotted along the ordinate axis. The points belonging to each of the three formula lines are connected.

As can be seen, the additives $AlMgB_{14}$ and TiB_2 increase the burning rate, while the additives $Ca_3(PO_4)_2$, $(NH_4)_2TiF_6$, NH_4BF_4 mainly decrease the burning rate compared to the corresponding base propellants. Here the words "mainly" are used due to the fact that the effect of the last three additives is ambiguous for different formulation lines. For propellants of line 3, the additives $Ca_3(PO_4)_2$, $(NH_4)_2TiF_6$, NH_4BF_4 have a weak effect on the burning rate, but still slightly (within the error) increase the rate.

5.2. Mass and size of agglomerates

The mass of agglomerates is characterized by a dimensionless parameter m_{80} (see Fig. 6). From this figure it can be seen that for propellants of lines 1, 2 and 3 all the studied additives lead to an increase in the mass of m_{80} agglomerates, with the exception of the additive $(NH_4)_2TiF_6$ for propellant of line 1.

Table 4 shows the mean sizes of agglomerates D_{mn}. Fig. 7 shows the effect of additives on the agglomerate mean size D_{43}.

The effect of additives in different propellant lines is ambiguous. Let us note the cases of the desired effect – reduction of D_{43}. For propellants of line 1, additives

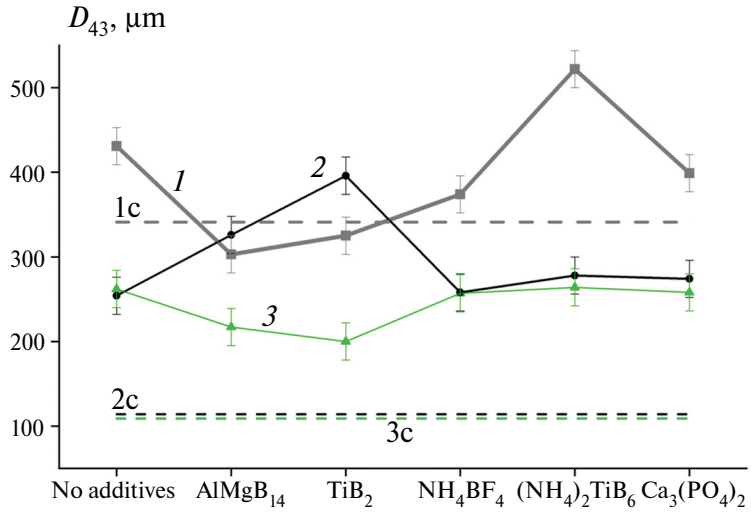

Fig. 7. Mean sizes of D_{43} agglomerate particles: broken curves 1, 2, 3 correspond to propellants of lines 1, 2, 3; horizontal dotted lines 1c, 2c, 3c – calculation according to model [57] for propellants of lines 1, 2, 3.

Table 4. Mean sizes D_{mn} of agglomerates (in μm)

Propellant	D_{10}	D_{30}	D_{32}	D_{43}	D_{53}
P1	246	306	373	431	457
P11	225	252	279	303	214
P12	245	272	301	325	336
P13	268	304	341	374	390
P14	310	376	453	522	551
P15	281	316	355	399	422
P2	186	210	235	254	263
P21	234	267	300	326	338
P22	267	307	350	396	420
P23	197	219	240	258	265
P24	212	235	258	278	287
P25	214	235	257	274	282
P3	157	194	234	262	274
P31	135	160	188	217	232
P32	138	161	184	200	206
P33	183	209	236	257	267
P34	191	214	237	258	267
P35	171	193	216	232	239

of $AlMgB_{14}$ and TiB_2 lead to a noticeable reduction of D_{43}, additives NH_4BF_4 and $Ca_3(PO_4)_2$ – to a slight decrease. For propellants of line 2, no additive led to a decrease in D_{43}. For propellants of line 3, additives of $AlMgB_{14}$ and TiB_2 lead to a decrease in D_{43}.

For comparison, the maximum possible agglomerate size was calculated using the tetrahedral pocket model [61], in which the pocket parameters and agglomerate size are calculated assuming that large oxidizer particles are located at the vertices of a regular tetrahedron. The internal volume of the tetrahedron is filled with a mixture of binder and metal and forms a pocket that generates an agglomerate. The calculated agglomerate size for propellants of lines 1, 2, 3 is 341 μm, 114 μm and 109 μm, respectively. As can be seen from Fig. 7, the experimental values for propellants of lines 2 and 3 significantly exceed the calculated ones, which indicates an "interpocket" [11] agglomeration mechanism. The model works better for propellants of line 1 with coarse AP. In this case, for three of the additives under consideration, the relative difference between the calculated and experimental values of D_{43} is 13%, 5% and 9% for propellants P11, P12 and P13, respectively. This indicates the suppression of "interpocket" agglomeration by the additives $AlMgB_{14}$, TiB_2, $(NH_4)_2TiF_6$.

5.3. The agglomerate combustion incompleteness of and sizes of oxide particles

Values of agglomerate combustion incompleteness for the studied propellants, η, versus the type of additives are presented in Fig. 8. Analysis of the data in Fig. 8 shows the following. For propellants of lines 1 and 3 only additive $Ca_3(PO_4)_2$ somewhat reduces the incompleteness of combustion η. For propellants of line 2, the value of η is reduced by additives $(NH_4)_2TiF_6$ and $Ca_3(PO_4)_2$.

Fig. 9 shows the results of the effect of additives on the d_{32} sizes of fine particles. Chemical analysis

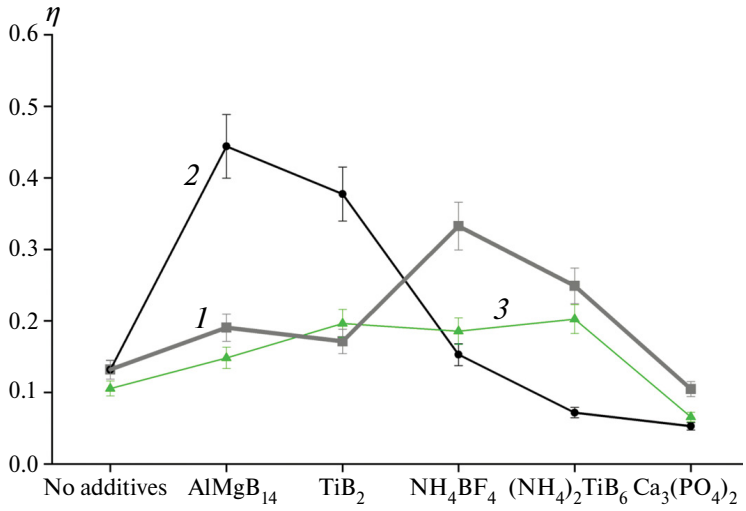

Fig. 8. Change in combustion incompleteness η: numbers 1, 2, 3 correspond to propellant lines 1, 2, 3.

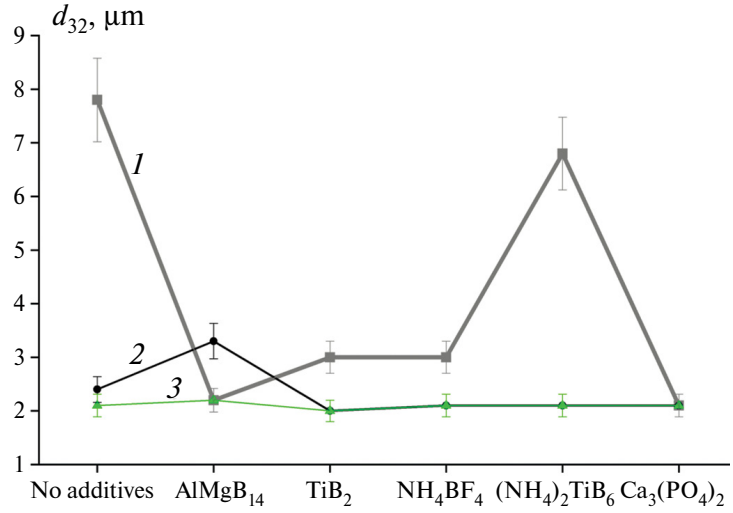

Fig. 9. Comparison of fine particle sizes d_{32}: curve numbers 1, 2, 3 correspond to the propellants of lines 1, 2, 3.

of these particles was not carried out, since it is expected that these particles are predominantly oxide [14].

The mean size d_{32} of oxide particles in most cases is in the range of 2–3.5 μm and changes slightly with the introduction of additives. The "outliers" for line 1 propellants (base and propellant with the additive $(NH_4)_2TiF_6$ are probably due to the peculiarities of particle preparation. At the initial stage of the studies, we did not pay due attention to strict adherence to the holding time of the gas suspension in the bomb. Insufficient holding time could lead to incomplete sedimentation of relatively small particles in the liquid, their subsequent loss during the release of gas from the bomb, and, as a consequence, to an overestimated value of the mean particle size that had time to settle in the liquid. Without taking into account the "outliers", we note the multidirectional influence of the $AlMgB_{14}$ additive – a positive effect (a decrease in d_{32} compared to the conditional "average" level) in the case of line 1 propellants, a negative effect in the case of line 2 propellants, and no effect for line 3 propellants.

Table 5 presents the main parameters – dimensionless mass of agglomerates m_{80}, burning rate r, mean size of agglomerates D_{43}, incompleteness of agglomerate combustion η, mean size of fine oxide particles d_{32}, as well as the "relative effect" showing the influence of the additive on each of the listed parameters under consideration. Definition of the relative effect for the abstract parameter p:

Table 5. The main parameters of the studied propellants and the influence of various additives on them

Propellant	m_{80}	Z_{m80}	r, mm/s	Z_r	D_{43}, μm	$Z_{D_{43}}$	η	$Z\eta$	d_{32}, μm	$Z_{d_{32}}$
P1	0.088	0	1.4	0	431	0	0.13	0	7.8	0
P11	0.106	0.20	1.5	0.07	303	–0.30	0.19	0.46	2.2	–0.72
P12	0.122	0.38	1.5	0.07	325	–0.25	0.17	0.31	3	–0.62
P13	0.17	0.93	1	–0.29	374	–0.13	0.33	1.54	3	–0.62
P14	0.16	0.81	1	–0.29	522	0.21	0.24	0.85	6.8	–0.13
P15	0.103	0.16	1.1	–0.21	399	–0.07	0.10	–0.23	2.1	–0.73
P2	0.042	0	1.8	0	254	0	0.13	0	2.4	0
P21	0.173	3.08	2.6	0.44	326	0.28	0.44	2.38	3.3	0.38
P22	0.193	3.55	2.4	0.33	396	0.56	0.37	1.85	2	–0.17
P23	0.054	0.27	1.5	–0.17	258	0.02	0.15	0.15	2.1	–0.12
P24	0.041	–0.04	1.8	0	278	0.09	0.07	–0.46	2.1	–0.12
P25	0.07	0.66	1.6	–0.11	274	0.08	0.05	–0.62	2.1	–0.12
P3	0.039	0	1.6	0	262	0	0.10	0	2.1	0
P31	0.053	0.36	2	0.25	217	–0.17	0.14	0.40	2.2	0.05
P32	0.083	1.14	2.2	0.38	200	–0.24	0.19	0.90	2	–0.05
P33	0.069	0.78	1.7	0.06	257	–0.02	0.18	0.80	2.1	0
P34	0.063	0.62	1.8	0.12	232	–0.11	0.06	–0.40	2.1	0
P35	0.043	0.11	1.7	0.06	258	–0.02	0.2	1	2.1	0

Note. Errors of values: m_{80} – 0.02 (abs.), r – 0.1 mm/s (abs.), D_{43} – 22 μm (abs.), η – 7% (rel.), d_{32} – 10% (rel.).

$$Z_p = \frac{\left(p_{\text{for propellant with additive}} - p_{\text{for base propellant}}\right)}{p_{\text{for base propellant}}},$$

where p is m_{80}, r, D_{43}, η, or d_{32}.

The presented results show that:

1. For propellants of lines 1 and 3, the studied additives lead to a decrease in the mean size of D_{43} agglomerates, with the exception of propellant P14 with the additive $(NH_4)_2TiF_6$. The greatest effect of reducing the mean D_{43} is observed for the $AlMgB_{14}$ additive and is $Z_{D_{43}} = -0.30$ (propellant P11). A good result is also given by the TiB_2 additive (the effect is $Z_{D_{43}} = -0.25$ and $Z_{D_{43}} = -0.24$ for propellants P12 and P32, respectively). For propellants of line 2, no additive leads to a decrease in the mean size of agglomerates.

2. The studied additives lead to an increase in the mass of agglomerates in most cases, with the exception of the additive $(NH_4)_2TiF_6$ when introducing it into the base propellant P2. However, even in this case the effect is insignificant, $Z_{m_{80}} = -0.04$ For propellant P24.

3. Additives $AlMgB_{14}$ and TiB_2 increase the burning rate of all propellants. Additives $Ca_3(PO_4)_2$, $(NH_4)_2TiF_6$, NH_4BF_4 increase the burning rate only in propellants of line 3. The maximum effect of increasing the rate is observed in propellant P21 with the additive $AlMgB_{14}$ and is $Z_r = 0.44$.

4. For propellants of lines 1 and 2 additive $Ca_3(PO_4)_2$ reduces the incompleteness of combustion η. The effects are $Z_\eta = -0.23$ (propellant P15) and $Z_\eta = -0.62$ (propellant P25, and this is maximum effect). For propellants of lines 2 and 3 the value η reduces additive $(NH_4)_2TiF_6$, effects $Z_\eta = -0.46$ (P24) and $Z_\eta = -0.40$ (P34).

5. The effect of additives on the d_{32} size of fine particles could not be studied. As a trend, it can be said that propellants of line 1 with large AP generate larger oxide particles compared to propellants of lines 2 and 3 with medium AP. The characteristic particle sizes d_{32} are approximately 3 μm and 2 μm, respectively.

Table 6 formally summarizes the results obtained. The (+) sign in a cell denotes a positive effect, the (–) sign denotes a negative effect, and (0) denotes no effect. The (0) sign also stands in cases of a weak effect, when its value is less than the error of the parameter under

Table 6. Qualitative influence of additives on the parameters under consideration

Additive	Propellant	m_{80}	r	D_{43}	η	d_{32}	Propellant	m_{80}	r	D_{43}	η	d_{32}	Propellant	m_{80}	r	D_{43}	η	d_{32}	***S***
$AlMgB_{14}$	P11	–	0	+	–	+	P21	–	+	–	–	–	P31	–	+	+	–	0	**5**
TiB_2	P12	–	0	+	–	+	P22	–	+	–	–	+	P32	–	+	+	–	0	**6**
$(NH_4)_2TiF_6$	P13	–	–	+	–	+	P23	–	–	0	–	+	P33	–	0	0	–	0	**3**
NH_4BF_4	P14	–	–	–	–	+	P24	0	0	0	+	+	P34	–	+	+	+	0	**6**
$Ca_3(PO_4)_2$	P15	–	–	+	+	+	P25	–	–	0	+	+	P35	–	0	0	–	0	**5**

Note. Positive effects (marked+): reduction of agglomerate mass, increase of burning rate, reduction of agglomerate sizes, reduction of combustion incompleteness, reduction of oxide particle size

consideration. The cells of the table with a positive effect are shaded. The last column of the table is the S (scores) parameter, the total number of "points" scored by a particular additive. The parameter is numerically equal to the sum of the "+" signs in the row of Table 6. As can be seen, the most effective in terms of the totality of the parameters studied turned out to be NH_4BF_4 additives, TiB_2 and $AlMgB_{14}$. Features of the substance NH_4BF_4 – high fluorine content. The NH_4BF_4 molecule contains about 72% fluorine, and in the molecule $(NH_4)_2TiF_6$ approximately 58% fluorine. This suggests the influence of the element F on the processes occurring during combustion. A feature of TiB_2 and $AlMgB_{14}$ powders is their high dispersion. Both powders were obtained by plasma recondensation [49], so their particles are mainly submicron in size.

6. CONCLUSION

The effect of the modifying additives titanium diboride TiB_2, aluminum and magnesium boride $AlMgB_{14}$, ammonium titanium (IV) fluoride $(NH_4)_2TiF_6$, ammonium tetrafluoroborate NH_4BF_4, calcium phosphate 3-substituted $Ca_3(PO_4)_2$ on the combustion parameters at a pressure of 0.35 MPa was investigated for the composite propellant consisting of aluminum ASD-4 as a fuel (≈20%), ammonium perchlorate as an oxidizing agent (≈60%) and an active binder based on MPVT (≈20%). The mass fraction of additives in the propellant is about 2% over 100%. In the experiments, the burning rate of propellant samples was measured using video recording and characteristics of condensed combustion products, by the quenching and sampling particles in a liquid. By analyzing the sampled particles, the mass, size and incompleteness of combustion of aluminum agglomerates larger than 80 μm, as well as the sizes of small (2–80 μm) oxide particles were determined. As a result, it was revealed how exactly each of the listed additives affects the determined parameters. The effect was assessed from the standpoint of increasing the burning rate, reducing the mass, size and incompleteness of combustion of agglomerates, as well as reducing the size of small particles. It was noted that the additives have a stronger effect on propellant with coarse AP (500–630 μm) than on propellants with medium AP (180–250 μm). The studied additives can be arranged in the following row in descending order of the totality of registered positive effects:

$$NH_4BF_4 = TiB_2 > AlMgB_{14} = Ca_3(PO_4)_2 > (NH_4)_2TiF_6.$$

Despite some positive effects, none of the five additives provides a simultaneous significant reduction in both the size and mass of agglomerates. At the same time, the analysis, although based on a limited set of experimental data (one pressure level of 0.35 MPa, one type of binder), demonstrated the fundamental possibility of additives influencing the selected combustion parameters. Therefore, work on finding new additives capable of reducing the intensity of agglomeration should be continued. Highly dispersed powders of substances with a high fluorine content seem promising.

FUNDING

This work was financed by the Ministry of Science and Higher Education of the Russian Federation within the framework of the state task (FWGF-2021–0001). No additional grants to carry out or direct this particular research were obtained.

CONFLICT OF INTEREST

The authors of this work declare that they have no conflicts of interest.

REFERENCES

1. B. P. Zhukov, editor. *Energetic condensed systems. Brief Encyclopedic Dictionary*. (Yanus-K, Moscow, 2000). [In Russian]
2. S. F. Sarner *Propellant Chemistry*. (New York, 1966).
3. V. I. Tsutsuran, N. V. Petrukhin, Gusev S. A. *Military-technical analysis of the state and prospects for the development of rocket propellants*. (MO RF, Moscow, 1999). [In Russian]
4. E. M. Nurullayev *Main characteristics of composite solid propellants and areas of their application. 2nd ed*. (Infra-Inzheneriya, Moscow, Vologda, 2021). [In Russian]
5. Yu. V. Frolov, P. F. Pokhil, V. S. Logachev, Combust Explos Shock Waves. **8**, 2, 168. (1972).
6. A. G. Korotkikh, I. V. Sorokin, E. A. Selikhova, V. A. Arkhipov, Russ. J. Phys. Chem. B. **14**, 4, 600. (2020). https: // doi.org/ 10.1134/S1990793120040089
7. A. G. Korotkikh, I. V. Sorokin, V. A. Arkhipov, Russ. J. Phys. Chem. B. **16**, 2, 259. (2022). https: // doi.org/ 10.1134/S1990793122020075
8. V. D. Gladun, Yu.V Frolov et al., *Agglomeration of a part of powdered metal during combustion of mixed condensed systems* [preprint]. (Institut khimicheskoy fiziki AN SSSR, Chernogolovka, 1977). [In Russian]
9. P. F. Pokhil, V. M. Maltsev, V. S. Logachev et al., Combust Explos Shock Waves. **7**, 1, 43 (1971).
10. Yu. V. Frolov, B. E. Nikolsky, Combust Explos Shock Waves. **19**, 5, 625 (1983).
11. V. A. Babuk, V. P. Belov, V. V. Khodosov et al., Combust Explos Shock Waves. **21**, 3, 287 (1985).
12. K. Jaraman, S. R. Chakravarthy, R. Sarathi, Combust Explos Shock Waves. **46**, 1, 21 (2010).
13. O. G. Glotov, V. E. Zarko V. V. Karasev et al., *Comb. and detonation. 28th International Annual Conference of ICT*. (Karlsruhe, Germany, 1997), Report **75**.
14. V. E. Zarko, O. G. Glotov, Science and Tech. of Ener. Materials. **74**, 6, 139 (2013).
15. Y. G. Liu, X. Tian, L. Yin et al., Combust Explos Shock Waves. **58**, 2, 190 (2022).
16. V. A. Babuk, D. I. Kuklin, S. Yu. Naryzhny et al., Combust Explos Shock Waves. 59, 2, 236 (2023).
17. O. G. Glotov, Combust Explos Shock Waves. 42, 4, 436 (2006).
18. I. Yu. Gudkova, I. N. Zyuzin, D. B. Lempert, Russ. J. Phys. Chem. B. **14**, 2, 302. (2020). https: // doi.org/ 10.1134/S1990793122010067
19. I. Yu. Gudkova, I. N. Zyuzin, D. B. Lempert, Russ. J. Phys. Chem. B. **16**, 1, 58. (2022). https: // doi.org/ 10.1134/S1990793120020062
20. T. I. Gorbenko, Vestnik SibSAU im. M. F. Reshetneva. **23**, 2, 173 (2009). [In Russian]
21. V. N. Popok, V. N. Khmelev *Composite condensed chemical propellants based on ammonium nitrate. Principles of layout and properties*. (Izd-vo Altayskogo gos. tekhnicheskogo un-ta im. I. I. Polzunova, Biysk, 2014). [In Russian]
22. G. V. Sakovich, V. A. Arkhipov, A. B. Vorozhtsov et al., Izvestiya TGU. **314**, 3, 18 (2009). [In Russian]
23. G. Ya. Pavlovets, V. Yu. Meleshko, B. I. Larionov et al., Khim. fizika i mezoskopiya. **8**, 1, 53 (2006). [In Russian]
24. V. D. Gladun, Yu. V. Frolov, L. Ya. Kashporov, Combust Explos Shock Waves. **13**, 5, 596 (1977).
25. V. N. Popok, A. P. Vandel, A. Yu. Kolesnikov, Butlerovskiye soobshcheniya. **36**, 11, 58 (2013). [In Russian]
26. V. N. Popok, N. I. Popok, Yu. A. Pivovarov, Butlerovskiye soobshcheniya. **49**, 15 (2017). [In Russian]
27. X. Liu, W. Ao, H. Liu et al., Propellants, Explos., Pyrotech. **42**, 3, 260 (2017).
28. U. R. Nair, R. Sivabalan, Gore G. M. et al., Combust Explos Shock Waves. **41**, 2, 121 (2005).
29. S. Lal, R. J. Staples, J. M. Shreeve, Chem. Eng. J. **468**, 143737, (2023).
30. V. A. Babuk, V. P. Belov, G. G. Shelukhin, Combust Explos Shock Waves. **17**, 3, 264 (1981).
31. E. W. Price, R. K. Sigman, J. R. Sambamurthi et al. *Behavior of aluminum in solid propellant combustion*. (AFOSR-TR-82–0964, Georgia Institute of Technology, 1982).
32. L. L. Breiter, L. Ya. Kashporov, V. M. Maltsev et al., Combust Explos Shock Waves. **7**, 2, 186 (1971).
33. Y. Aly, M. Schoenitz, E. L. Dreizin, Comb. Flame. **160**, 835 (2013). http://dx.doi.org/10.1016/j.combust-flame.2012.12.011.
34. W. Ao, Z. Fan, L. Lu et al., Comb. Flame. **220**, 288 (2020). https://doi.org/10.1016/j.combust-flame.2020.07.004.

35. W. He, J. Y. Lyu, D. Y. Tang et al., Comb. Flame. **221**, 441 (2020).
36. A. Yu. Dolgoborodov, Combust Explos Shock Waves. **51**, 1, 86 (2015).
37. D. A. Yagodnikov *Ignition and combustion of powdered metals in gas-dispersed media*. (MGTU im. N. E. Baumana, Moscow, 2018). [In Russian]
38. O. G. Glotov, D. A. Yagodnikov, V. S. Vorob'ev et al., Combust Explos Shock Waves. **43**, 3, 320 (2007).
39. V. G. Shevchenko, D. A. Eselevich, N. A. Popov et al., Combust Explos Shock Waves. **54**, 1, 58 (2018).
40. V. Rosenband, A. Gany Intern. J. Energetic Mater. Chem. Propuls. **6**, 2, 143 (2007).
41. E. Shafirovich, P. E. Bocanegra, C. Chanveau et al. Proc Combust Inst. **30**, 2, 2055 (2005).
42. T. A. Andrzejak, E. Shafirovich, A. Varma Combust. Flame. **150**, 60 (2007).
43. E. A. Lebedeva, I. L. Tutubalina, A. Valtsifer et al. Combust Explos Shock Waves. **48**, 6, 694 (2012).
44. J. Y. Lyu, G. Xu, H. Zhang et al. Fuel. 356, 129587 (2024).
45. A. G. Korotkikh, O. G. Glotov, V.A Arkhipov. et al. Combust. Flame. **178**, 195 (2017). https: //doi.org/10.1016/j.combust-flame.2017.01.004
46. W. Q. Pang, L. T. DeLuca, X. Z. Fan, et al. Combust. Flame. **220**, 157 (2020).
47. K. Tejasvi, V. V. Rao, Y. PydiSetty et al. Combust Explos Shock Waves. **57**, 2, 203 (2021).
48. L. T. DeLuca, L. Galfetti, F. Severini et al. Combust Explos Shock Waves. **41**, 6, 680 (2005).
49. Sh. L. Guseynov, S. G. Fedorov *Nanopowders of aluminum, boron, aluminum and silicon borides in high-energy materials*. (Torus Press, Moscow, 2015). [In Russian]
50. F. K. Bulanin, A. E. Sidorov, N. I. Poletaev et al. Combust Explos Shock Waves. **57**, 2, 190 (2021).
51. L. D. Romodanova, P. F. Pokhil Combust Explos Shock Waves. **9**, 2, 195 (1973).
52. Aerosol Calculator Program // http: // www. cheresources.com/che-links/content/particle-technology/aerosol-calculator-program. 2012. URL: http: // cires.colorado.edu/jimenez-group/Reference/aerocalc.zip (accessed on: 22.03.2024).
53. O. G. Glotov, V. E. Zarko, V. V. Karasev, Combust Explos Shock Waves. **36**, 146 (2000).
54. V. A. Babuk, V. A. Vasilyev, M. S. Malachov J. Propul. Power. **15**, 6, 783 (1999).
55. V. A. Babuk, V. A. Vassilyev, V. V. Sviridov Combust Sci Technol. **163**, 261 (2001).
56. J. K. Sambamurthi, E. W. Price, R. K. Sigman AIAA Journal, **22**, 8, 1132 (1984)
57. K. P. Kutsenogii *Candidate of dissertation tech. Sci.* (Institute of Chemical Kinetics and Combustion Siberian Branch of the Russian Academy of Sciences, Novosibirsk, 1970). [In Russian]
58. L. Ya. Gradus *A Guide to Dispersion Analysis Microscopy.* (Khimiya, Moscow, 1979). [In Russian]
59. T. D. Fedotova, O. G. Glotov, V. E. Zarko Propellants, Explos. Pyrotech. **32**, 2, 160 (2007).
60. W. Pang, L. T. De Luca, X. Fan et al. *Boron-Based Fuel-Rich Propellant: Properties, Combustion, and Technology Aspects.* (CRC Press, 2019).
61. O. G. Glotov, I. V. Sorokin, A. A. Cheremisin Combust Explos Shock Waves. **59**, 6, 752 (2023).

ADVANCES IN CHEMICAL PHYSICS, 2025, Vol. 44, No. 1, pp. 67–72

ELECTRICAL AND MAGNETIC PROPERTIES OF MATERIALS

FEATURES OF INTERPRETATION OF PULSED RADIATION-INDUCED CONDUCTIVITY OF POLYMERS AT LOW TEMPERATURE

© 2025 I. R. Mullakhmetov*, V. S. Saenko, A. P. Tyutnev, and E. D. Pozhidaev

Tikhonov Moscow Institute of Electronics and Mathematics, National Research University Higher School of Economics, Moscow, Russia

**e-mail: imullakhmetov@hse.ru*

Received March 06, 2024
Revised April 12, 2024
Accepted April 22, 2024

Abstract. The pulsed radiation-induced conductivity of polyethylene and polypropylene was studied at low (about 100 K) temperatures under the influence of electron pulses with an energy of 50 keV and a duration of 1 ms. To explain the results obtained, the Rose-Fowler-Vaisberg model was used. It is shown that when using it, it is necessary to take into account the difference in the shifts of carriers in a unit electric field before the first trapping ($\mu_0 \tau_0$) and those moving by recapture along traps ($\mu_0 \tau_0$) appearing in the theoretical Rose–Fowler–Vaisberg model. Both of these parameters were calculated based on the results of experimental results.

Keywords: *electrons with energy 50 keV, numerical calculations, semi-empirical model of radiation electrical conductivity of polymers*

DOI: 10.31857/S0207401X250108e2

1. INTRODUCTION

From the mid-70s to the late 80s, the scientific school led by A. P. Tyutnev, V. S. Saenko and E. D. Pozhidaev performed a series of works on the radiation-pulse electrical conductivity (RPEC) of engineering polymers when they are irradiated with pulses of accelerated electrons, usually at room temperature [1–4]. The obtained results were interpreted on the basis of the quasi-zone Rose-Fowler-Weisberg model (RFW) [1, 5] with the involvement of the basic theoretical concepts borrowed from the ion-pair mechanism of radiolysis of liquid hydrocarbons (Onzager theory, Langevin recombination). It is quite obvious that these data relating to the bulk irradiation of polymer films in the small-signal regime most directly characterize the transport of excess charge carriers in polymers. It is found that in the response of polymers it is possible to distinguish the instantaneous and delayed components of the RPEC. The first of them is described by first-order kinetics with a time constant of the order of fractions of a nanosecond. The second one is caused by hopping transport of charge carriers both in the composition of hemin (twin) pairs (the case of low temperatures) and free charges (room temperature).

Currently, the RPEC of polymers under pulse irradiation has been well studied not only at room temperature [3, 4, 6] but also at low temperature [7–9]. It turned out that the RPEC of polymers is also well described by a semiempirical model of RFW based on the multiple capture formalism (most convincingly shown in [8]). This fact is extremely surprising, because at low temperature (77–103 K) the application of the quasi-zone multiple-capture model should encounter serious difficulties, since in this temperature region the dominant position is occupied by the tunneling mechanism of charge carrier transport [10]. This situation required a careful consideration of the situation both from the theoretical point of view and additional experimental studies.

The aim of the present work is to study the RPEC of polyethylene and polypropylene at low temperature (around 100 K), similar to what was done earlier for normal conditions [11] and to give an explanation of the obtained results using a modified RFW model.

The system of equations of the classical RFW model has the following form:

$$\frac{dN(t)}{dt} = g_0 - k_r N_0(t) N(t)$$
$$\frac{\partial \rho(E,t)}{\partial t} = k_c N_0(t)\left[\frac{M_0}{E_1}\exp\left(-\frac{E}{E_1}\right) - \rho(E,t)\right] - \nu_0 \exp\left(-\frac{E}{kT}\right)\rho(E,t) \quad (1)$$
$$N(t) = N_0(t) + \int_0^\infty \rho(E,t)dE$$

By definition, the radiation conductivity

$$\gamma_r(t) = e\mu_0 N_0(t),$$

where $N_0(t)$ is the concentration of the main charge carriers (hereinafter electrons) in the conducting state (in the transfer zone) with microscopic mobility μ_0; $N(t)$ is their total concentration; g_0 is the rate of bulk generation of electrons and holes; k_r is the bulk recombination coefficient of quasi-free electrons with fixed holes acting as recombination centers; k_c is the rate constant of trapping of quasi-free electrons on traps; M_0 is total concentration of biographical traps exponentially distributed in energy ($E > 0$ and counted down from the bottom of the transfer zone); $\tau_0 = (k_c M_0)^{-1}$ is lifetime of quasi-free electrons before capture; $\rho(E,t)$ – density of distribution of trapped electrons on traps of different depth; ν_0 is effective frequency factor of thermal release of trapped electrons from traps; E_1 is a parameter of exponential distribution of traps in energy. The dispersion parameter $\alpha = kT / E_1$, where k is the Boltzmann constant and T is the temperature.

According to the RFW model, ionizing radiation creates pairs of free charges (i.e, charges moving under the action of an external electric field only), of which only electrons are mobile. The holes formed do not participate in the transfer of electric current and serve as recombination centers. Initially, electrons appear in a mobile state with microscopic mobility μ_0, but their motion occurs in the presence of numerous traps, the depth of which is distributed in a wide energy range according to the exponential law.

A distinctive feature of the RFW model is that the parameters μ_0 and τ_0 enter the analytical formulas only as their product [1–4], while α, τ_0, and ν_0 appear in the expression for the transit time even as a triple product $\mu_0\tau_0\nu_0^\alpha$ [1, 4, 11]. To determine the frequency factor ν_0, we have proposed a special procedure that uses short pulses of radiation [9, 12].

The recombination rate constant k_r reflects the bimolecular nature of the process, but can be much smaller than its Langevin value (so-called non-Langevin recombination [1]). The RPEC of polymers at low temperatures decreases to the level of the instantaneous component of the radiation conductivity γ_p, which within the framework of the RFW model is equal to $\gamma_p / R_0 = K_p = \eta_0\mu_0\tau_0 e$, where R_0 is the dose rate, K_p is the reduced instantaneous component of the RPEC, and η_0 ($m^{-3}Gr^{-1}$) is the initial concentration of hemin electron-hole pairs formed in the polymer for every 100 eV of absorbed ionizing radiation energy [1, 8, 9]. The parameter K_p under these conditions becomes one of the main experimental quantities characterizing the RPEC and, moreover, the most easily determined by measurements.

It turned out that the value $\mu_0\tau_0$, appearing in K_p, is not always equal to $\mu_0\tau_0$, determined by the RFW model from analyzing the properties of the delayed component $\gamma_{rd} = \gamma_r - \gamma_p$ [4]. To reflect this difference, it is denoted as $\overline{\mu_0\tau_0}$. Typically $\mu_0\tau_0 = k\overline{\mu_0\tau_0}$ and $k \le 1$.

The temperature dependence of the RPEC of polymers enters the equations of the RFW model through the parameter η_0 (generally speaking, at nitrogen temperatures, it is a weak dependence) and the frequency factor ν_0, which carries the major part of the activation dependence. Charge carrier transport in disordered solids at low temperature is believed to occur by thermally activated tunnel jumps involving molecular motions of polymer structural units acting as hopping centers [13, 14]. The concept of transport level [15, 16], which has been intensively developed recently, allows us to reduce these theoretical results to the multiple capture equations, on which the RFW model is based. A direct experimental determination of ν_0 appears to be an urgent experimental problem, allowing us to parameterize *a* modified RFW model that distinguishes between the parameters $\mu_0\tau_0$ and $\overline{\mu_0\tau_0}$.

2. EXPERIMENTAL RESULTS AND THEIR DISCUSSION

2.1 Experimental methodology

To conduct the experiments we used the methodology described in [7]. Films of technical high-pressure polyethylene (HDPE) of domestic production and polypropylene (PP) of "Torayfan" trademark with thicknesses of 20 μm and 12 μm, respectively, were used. Samples of 40 mm diameter

Table 1. Absorbed dose rate for tested polymers (data kindly provided by D. N. Sadovnichiy)

Material	Thickness, μm	Absorbed dose rate (Gy/s) per 1 nA of primary electron current registered by the shutter	
		without PET film	PET film
LDPE	20	2.8	2.1
PP	12	2.3	1.7

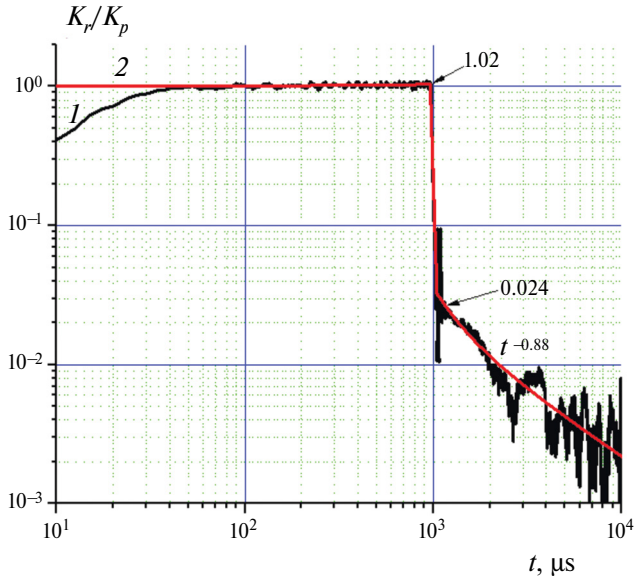

Fig. 1. Experimental (*1*) and calculated (*2*) radiation-pulse electrical conductivity of LDPE at 103 K, dose rate 2.1×10^4 Gy/s

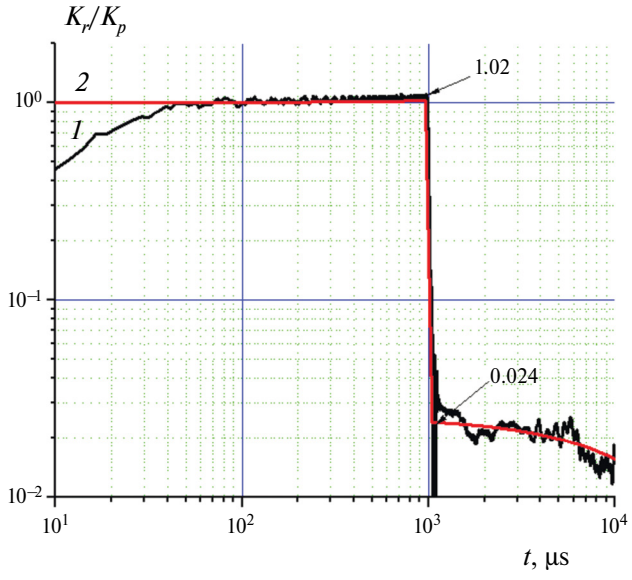

Fig. 2. Experimental (*1*) and numerically obtained (*2*) radiation-pulse electrical conductivity of PP at 103 K, dose rate 1.7×10^4 Gy/s

with sputtered aluminum electrodes of 32 mm diameter were irradiated with monoenergetic electrons with energy of 50 keV at the duration of rectangular irradiation pulses of 1 ms at low (103 K) temperature. All experiments were performed at an electric field strength in the sample of 4×10^7 V/m.

Table 1 shows the calculated values of the absorbed dose rate from the current of 1 nA electrons falling on the flap and registered directly when they flow to the ground. When estimating the averaged dose rate, the depth course of the dose rate calculated by the Monte Carlo method [3] was taken into account. The data are given both in the presence and absence of a 5 μm thick light- and heat-reflecting polyethylene terephthalate (PET) film over the irradiated sample, since the measurements at room temperature were carried out without the PET film.

2.2 Experimental results and their analysis

Figs. 1 and 2 show that in both cases the instantaneous component of the RPEC dominates, and after the end of the radiation pulse the conductivity sharply decreases by more than an order of magnitude. Under low temperature conditions, the concentration of charge carriers cannot change appreciably during the beam turn-off time [8, 9]. Thus, the observed effect is related to the specificity of transport of thermalized electrons.

When working with rectangular radiation pulses in the small signal mode (as in the present work), the transient RPEC current density j_r at any moment of time is proportional to the dose rate, so it is convenient to consider not the current density j_r, but its reduced value $K_r = j_r / R_0$, calculated per unit dose rate. The dimensionality of K_r coincides with the dimensionality of the reduced instantaneous component K_p or its theoretical analog K_p' (see below), which appears in the RFW model.

The procedure for determining k is illustrated on the example of RPEC of LDPE at room temperature (Figs. 3 and 4), since the experimentally recorded drop in conductivity after the end of the pulse

(Fig. 3) is well labeled. These data are based on unpublished results of [4].

Having determined the parameter K_p, we estimate the value of $\overline{\mu_0\tau_0} = \frac{0.1}{3\rho} K_p$ [1], where ρ is the density of the polymer (see Table 2). It is assumed that the absorbed energy of 100 eV leads to the formation of three electron-hole pairs [1].

After that, the dispersion parameter α is determined by the decline of the delayed component after the end of irradiation, represented in logarithmic coordinates $\lg j_{rd} - \lg t$ at $t \geq 3t_p$ ($j_{rd} \propto t^{-1+\alpha}$), where t_p is the duration of the radiation pulse (Fig. 3, curve *1*). The parameter ν_0 can be found by the method given in [12] (see Fig. 4). At $\nu_0 t_p = 4$ the decline curve of the delayed component of the RPEC is transformed into a straight line, at $\nu_0 t_p < 4$ the curve is convex in the sense that the slope of the curve decreases when approaching the end of the pulse from the high time side as in curve *5* in Fig. 4. At $\nu_0 t_p > 4$, the decline curves become convex as in curves *1*–*3* in Fig. 4. Curve *3* ($\nu_0 = 6.5 \times 10^5$ c^{-1}) allows us to determine the value of this parameter for LDPE at 298 K (Table 2).

After that, it is necessary to determine the experimental value of the delayed component reduced to the unit of dose rate at the moment of pulse termination (K_{d1}) and the dimensionless ratio $\delta_{d1} = K_{d1} / K_p$, equal to 0.28 for curve *1* in Fig. 1. Further, for the found values of α and ν_0 we determine the parameter δ_{d2} by the value of the delayed component of the RPEC at the moment of pulse termination, expressed in units of the instantaneous component of the RFW model $K'_p = \eta_0\mu_0\tau_0 e$ [4, 8], using the MathCad program, as in [11, 12]. In the calculations, it was assumed that both μ_0, and $\overline{\mu_0}$ are equal to 10^{-5} m^2/B · s, and τ_0 and $\overline{\tau_0}$ are chosen so that the product of $\mu_0\tau_0$

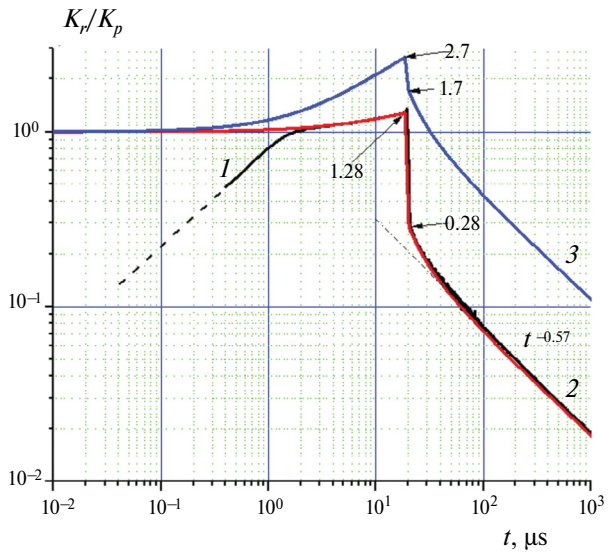

Fig. 3. Experimental (*1*, black, on the ordinate axis the ratio K_r / K_p) and numerically obtained (*2*, on the ordinate axis the ratio K_r / K'_p) RPEC curves of LDPE at 298 K, dose rate 6.2×10^5 Gy/sec. Curve *2* almost coincides with curve *1*, which drops sharply to zero at $t \leq 0.4$ μs (shown in dashed line) due to the influence of methodological factors (measurement time constant, inertia of the electronic system, etc.). The electron pulse duration is 20 μs. The calculated curve (*3*, blue) is calculated for the parameter $\overline{\mu_0\tau_0} = 1.9\times10^{-16}$ m^2/V (Table 2)

retains the required value. Thus, the value of K_{d1} for LDPE at 298 K is 0.28 K_p (curve *1* in Fig. 3), i.e. $\delta_{d1} = 0.28$, and $K_{d2} = 1.7K'_p$ (curve *3* in the same figure) i.e. $\delta_{d2} = 1.7$. In determining k, we proceed from the original relation $K_{d1} = K_p\delta_{d1} = K'_p\delta_{d2}$ and find that $\overline{\mu_0\tau_0}\delta_{d1} = \mu_0\tau_0\delta_{d2} = k\,\overline{\mu_0\tau_0}\,\delta_{d2}$. Here each term of the equality is reduced by the common multiplier $\eta_0 e$. Hence we find that $k = \delta_{d1} / \delta_{d2} = 0.28 / 1.7 = 0.165$ (Table 2). The control calculation by the RFW model fully confirmed the correctness of the calculation of the coefficient k.

Table 2. Values $\mu_0\tau_0$ calculated using the described methodology with the necessary parameter values for calculation

Polymer / temperature		$K_p \cdot 10^{15}$, F / (m · Gr)	$\nu_0 \cdot 10^{-3}$, c^{-1}	α	δ_{d1}	δ_{d2}	k	$\overline{\mu_0\tau_0} \cdot 10^{16}$, m^2/B	$\mu_0\tau_0 \cdot 10^{16}$, m^2/B
LDPE	298 K	5.5	600	0.43	0.28	1.7	0.165	1.9	0.31
	103 K	3.5	4	0.12	0.024	0.24	0.1	1.2	0.12
PP	298 K	5.6	20	0.38	0.1	2	0.05	2.0	0.1
	298 K	5.6	4	0.38	0.07	0.7	0.1	2.0	0.2
	103 K	4.7	0.17	0.17	0.024	0.024	1.0	1.7	1.7

Note. The density of LDPE and PP is 0.95 and 0.92 g / cm^3, respectively. The first line for PP at 298 K corresponds to curve 2 and the second line corresponds to curve 3 in Fig. 5

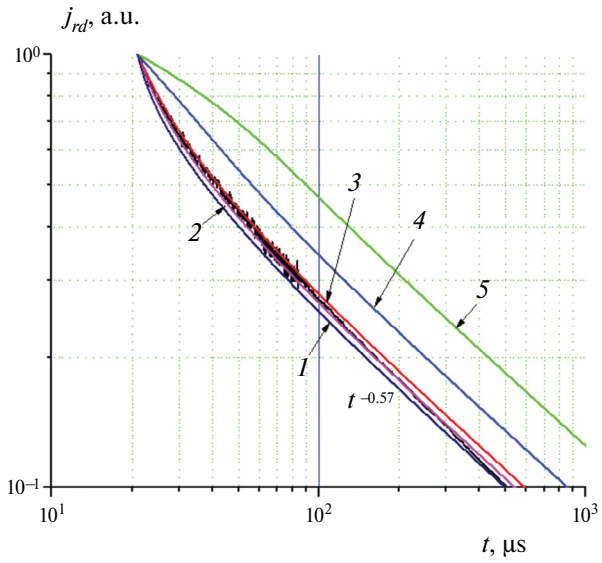

Fig. 4. Experimental (black) and calculated curves (*1*–*5*) demonstrating the method of frequency factor selection on the example of LDPE (normalized to the value of j_{rd} at the moment of radiation pulse termination). The temperature is room temperature, the pulse duration is 20 μs. The frequency factor values are 10^7 (*1*), $10^{(6)}$ (*2*), 6×10^5 (*3*), 2×10^5 (*4*), and 8×10^4 s^{-1} (*5*)

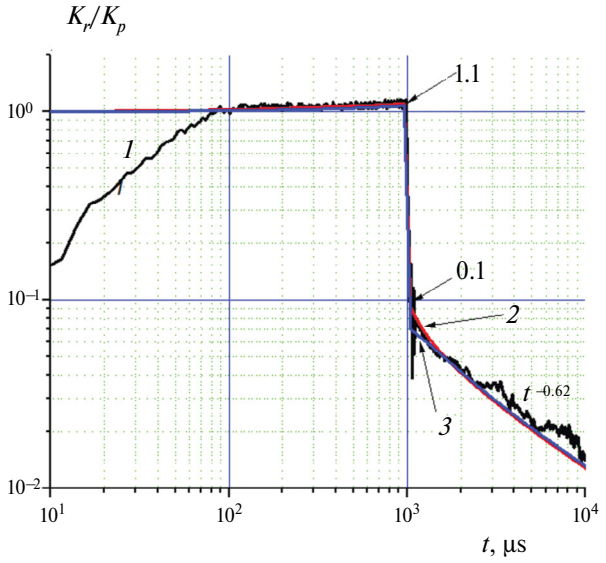

Fig. 5. Experimental (*1*) and numerically calculated (*2*, *3*) RPEC curves of PP at 298 K, dose rate 1.7×10^4 Gy/s. For curve *2* the parameter $\delta_{d1} = 0.1$, for curve *3* it is equal to $\delta_{d1} = 0.07$ (shown by arrows)

The table shows the values of $\mu_0\tau_0$, for LDPE and PP at 103 K (for PP and at 298 K), calculated by the above described method with the necessary data for calculation. Let us point out one peculiarity of the above methodology. Fig. 5 shows that the course of the delayed component decline curve allows ambiguity of interpretation at the earliest stage after the end of the pulse. The data of Table 2 refer precisely to the type of the decline curve adopted in the figures (highlighted in red). In the approach used for curve *3* in Fig. 5, the parameter $\delta_{d1} = K_{d1} / K_p$ will decrease to 0.07 at $\nu_0 = 4\times10^3$ s^{-1} (the decline curve is a straight line up to the end of the $t_{p\ pulse}$), so that $\mu_0\tau_0$ appears to be $0.2\times10^{-16}m^2/V$ ($k = 0.1$), which is two times the original value. This result emphasizes the importance of determining the exact course of the decay curve of the delayed RPEC component immediately after the end of the radiation pulse.

Table 2 also shows that in PP the parameter $\overline{\mu_0}\,\overline{\tau_0}$ practically does not change at transition from room temperature to 103 K and is within the experimental error± 20%.

One more peculiarity should be noted: *k* in PP increases with decreasing temperature and approaches unity. In LDPE the opposite effect is observed – the coefficient k, when passing from room temperature to 103 K, decreased. This issue requires serious study and interpretation in the future.

The model used in this work can be applied to analyze the photogeneration of current carriers in organic solar cells at low temperature [17, 18]. Also, this model of an effective homogeneous medium can be applied to study the properties of modern composite materials [19, 20], which are of interest for various fields of science and technology.

3. CONCLUSION

The technique we have described allows us to estimate the parameter $\mu_0\tau_0$ directly from the experiment. Thus, all parameters of the RFW model are estimable from experimental data, although this procedure relies on obtaining accurate data on the decay of the delayed component immediately after the end of the radiation pulse, as demonstrated in Fig. 3 curve *1*, which is not always possible in a real experiment. The modified dispersive transport model can be called a two-parameter model, distinguishing between shifts of carriers in a unit electric field before the first trapping ($\overline{\mu_0\tau_0}$) and those moving by recapture across traps ($\mu_0\tau_0$). These parameters were determined experimentally for both polymers (see Table 2). Thus, the fundamental difficulty in explaining such a significant drop in the RPEC (up to a factor of ten, as observed in LDPE and PP at 103 K) immediately after the end of the radiation

pulse has been eliminated. In [11], this phenomenon was erroneously explained by the influence of hemin recombination.

In the future it is necessary to elucidate the issue related to the temperature dependence of $\mu_0\tau_0$ to explain the different temperature dependence of the shift of thermalized charge carriers in a unit electric field.

ACKNOWLEDGEMENTS

The authors are grateful to D. N. Sadovnichiy for providing the data of Monte Carlo calculations used in Table 1.

FUNDING

The authors are grateful to the Fundamental Research Program of National Research University Higher School of Economics for its support.

ETHICS DECLARATION

There are no human or animal studies in this paper.

CONFLICT OF INTEREST

The authors of this paper declare that they have no conflicts of interest.

REFERENCES

1. *Tyutnev A. P., Saenko V. S., Pozhidaev E. D., Kostyukov N. S.* Dielectric Properties of Polymers in the Fields of Ionizing Radiation. Moscow: Nauka, 2005.
2. *Tyutnev A. P., Abramov V. N., Dubenskov P. I., Vannikov A. V., Saenko V. S., Pozhidaev E. D.* // Dokl. of the USSR Academy of Sciences. 1986. Vol. 289. No. 6. P. 1437.
3. *Tyutnev A. P., Sadovnichiy D. N., Saenko V. S., Pozhidaev, E. D.* // High-molecular compounds. A. 2005. Vol. 47. № . 11. P. 1971.
4. *Tyutnev A., Saenko V., Ikhsanov R., Krouk* E. // J. Phys. Appl. Phys. 2019. Vol. 126. 095501; https://doi.org/10.1063/1.5109768.
5. *Tyutnev A. P., Ihsanov R. Sh., Saenko V. S., Pozhidaev E. D.* // High-molecular compounds. A. 2006. Vol. 48. No. 11. P. 2015.
6. *Tyutnev A. P., Saenko V., Mullakhmetov I., Abrameshin A.* // J. Appl. Phys. Appl. Phys. 2021. Vol. 129. 175107; https://doi.org/10.1063/5.0048649.
7. *Mullakhmetov I. R., Tyutnev A. P., Saenko V. S., Pozhidaev E. D.* // Zhurn. tekhn. phys. 2023. Vol. 93. No. 1. P. 130; https://doi.org/10.31857/10.21883/JTF.2023.01.54072.207–22.
8. *Tyutnev A. P., Saenko V., Mullakhmetov I., Abrameshin A.* // J. Appl. Phys. Appl. Phys. 2022. Vol. 132. 135105; https://doi.org/10.1063/5.0106159.
9. *Tyutnev A. P., Saenko V., Mullakhmetov I., Pozhidaev E.* // J. Appl. Phys. Appl. Phys. 2023. Vol. 134. 095903; https://doi.org/10.1063/5.0158855.
10. *Goldansky V. I., Trakhtenberg L. I., Flerov V.* N. Tunnel phenomena in chemical physics. Moscow: Nauka, 1986.
11. *Tyutnev A. P., Saenko V. S., Pozhidaev E. D.* // Chemical Physics. 2006. Vol. 25. No. 1. P. 79.
12. *Tyutnev A. P., Saenko V. S., Pozhidaev E. D.* // IEEE Trans. Plasma Sci. 2018. Vol. 46. P. 645; https://doi.org/10.31857/10.1109/TPS.2017.2778189.
13. *Tyutnev A. P., Sadovnichiy D. N., Saenko V. S., Pozhidaev, E. D.* // High-molecular compounds. A. 2000. Vol. 42, № . 1. P. 16.
14. *Bartenev G. M., Barteneva A. G.* Relaxation properties of polymers. M: Khimiya, 1992.
15. *Nikitenko V. R.* Non-stationary processes of charge carriers transfer and recombination in thin layers of organic materials. M.: NIAU MIFI, 2011.
16. *Khan M. D., Nikitenko V. R., Tyutnev A. P., Ikhsanov R. Sh.* // J. Phys. Phys. Chem. C. 2019. Vol. 123. Pp. 1652–1659; https://doi.org/10.1021/acs.jpcc.8b11520.
17. *Lukin L. V.* // Chem. physica. 2023. Vol. 42. No. 12. P. 54; https://doi.org/10.31857/10.31857/S0207401X23120075.
18. *Lukin L. V.* // Chem. physics. 2024. Vol. 44. No. 12.
19. *Gerasimov G. N., Gromov V. F., Ikim M. I., et al.* // Chem. physics. 2021. Vol. 40. No. 11. P. 65; https://doi.org/10.31857/S0207401X21110030.
20. *Simbirtseva G. V., Babenko S. D.* // Chemical Physics. 2023. Vol. 42. No. 12.P. 64; https://doi.org/10.31857/10.31857/S0207401X23120117.

ADVANCES IN CHEMICAL PHYSICS, 2025, Vol. 44, No. 1, pp. 73–77

ELECTRICAL AND MAGNETIC PROPERTIES OF MATERIALS

DIELECTRIC CHARACTERISTICS OF POLYVINYL ALCOHOL FILMS

© 2025 G. V. Simbirtseva*, S. D. Babenko

Semenov Federal Research Center for Chemical Physics, Russian Academy of Sciences, Moscow, Russia

**e-mail: sgvural@mail.ru*

Received March 14, 2024

Revised April 08, 2024

Accepted April 22, 2024

Abstract. Dielectric characteristics of polyvinyl alcohol films obtained from aqueous solutions of the polymer have been investigated. The results of low-frequency (25 Hz – 1 MHz) and high-frequency (9.8 GHz) measurements are presented. The influence of filtration of aqueous solution of polyvinyl alcohol on dielectric parameters of the studied samples was found. The IR spectra of both types of films are identical and correspond to the literature data.

Keywords: *complex dielectric permittivity, electrical conductivity, IR spectroscopy, polyvinyl alcohol*

DOI: 10.31857/S0207401X250109e1

1. INTRODUCTION

One of the promising directions in the search for new functional materials with different properties is the production of composite materials based on polymer matrix. The choice of polyvinyl alcohol (PVA) as the main polymer for various types of nanofillers is promoted by its biocompatibility, nontoxicity, biodegradability, film-forming ability, hydrophilicity, water solubility, chemical resistance, availability and ease of processing [1, 2]. The large number of hydroxyl groups in PVA prevents agglomeration with nanofillers and promotes their uniform dispersion in its matrix, and hence improves the properties of nanocomposites [2]. Due to such properties, PVA is chosen as a base matrix for fillers in various applications [1, 3–6].

The reduction and elimination of electromagnetic radiation (EMI) pollution and new wireless telecommunication standards require a variety of affordable, lightweight, EMI shielding and radio-absorbing composite materials. Carbon nanoscale structures used as fillers in polymer composites allow the development of new approaches to create new materials with different properties and therefore different practical applications while reducing the amount of fillers and reducing the weight of composite materials. The combination of the above-mentioned properties of polyvinyl alcohol and carbon nanoscale structures allows us to consider composites based on them as promising materials absorbing EMI.

The present work is devoted to the study of electrophysical properties of PVA polymer films for their possible use as a basis for composite materials containing carbon nanoscale structures.

2. EXPERIMENT

Commercial polyvinyl alcohol grade 098–15(G) (Sinopec, China) with a mass fraction of the main substance $(CH_2CHOH)_n$ of at least 95.3%, density of 1.19–1.31 g/cm^3, melting point of 220–230 °C, degree of hydrolysis of 98.6%, and decomposition temperature of 160–200 °C without prior purification was used as a polymer material for film preparation. To obtain a **1-nF** film sample, 6 g of PVA was dissolved in 95 mL of water at 80–93 °C for several days. Then 6 g of the solution was placed in a 2.4*7.1 cm^2 Teflon container and dried for 1 day at (2–3)*10^{-2} mmHg pressure and room temperature. Then, the aqueous solution of PVA was filtered with No. 2 filter paper to free the insoluble part. The **2-F** film sample was made similarly from 10 mL of the resulting filtered solution. Freshly prepared films were used in the experimental measurements. The films were

0.025 (**1-nF**) and 0.013 (**2-F**) cm thick with respective densities of 0.95 and 0.55 g/cm^3.

The IR spectra of PVA films were recorded on a FT-02 FT-IR spectrometer (Lumex, Russia) in the wave number region 450–3500 cm^{-1} with a resolution of 4 cm^{-1}. In low-frequency measurements, the capacitance C and resistance R of PVA films were determined in a two-electrode system with a diameter of brass electrodes of 5 mm at a pressure of 2 MPa in the frequency range of 25 Hz-1 MHz using an E7–20 immittance meter (Russia). To correctly determine the values of dielectric permittivity and low-frequency conductivity (σ_{LF}), which depend on the sample inhomogeneity, these measurements were carried out in different parts of the sample and these values were averaged. The complex dielectric permittivity of the samples (CDP) at high frequency (9.8 GHz) was measured by the resonator method, for this purpose the samples were placed in glass ampoules with an inner diameter of 2–2.5 mm. The obtained values of dielectric permittivity (ε'), dielectric loss (ε ") and tangent angle of dielectric loss (tanδ) were averaged over several measurements. All measurements were performed at room temperature, and their accuracy was 10 and 20% for ε' and ε", respectively. The above methods are described in [7–10].

3. DISCUSSION OF RESULTS

The frequency dependence of dielectric characteristics of materials is described by the complex dielectric permittivity $\varepsilon(\omega) = \varepsilon'(\omega) - j\varepsilon''(\omega)$, where $\omega = 2\pi f$, f is the frequency of the applied electromagnetic field, ε'(ω) and ε"(ω) are the real and imaginary parts of the CDP characterizing dielectric polarization and losses in the dielectric, with dielectric loss angle tangent $\tan\delta = \varepsilon''/\varepsilon'$. The measured values of capacitance C and the tanδ dielectric loss angle tangent were used to calculate the low-frequency dielectric parameters. The values of ε' were determined as $\varepsilon' = Cd/S\varepsilon_0$, where d is the thickness of the sample, m, S is the area of the electrode, m^2, $\varepsilon_0 = 8.85*10^{-12}$ F/m is the dielectric constant of free space. The values ε" were calculated by the relation $\varepsilon'' = \varepsilon'\tan\delta$. In case of high-frequency measurements tgδ was determined from the measured values ε' and ε". The low-frequency and high-frequency conductivities (σ_{LF} and σ_{HF}) were calculated by the ratio $\sigma = \varepsilon_0 w\varepsilon''$.

Taking into account the technological process of PVA production, in which polyvinyl acetate (PVAc) is the main material, it is possible to analyze the experimental results, considering the produced PVA films as a system of PVA+PVAc+water, each component of which can contribute to their dielectric characteristics. Since polyvinyl alcohol is a hygroscopic polymer with OH-group, its properties can be influenced by many factors such as the method of its preparation, molecular weight distribution, branching, degree of hydrolysis, presence of residual acetate groups, and water [11–16]. These factors can lead to structural inhomogeneities of the films.

The measured IR spectra of PVA films (Fig. 1) contain characteristic absorption bands attributed to stretching vibrations of C-O bonds at 1050–1140 cm^{-1} [17], C-H/CH_2 at 2880–2960 cm^{-1} [1, 4, 17–19] and O-H at 3100–3500 cm^{-1} [1, 4, 17–20], and to bending vibrations of O-H bonds at 510–740 cm^{-1} [18] and CH_2 at 1320–1470 cm^{-1} [19]. Absorptions at 850 cm^{-1} and 918 cm^{-1} are attributed to vibrations of the carbon framework of PVA [4, 17]. At 1235 cm^{-1}, a weak absorption corresponding to C-H bond vibrations is observed [4, 17], and the absorption at 1660 cm^{-1} is attributed to C=O stretching vibrations of the carbonyl group of PVA [4].

The measured low-frequency parameters of the PVA films are presented in Fig. 2. For specificity, Table 1 summarizes these values for both films at frequencies of 60 Hz, 10 kHz and 1 MHz.

Table 1. Low-frequency electrophysical characteristics of polyvinyl alcohol films

Sample	f, Hz	ε'	ε"	tanδ	σ_{LF}, S/m
1-nF	60	4,99	0,35	0,07	$1{,}33*10^{-9}$
	10^4	4,15	0,22	0,05	$1{,}16*10^{-7}$
	10^6	3,40	0,28	0,08	$1{,}50*10^{-5}$
2-F	60	3,09	0,17	0,06	$7{,}11*10^{-10}$
	10^4	2,67	0,12	0,05	$6{,}67*10^{-8}$
	10^6	2,57	0,20	0,08	$1{,}08*10^{-5}$

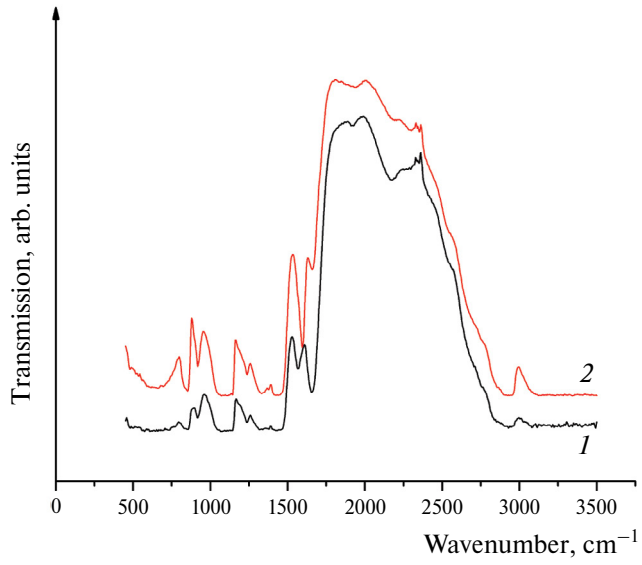

Fig. 1. IR spectra of films made from unfiltered **(1)** and filtered **(2)** aqueous solutions of polyvinyl alcohol. 1-film **1-nF**, 2-film **2-F**.

Table 2. High-frequency electrophysical characteristics of polyvinyl alcohol films at 9.8 GHz

Sample	ε'	ε''	tanδ	σ_{HF}, S/m
1-nF	2,97	1,62	0,52	0,89
2-F	2,97	2,09	0,75	1,16

The decrease of the low-frequency values of the real part of the dielectric constant ε' (Fig. 2a) and increase of σ_{LF} values (Fig. 2d) with frequency is typical for many polymers, and in the literature it is attributed mainly to dipole polarization [1, 21]. The behavior of ε'' seems to reflect the structural heterogeneity of the studied PVA polymer films and the uncontrolled water content.

Filtration of aqueous polyvinyl alcohol solution resulted in changes in the low-frequency and high-frequency CDP values of PVA films. The low-frequency values of ε', ε'', tanδ and σ_{LF} decreased while maintaining the trend of their frequency dependence (Fig. 2, Table 1). It can be assumed

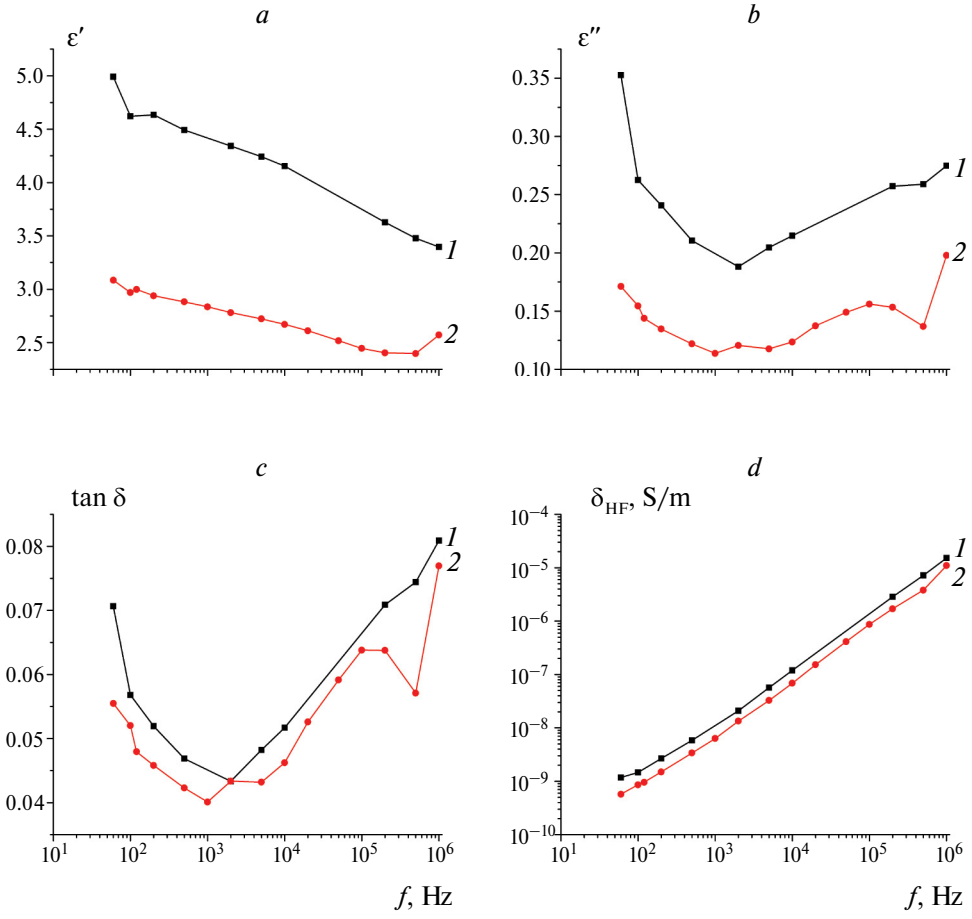

Fig. 2. Effect of filtration of aqueous polyvinyl alcohol solution on the low-frequency complex dielectric permittivities and conductivities (ε' (a), ε'' (b), tanδ (c), σ_{LF} (d)) of **1-nF** (1) and **2F** (2) PVA films

that the **2-F** sample obtained from the filtered PVA solution is more homogeneous in composition than the **1-nF** sample obtained from the original solution, it may have fewer uncontrolled impurities, which is reflected in the low-frequency characteristics. Table 2 summarizes the high-frequency dielectric characteristics. The increase in the high-frequency dielectric loss values of the PVA film prepared from filtered aqueous PVA solution can be attributed to the more porous structure of the **2-F** film, as indicated by its lower density. The decrease in density seems to be due to the increase in free volume [16], i.e., the air-bound water ratio has changed.

The low-frequency and high-frequency values of ε' and ε" presented in the present work, which exceed the similar values for PVA powder [14], indicate the role of water contained in the studied PVA films. Adsorbed water affects the dielectric and physical and mechanical properties of polymer composites [13, 15, 16, 21–23]. The low-temperature regime for obtaining the studied PVA films (<100 °C) promotes water retention due to its interaction with polymer molecules. Evaporation of free water occurs at temperatures up to 200 °C, and removal of chemically bound water occurs in the range 230–400 °C [19]. In the investigated films, the values of ε' (Fig. 2a) are much lower than those for free water [24] and this may be due to the influence of adsorbed water. The binding of water and PVA molecules in the aqueous solution, the subsequent attachment of water molecules to the groups of the polymer molecule of PVA may limit their motion and increase the relaxation time compared to free water molecules [14]. Comparison of the frequency characteristics of the dielectric permittivity of water in different states (solid, adsorbed, liquid) revealed a shift of the frequency dispersion of the dielectric permittivity to the region of lower frequencies and a significant increase in the dielectric relaxation time of adsorbed water compared to water in the liquid phase [24].

Dielectric characteristics of PVA films allow us to consider the possibility of their use as a basis for polymer composite materials containing carbon nanoscale fillers that absorb electromagnetic radiation [8, 10].

4. CONCLUSION

Low-frequency (25 Hz-1 MHz) and high-frequency (9.8 GHz) measurements of complex dielectric permittivity and electrical conductivity of polymer films of polyvinyl alcohol obtained from aqueous solutions of the polymer have been carried out. The influence of filtration of aqueous solution of polyvinyl alcohol on the electrophysical parameters of the films obtained from it was demonstrated. The influence of filtration on the IR spectra of the films was not found and they correspond to the literature data. Polyvinyl alcohol can be considered as a basis for polymer composite materials with carbon nanostructured fillers that absorb electromagnetic radiation.

REFERENCES

1. *Reddy P. L., Deshmukh K., Chidambaram K. et al.* // J. Mater. Mater. Sci. Mater. Electron. 2019. Vol. 30. P. 4676. https://doi.org/10.1007/s10854-019-00761-y
2. *Sahu G., Das M., Yadav M. et al.* // Polymers. 2020. Vol. 12. 374. https://doi.org/10.3390/polym12020374.
3. *Asriani A., Santoso I.* // JPSE (Journal of Physical Science and Engineering). 2021. Vol. 6. P. 10. https://doi.org/10.17977/um024v6i12021p010
4. *Rani P., Ahamed M. B., Deshmukh K.* // Mater. Res. Express. 2020. Vol. 7. 064008. https://doi.org/10.1088/2053–1591/ab9853
5. *Rapisarda M., Malfense Fierro G.-P., Meo M.* // Sci. Rep. 2021. Vol. 11. 10572. https://doi.org/10.1038/s41598-021-90101-0
6. *Kim M. P., Um D.-S., Shin Y.-E. et al.* // Nanoscale Res. Lett. 2021. Vol. 16. 35. https://doi.org/10.1186/s11671-021-03492-4.
7. *Vikulova M. A., Tsyganov A. R., Artyukhov D. I., et al.* // Chem. physics. 2023. T. 42. No. 11. P. 3. https://doi.org/10.31857/S0207401X23110092
8. *Simbirtseva G. V., Piven N. P., Babenko S. D.* // Chemical Physics. 2022. T. 41. No. 4. P. 32. https://doi.org/10.31857/S0207401X22040094
9. *Simbirtseva G. V., Babenko S. D., Perepelitsina E. O., et al.* // Journal of Physical Chemistry. 2023. Vol. 97. No. 1. P. 175. https://doi.org/10.31857/S0044453723010302
10. *Simbirtseva G. V., Babenko S. D.* // Chemical Physics. 2023. Vol. 42. No. 12. C. 64. https://doi.org 10.31857/S0207401X23120117
11. *Kharazmi A., Faraji N., Hussin R. M. et al.* // Beilstein J. Nanotechnol. 2015. Vol. 6. P. 529 https://doi.org/10.3762/bjnano.6.55

12. *Deshmukh K., BasheerAhamed M., Deshmukh R. R. et al.* // Eur. Polym. J. 2016. Vol. 76. P. 14. https://doi.org/10.1016/j.eurpolymj.2016.01.022
13. *El-Bashir S. M., Alwadai N. M., AlZayed N.* // J. Mol. Mol. Struct. 2018. Vol. 1154. P. 239. https://doi.org/10.1016/j.molstruc.2017.09.043
14. *Yeow Y. K., Abbas Z., Khalid K. et al.* // Am. J. Appl. Sci. 2010. Vol. 7. P. 270.
15. *Amin E. M., Karmakar N., Winther-Jensen B.* // Progr. Electromag. Res. B. 2013. Vol. 54. P. 149.
16. *Cobos M., Fernández M. J., Fernández D.* // Nanomaterials. 2018. Vol. 8. 1013. https://doi.org/10.3390/nano8121013
17. *Reddy P. L., Deshmukh K., Kovářík T. et al.* // Mater. Res. Express. 2020. Vol. 7. 064007. https://doi.org/10.1088/2053–1591/ab955f
18. *Allayarov S. R., Korchagin D. V., Allayarova U. Yu. et al.* // High Energy Chemistry. 2021. Vol. 55. No. 1. C. 42. https://doi.org/10.31857/S0023119321010022
19. *Gil-Castell O., Cerveró R., Teruel-Juanes R. et al.* // J Renew. Mater. 2019. Vol. 7. No. 7. P. 655. https://doi.org/10.32604/jrm.2019.04401
20. *Pan X., Debije M. G., Schenning A. P. H. J. et al.* // ACS Appl. Mater. Interfaces. 2021. Vol. 13. P. 28864. https://doi.org/10.1021/acsami.1c06415
21. *Kandhol G., Wadhwa H., Chand S. et al.* // Vacuum. 2019. Vol. 160. P. 384. https://doi.org/10.1016/j.vacuum.2018.11.051
22. *Morozov E. V., Ilyichev A. V., Buznik V. M.* // Chemical Physics. 2023. Vol. 42. No. 11. P. 54. https://doi.org/10.31857/S0207401X23110067
23. *Podzorova M. V., Tertyshnaya Y. V., Khramkova A. V.* // Chemical Physics. 2023. T. 42. No. 1. P. 35. https://doi.org/10.31857/S0207401X23010090
24. *Simakov I. G., Gulgenov Ch. Zh., Bazarova S. B. // IOP Conf. B.* // IOP Conf. Series: Journal of Physics: Conf. Series. 2019. Vol. 1281. 012073. https://doi.org/10.1088/1742–6596/1281/1/012073

ADVANCES IN CHEMICAL PHYSICS, 2025, Vol. 44, No. 1, pp. 78–82

CHEMICAL PHYSICS OF NANOMATERIALS

STRUCTURE, CONDUCTIVITY AND SENSOR PROPERTIES OF NiO–In_2O_3 COMPOSITES SYNTHESIS BY DIFFERENT METHODS

© 2025 M. I. Ikim[a]*, A. R. Erofeeva[a], E. Y. Spiridonova[a], B. F. Gromov[a], G. N. Gerasimov[a], and L. I. Trakhtenberg[a, b]

[a] *Semenov Federal Research Center of Chemical Physics, Russian Academy of Sciences, Moscow, Russia*

[b] *Lomonosov Moscow State University, Moscow, Russia*

**e-mail: ikimmary1104@gmail.com*

Received November 03, 2023

Revised November 15, 2023

Accepted November 20, 2023

Abstract. The effect of the synthesis method of NiO–In_2O_3 composites on their structural, conductive and sensory characteristics when detecting hydrogen was studied. Impregnation of indium oxide nanoparticles with a nickel nitrate salt and a hydrothermal method with aqueous solutions of the corresponding salts were used. It has been shown that during the impregnation process, nickel oxide is formed in the form of amorphous nanoparticles on the surface of indium oxide, and during hydrothermal treatment, nickel ions are introduced into In_2O_3 structures. In impregnated composites, the particle size of indium oxide does not depend on the composition and is 60 nm, while in hydrothermal composites it decreases from 35 to 30 nm with increasing nickel content. With an increase in nickel content from 0 to 3 wt.% for both synthesis methods, the conductivity decreases, and the resistance for hydrothermal samples is an order of magnitude higher than for impregnated ones. The sensory response was almost twice as high.

Keywords: *composite, hydrothermal method, impregnation method, indium oxide, conductivity, sensory response, hydrogen*

DOI: 10.31857/S0207401X250110e7

1. INTRODUCTION

The continuous growth of toxic and explosive gas emissions into the atmosphere leads to the need to develop sensors for their detection. Semiconductor sensors are of interest due to their commercial availability, ease of fabrication, good stability and prospects for modernization. The n-type metal oxides In_2O_3, ZnO, SnO_2, CeO_2 have been widely used in gas detection systems (see, for example, [1–4]). In binary sensors, the use of In_2O_3 is associated with a high concentration of electrons in the conduction zone [5–8].

Indium oxide crystallizes in two polymorphic modifications: cubic and rhombohedral, the properties of which affect the conductive and sensory characteristics. The conductivity of the rhombohedral phase of indium oxide is 8–12 times higher and the sensory response 1.5–2 times higher than that of its cubic phase [6]. Addition of catalytically active oxide to indium oxide leads to increased sensitivity in detection of various gaseous substances [9]. Doping In_2O_3 with ions of different valence also improves selectivity and sensitivity in the detection of hazardous gases [4].

One of the most promising *p*-type semiconductors as an additive for gas sensors is nickel oxide due to its chemical and thermal stability and high catalytic activity. Such an additive helps to reduce the operating temperature and response/recovery time [10]. The doping of indium oxide with 5 mol% NiO contributes to increase in the sensory response compared to pure In_2O_3 for the detection of 200 ppm CH_4 at a relatively low operating temperature [11]. The incorporation of 2 mol% Ni into In_2O_3 leads to a 12-fold increase in the response to 10 ppm NO_2compared to pure In_2O_3, at an operating temperature of 200 °C [12]. In addition, the sensor showed a low detection limit of 5 ppb of nitric oxide.

In this work, the influence of the synthesis method on the structural characteristics, conductivity, and sensory properties of layers based on nanoscale NiO-In_2O_3 composites for hydrogen detection in a wide temperature range was investigated. The composites were prepared by impregnation of indium oxide nanopowder with nickel nitrate salt with its subsequent transformation into oxide and by hydrothermal method using nitrate aqueous solutions of nickel and indium.

2. EXPERIMENTAL PART

NiO-In_2O_3 composites containing 0 to 3 wt.% nickel oxide were synthesized by two methods: hydrothermal [13] and impregnation [14]. Commercial In_2O_3 powder (AnalaR grade, 99.5%, BDH/Merck Ltd., Lutterworth, Leicestershire, UK) and chemically pure (CP) nickel nitrate $Ni(NO_3)_2 \cdot 6H_2O$ (GOST 5106–77) were used to obtain impregnated composites. Indium oxide powder was placed in an aqueous solution of nickel nitrate and incubated at room temperature for 24–48 hours. Further removal of water was carried out at a temperature of about 70–80 °C, then heated the samples for several hours to 500 °C to obtain impregnated composites.

Indium nitrate $In(NO_3)_3 \cdot 4H2O$ ($\geqslant$99.5%) and nickel nitrate $Ni(NO_3)_2 \cdot 6H_2O$ ($\geqslant$99%) were used as precursors for hydrothermal synthesis. To obtain indium oxide, 2 mmol of indium nitrate and 18 mmol of urea were dissolved in 80 mL of distilled water. To form the composites, the required amounts of nickel nitrate were added to the above composition. The synthesized solutions were incubated in an ultrasonic bath for 1 hour at 30 °C. Then they were placed in a 100 mL Teflon-coated autoclave for hydrothermal treatment for 3 hours at 160 °C. The resulting hydroxides were separated by centrifugation for 5 min at 4500 rpm and then washed with distilled water and annealed in air at 500 °C.

The phase composition, structure and morphology of the obtained composites were studied by X-ray diffraction (XRD) on a Rigaku Smartlab SE diffractometer using Cu($K\alpha$)-radiation with a wavelength of 1.5406 Å and transmission electron microscopy (TEM) on a Tecnai Osiris FEI instrument equipped with an energy dispersive analysis system.

To determine the conductivity and sensory properties, the synthesized composites were mixed with distilled water, and the resulting paste was applied to a special chip equipped with a heater and contacts. Further, the temperature was gradually increased up to 550 °C until a constant resistance of the obtained film was achieved.

The sensor response to H_2 was investigated using the developed setup in the temperature range from 300 to 550 °C. The chip with the applied sensing layer was placed in a special chamber with a volume of about 1 cm^3, into which purified air or a gas mixture containing 0.9% H_2 was supplied. The pumping rate of gases through the chamber was 200 ml/min, and the accuracy of temperature maintenance was within 1 °C. The response was defined as $S = R_0/R_g$, where R_0 is the initial sensor resistance (before the analyzed mixture was introduced) and R_g is the minimum value of the sensor resistance after the analyzed gas was introduced. The change in sensor resistance was recorded using a Keysight digital multimeter, the signal from which was transmitted to a computer.

3. DISCUSSION OF RESULTS

The data of X-ray phase analysis showed that regardless of the synthesis technique, when adding different concentrations of NiO to the composite, only peaks corresponding to the cubic phase of indium oxide with preferential orientation (222) are registered. The absence of nickel or its compounds may be due to the dissolution of nickel ions in the In_2O_3 lattice, the formation of an X-ray amorphous phase, or a small amount of Ni O.

With increasing nickel content in composites synthesized by the hydrothermal method, there is a shift of the diffraction angle towards higher values, while in impregnated composites the shift of peaks is insignificant. The ionic radius of Ni^{2+} is 0.75 Å, which is smaller than this value for In^{3+} – 0.81 Å. Consequently, the introduction of nickel ions into the In_2O_3 crystal lattice leads to a shift of the diffraction peaks of indium oxide towards larger angles.

As NiO is introduced into the composites obtained by the hydrothermal method, the lattice parameter decreases due to the difference in ionic radii, while in impregnated samples the lattice parameter is practically independent of the nickel oxide content in the composite (Fig. 1a). That is it can be assumed that for hydrothermal samples nickel is embedded in the structure of indium oxide, and in impregnated samples X-ray amorphous nickel oxide is formed on the surface of In_2O_3.

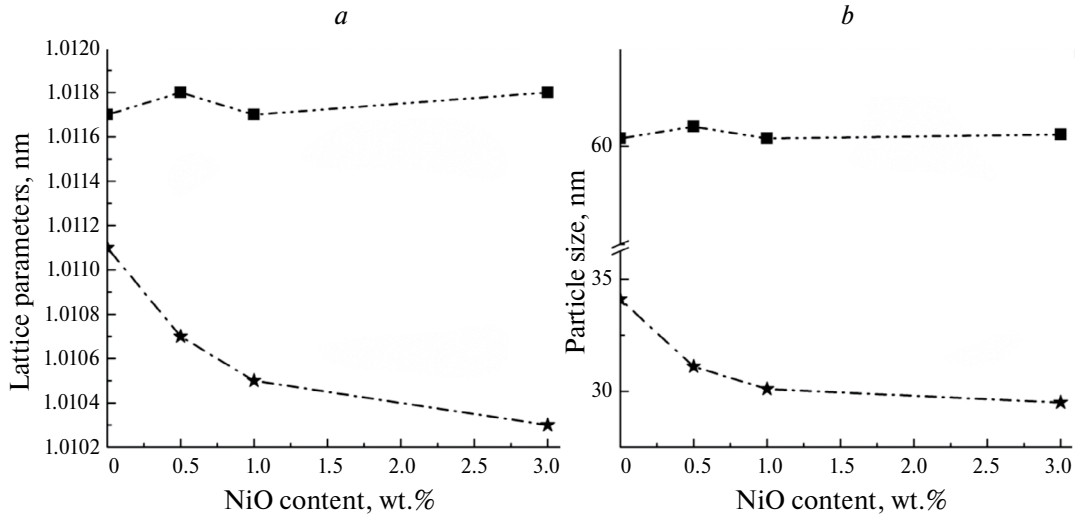

Fig. 1. Dependence of lattice parameter (*a*) and particle size (*b*) of In_2O_3 on NiO content in composites obtained by different methods

The particle sizes were calculated from X-ray phase analysis data, using the Debye-Scherrer equation by the peak width at its half-height and amounted to about 60 nm in the case of impregnated samples and 35–30 nm for composites obtained by the hydrothermal method (Fig. 1b). The increase in the concentration of nickel oxide in hydrothermal composites is accompanied by a decrease in the particle size from 35 to 30 nm, which is associated with the occurrence of deformation due to indium substitution in the crystal lattice. The introduction of nickel ions into the In_2O_3 structure prevents crystal growth. In the case of impregnated samples, unlike hydrothermal samples, the addition of nickel oxide does not significantly affect the particle size (Fig. 1b).

According to TEM data of impregnated NiO-In_2O_3 nanocomposites, spherical particles up to 20 nm are formed on the porous surface of indium oxide (particle size up to 100 nm) after impregnation with nickel nitrate and further heat treatment. In the case of hydrothermal samples, the particles have a cubic shape with a size of about 30 nm, which agrees with the XRD data. The results of energy dispersive analysis showed that in the hydrothermal composites, nickel ions are uniformly distributed in the indium oxide particles. While in impregnated composites, particles containing only nickel ions are observed on the surface of indium oxide. At the same time, some amount of nickel is distributed in the surface layer of indium oxide particles. The data of TEM, energy dispersive and X-ray diffraction analyses are in good agreement with each other.

For NiO-In_2O_3 composites obtained by impregnation and hydrothermal method, conductivity and sensory properties were investigated in the temperature range from 300 to 550 °C. Regardless of the synthesis method, an increase in conductivity with increasing temperature was observed, which is characteristic of *n-type* semiconductors. The dependence of resistance on nickel content for impregnated and hydrothermal composites is shown in Fig. 2a. It can be seen that the resistivity increases with increasing nickel content for both synthesis methods.

Since the electron yield work of NiO (5.5 eV) is larger than that of In_2O_3 (4.3 eV), electron transfer occurs from nanoparticles In_2O_3 to NiO nanoparticles, which leads to an increase in the resistance of composites due to a decrease in the concentration of electrons in the well-conducting indium oxide particles. During the hydrothermal synthesis process, nickel ions (Ni^{2+}) are introduced into the In_2O_3lattice, replacing In^{3+}) ions. Simultaneously, positively charged oxygen vacancies V^{+}_{O} are formed, which provides a balance of positive and negative charges during substitution. A similar process was observed during the formation of hydrothermal composites ZnO-In_2O_3 containing up to 20 wt.% of zinc oxide [15].

Note that the resistance of hydrothermal samples is an order of magnitude higher than impregnated composites. This may be due to the fact that the number of In^{3+} ions substituted by Ni^{2+} ions during hydrothermal synthesis of composites is greater than during impregnation, when the composite

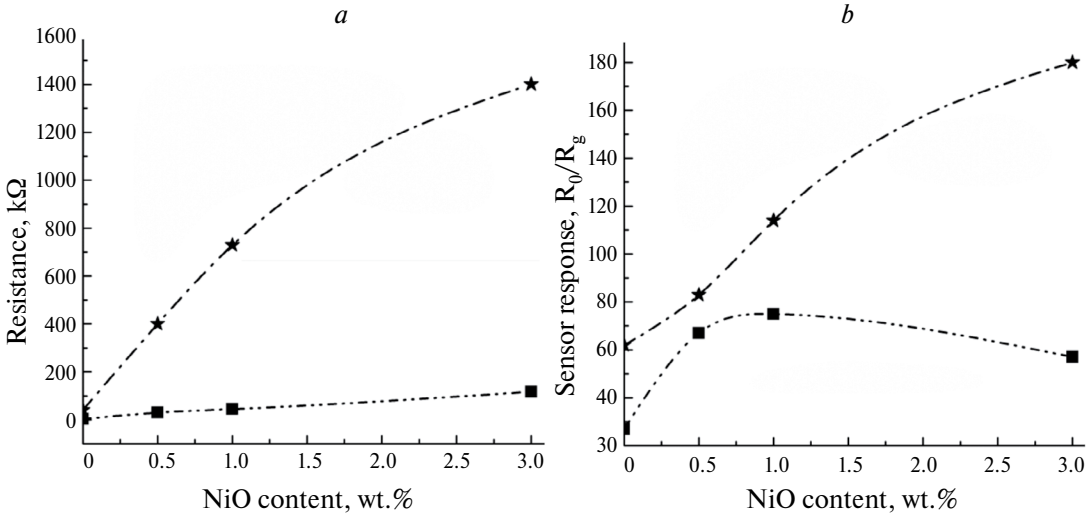

Fig. 2. Concentration dependence of resistance (*a*) and sensory response in detection of 0.9% H_2 (*b*) composites prepared by different methods

formation is concentrated mainly in the surface layers of nanocrystals.

In NiO – In_2O_3 composites, regardless of the method of their synthesis, the temperature dependence of the sensor response has a typical for semiconductor sensors curve with a maximum S_{max} at certain temperature T_{max}. Increasing the content of nickel oxide leads to a decrease in the operating temperature in hydrothermal samples by 60 °C, and in impregnated samples by 20 °C. This decrease may be due to the high catalytic activity of Ni O. For example, the operating temperature of composites obtained by solvothermal method was reduced by 60 °C in methane detection [16]. The sensory response of hydrothermal composites at hydrogen detection for all compositions is almost two times higher than that of the samples obtained by the impregnation method (Fig. 2b). The reason for this may be the small size of indium oxide nanoparticles, as the bond strength in their lattice is weakened, which leads to a significant decrease in the vacancy formation energy. The increase in the concentration of oxygen vacancies, which are the centers of chemisorption of oxygen and analyzed gas, contributes to the increase in the sensory activity of hydrothermal composites.

The method of synthesis of NiO-In_2O_3 composites significantly affects the character of change of their sensory response depending on the concentration of nickel oxide (Fig. 2b). For impregnated samples a maximum is observed at 1% NiO, further introduction of nickel oxide into the composite leads to a slight drop in the sensory response in contrast to hydrothermal composites where 3% NiO causes a sharp increase in sensory sensitivity. This is due to the interaction between the components: in hydrothermal composites, nickel ions are embedded in the lattice of indium oxide, while in composites synthesized by impregnation, nickel oxide nanoparticles are formed on the surface of In_2O_3 nanoparticles [17].

4. CONCLUSION

Studies of properties of NiO – In_2O_3 composites demonstrate a significant influence of the method of their synthesis on structural characteristics, conductivity and sensitivity at hydrogen detection. In the case of sample synthesis by impregnation method, X-ray amorphous NiO is formed on the surface of large indium oxide particles of the order of 60 nm. The formation of nickel oxide nanoparticles does not lead to a change in the structural characteristics and particle size of indium oxide. On the contrary, in hydrothermal samples nickel ions are uniformly distributed over the volume of In_2O_3 nanoparticles, the size of which decreases from 35 to 30 nm with increasing nickel concentration.

The conductivity of the samples, regardless of the method of synthesis, monotonically decreases with increasing concentration of nickel oxide in the composite. This change in the case of impregnated samples is associated with electron transfer between nanoparticles forming the composite, and in hydrothermal samples by modification of the electronic structure of In_2O_3. At the same time, the values of resistance and sensory response

to hydrogen of hydrothermal composites at all nickel concentrations are higher than those of impregnated ones.

The detailed study of the properties of NiO-In_2O_3 composites performed in this work indicates the essential role of the interaction between the metal-oxide components, which will allow further consideration of the mechanisms of such interaction in the sensing process.

FUNDING

The research was supported by the Russian Science Foundation grant No. 22–19–00037; https://rscf.ru/project/22–19–00037/.

REFERENCES

1. *Li Q., Zeng W., Li Y.* // Sens. Actuators B. 2022. Vol. 359. P. 131579.
2. *Zhang C., Xu K., Liu K., Xu J., Zheng Z.* // Coord. Chem. Rev. 2022. Vol. 472. P. 214758.
3. *Krishna K. G., Parne S., Pothukanuri N., Kathirvelu V., Gandi S., Joshi D.* // Sens. Actuators A. 2022. Vol. 341. P. 113578
4. *Trakhtenberg L. I., Ikim M. I., Ilegbusi O. J., Gromov V. F., Gerasimov G. N.* // Chemosens. 2023. Vol. 11(6). P. 320.
5. *Yan S., Song W., Wu D., Jin S., Dong S., Hao H., Gao W.* // J. *Alloys Compd*. Alloys Compd. 2022. Vol. 896. P. 162887.
6. *Ikim M. I., Spiridonova E. Yu., Gromov V. F., Gerasimov G. N., Trakhtenberg L. I.* // Chemical Physics. 2023. Vol. 42. No. 5. P. 71.
7. *Jimenez L. C., Mendez H. A., Paez B. A., Ramırez M. E., Rodrıguez H.* // Braz. J. Phys. 2006. Vol. 36. P. 1017.
8. *Prathap P., Gowri D. G., Subbaiah Y. P. V., Ramakrishna R. K. T., Ganesan V.* // Current Appl. Phys. Phys. 2008. Vol. 8. P. 120
9. *Gerasimov G. N., Gromov V. F., Ikim M. I., Trakhtenberg L. I.* // Chemical Physics. 2021. Vol. 40. No. 11. P. 65.
10. *Fan X., Xu Y., He, W.* // RSC advances. 2021. Vol. 11(19). P. 11215.
11. *Zhang Y., Cao J., Wang Y.* // Vacuum. 2022. Vol. 202. P. 111149.
12. *Jin Z., Wang C., Wu L., Song H., Yao X., Liu J., Wang F.* // Sens. Actuators B. 2023. Vol. 377. P. 133058.
13. *Ikim M. I., Spiridonova E. Yu., Gromov V. F., Gerasimov G. N., Trakhtenberg L. I.* // Chemical Physics. 2022. Vol. 41. No. 12. P. 79.
14. *Gromov V. F., Ikim M. I., Gerasimov G. N., Trakhtenberg L. I.* // Chemical Physics. 2021. Vol. 40. No. 12. P. 76.
15. *Ikim M. I., Spiridonova E. Yu., Gromov V. F., Gerasimov G. N., Trakhtenberg L. I.* // Russ. J. Phys. Chem. Vol. 18, 283 (2024).
16. *Wang Y., Yao M., Guan R., Zhang Z., Cao J.* // J. Alloys Compd. Alloys Compd. 2021. Vol. 854. P. 157169.
17. *Ikim M. I., Gromov V. F., Gerasimov G. N., Spiridonova E. Y., Erofeeva A. R., Kurmangaleev K. S., Polunin K. S., Ilegbusi O. J., Trakhtenberg L. I.* // Micromachines. 2023. Vol. 14(9). P. 1685.

ADVANCES IN CHEMICAL PHYSICS, 2025, Vol. 44, No. 1, pp. 83–93

REACTIONS ON SURFACE

INVESTIGATION OF INTERNAL STRUCTURE AND LOCAL ELASTIC PROPERTIES OF HUMAN HAIR WITH ATOMIC FORCE MICROSCOPY

© 2025 N. A. Erina*

Semenov Federal Research Center for Chemical Physics, Russian Academy of Sciences, Moscow, Russia

**e-mail: natalia.erina@mail.ru*

Received December 25, 2023

Revised January 18, 2024

Accepted January 22, 2024

Abstract. The detailed microstructure of human hair in the transverse and longitudinal directions was studied using of atomic force microscopy (AFM) in the mode of intermittent probe oscillation (known as TappingMode^{TM}). In addition, operating in AFM-based nanoindentation the local elastic properties (Young modulus, E_{loc}) were determined in various zones of the hair. For quantitative analysis of E_{loc} precise calibration of the AFM system and assessment of the tip apex geometry were carried out. To calculate the numbers of E_{loc} the adapted Sneddon contact mechanical model was used.

Keywords: *human hair, atomic force microscopy, nanoindentation, keratin, internal structure of hair in longitudinal and transversal sections, local Young modulus in longitudinal and transversal sections*

DOI: 10.31857/S0207401X250111e7

1. INTRODUCTION

Structurally, human hair is a complex hierarchical organization based on keratin – keratinized derivatives of epithelial cells of the skin. Keratins are a family of fibrillar proteins with high mechanical strength. Chemically, hair is composed of 65–95% α-aliphatic amino acids tyrosine, glycine and cysteine, 15–35% water, 1–9% lipids and less than 1% enzymes, pigments and cholesterol. The high content of sulfur-containing cysteine leads to the establishment of disulfide bonds between neighboring keratin chains, forming cysteine units. Along with disulfide bonds, the hair structure contains many peptide bonds containing numerous –CO and –NH groups that form hydrogen bonds between neighboring protein fibers. The resulting cross-linked keratin structure is responsible for the shape, structure and strength of the hair fibers [1]. It has been found that the chemical composition of hair can vary depending on the origin, sex, age and other conditions of the organism.

The hair consists of three morphological regions: the outer (cuticle), cortical (cortex), and core (medulla) (Fig. 1a). The cuticle is the outer protective sheath of the hair shaft, which is a keratinized nucleusless cells arranged in the form of scales forming a characteristic pattern and composed of a protein substance containing keratin and sulfur.

The structure of the cuticle is complex and is divided into several functional sub-layers: epicuticle, *A*-layer, exocuticle and endocuticle. Organic components of the cuticle (lipids, proteins and wax-like substances) provide hair with elasticity and natural shine. When the cuticle is damaged, its outer cells die and begin to peel off, and the hair surface loses its smoothness and healthy appearance [2].

The middle part of the hair (cortex) occupies up to 80% of the volume of the hair shaft and determines to the greatest extent the complex of its mechanical properties. The cortex is built of long, densely packed cells of different types (para- and ortho-) of spiral shape, connected by intercellular substance. The paracortical cells have a uniform shape and are only found in straight hair, while due to the orthocortical inhomogeneous cells, the hair is curly. Each cortex cell consists of bundles of keratin protofibrils, successively forming micro- and then macrofibrils oriented along the main axis of the hair [3]. In addition, it has been established that it is the cortex that contains the pigment melanin, which determines hair color [4].

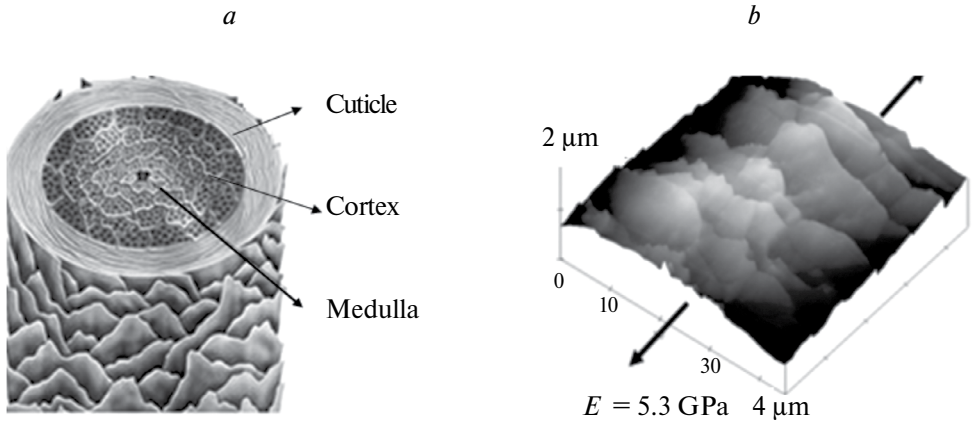

Fig. 1. *a* – Schematic image of the internal structure of the hair [saylordotorg.github.io]. *b* – Three-dimensional topographic image of the outer layer of the hair, obtained on a scanning probe microscope MultiMode™ (Bruker NanoSurface Inc., USA) in the oscillation mode (Tapping Mode™). The Young's modulus of the hair in uniaxial tension was determined on an Instron-3365 tensile testing machine (UK)

The innermost layer of the hair shaft (medulla) is a loosely packed channel of proteinaceous non-corneal cells in the central part of the hair, which may be continuous or fragmented. It has been suggested that the medulla is part of the excretory system of the hair and contains heavy metals and traces of drugs [2].

Hair consists of 80–90% keratin. The remaining substances are mainly water (for elasticity) and lipids (for protection). In essence, the hair shaft is different types of keratin assembled into differently shaped elements that are bound together by keratin-like cement [2]. As early as 1951, using X-ray and protein modeling experiments considering bond lengths and valence angles, it was shown that the fibrillar material of hair consists of spiral-shaped α-keratin fibers [5]. It has also been suggested that there is another form of keratin assembly in the form of folded plates of *β-keratin* that can be reversibly stretched to approximately 100% elongation (Fig. 2) [6]. Such an extremely complex structure provides high mechanical properties of the hair.

A large number of studies on natural wool fibers have been conducted to establish the relationship between the fine texture of the microfibril matrix and the macroscopic properties of the fiber. The molecular mechanism of microfibril deformation has been described as a gradual transition from α-helical tufts to β-layered structures [7]. Using this mechanism as the main mechanism, attempts have been made to explain the elastic response of keratin fibers in terms of its two structural subcomponents [8]. The value of the elastic modulus (Young's modulus) can vary from 2 to 8 GPa depending on the ethnicity, gender and age of the individual. The tensile strength ranges from 200 to 300 MPa, which is equivalent to that of lead, copper or platinum and comparable to that of steel [4, 9].

Currently, scanning probe microscopy (SPM) [10], which includes several methodological approaches, is widely used to obtain structural information of various materials: tunneling probe microscopy, which allows obtaining information on the topography and electrical characteristics of electrically conductive materials [11–14] and atomic force microscopy (AFM) [15].

AFM has made it possible to extend the scope of application of the SPM method to a wide range of materials by recording various forces of interatomic interaction between the probe and the sample surface. The basic principle of AFM is to record various forces of interaction (attraction or repulsion) between the probe located at the end of an elastic microcantilever (cantilever) and the surface of the sample [16]. Unlike the widely used electron and transmission electron microscopy, which require special techniques for surface preparation and contrasting of sample components, AFM is not an invasive methodology. In addition, AFM allows to simultaneously investigate topography, structural features and probe local physical and mechanical properties (elasticity, adhesion, electro-magnetic characteristics) of a wide range of materials with high spatial resolution [17].

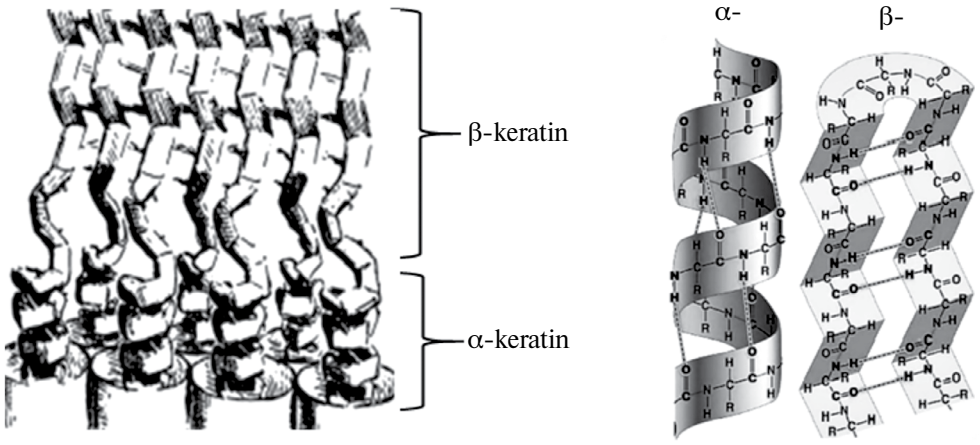

Fig. 2. Illustration of the packing of spiral-shaped ensembles of α-keratin that transform into folded plates of β-keratin when stretched

A key step in the development of AFM applications was the development of an oscillating mode (or intermittent contact) called TappingMode™ [18]. In this mode, the probe interacts with the sample surface for a very short period of time, which minimizes the influence of lateral friction forces during scanning and allows the examination of very soft samples without damaging their surface. At the beginning of the procedure, an elastic beam (cantilever) with a probe at the end is driven into free oscillation in the vertical direction at its resonant frequency and corresponding amplitude by means of a piezo element. The damping of the amplitude due to the resulting attraction forces between the probe and the sample is the mechanism for generating the surface topography. At the same time, a so-called phase image is mapped, the contrast change on which is caused by the shift of the phase angle of oscillations when the probe interacts with material regions having different mechanical properties. As a rule, a brighter contrast on the phase image corresponds to the most rigid and less dissipative regions of the material. However, one cannot quantitatively extract any specific mechanical characteristic of the material from the phase contrast, since the phase shift of the cantilever oscillations is due to the convolution of elastic, adhesive, and dissipative contributions at the moment of probe-sample contact [19].

Indentation [20] has become a theoretically and experimentally confirmed method for quantitative determination of local physical and mechanical properties of materials, including the application of the AFM methodology called nanoindentation [21]. This method of testing materials is based on indentation of the indenter into the specimen and recording, so-called force curves (FC), representing the dependence of the indentation depth (H) on the applied load (F) (Fig. 3).

The loading curve reflects the work expended to overcome the resistance of the material, determined by its stiffness (hardness) when the indenter is pushed in. The reverse process of unloading is the work expended to restore the material. In many cases, deformation occurs with the development of plasticity, when the recovery is not elastic, but with a delay due to the presence of structural elements of different viscosity in the material. This leads to energy loss (dissipation) during the unloading cycle and is manifested on the SC as the difference between

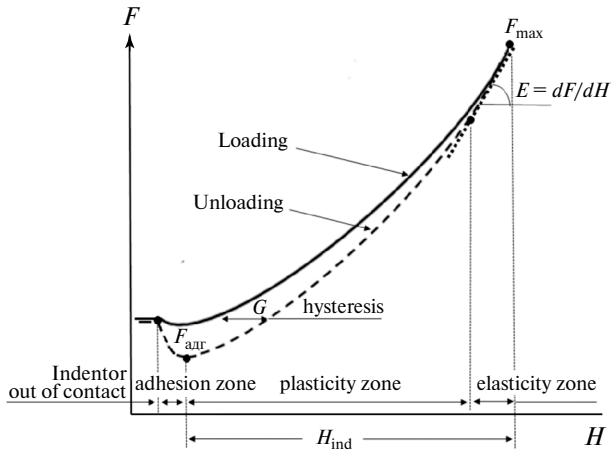

Fig. 3. Conditional force curve obtained by nanoindentation method

the loading and unloading curves, or hysteresis. Therefore, to calculate the modulus of elasticity (E), only the upper straight section of the unloading curve is analyzed by the tangent of its slope, where the material responds elastically in response to the applied force (F_{max}) and the influence of adhesion forces is minimal and hysteresis is not yet manifested.

At the same time, an adequate interpretation of AFM data and their subsequent use for characterizing local mechanical properties of materials requires a good understanding of the effects of probe-sample interactions. There are many contact models for determining the hardness and elasticity of materials during an indentation. One popular approach in this area is based on the Sneddon solution, which relates load to strain and the generated contact area to determine the shape coefficients of various axisymmetric indenters (cylinder, cone, ball, and paraboloid of rotation) [21].

Nanoindentation has been used to perform studies regarding structural mapping and probing of elastic and plastic properties of hair, however, mainly at the qualitative level [22–25]. However, for quantitative extraction of the mechanical characteristics of the material, it is necessary to perform an accurate calibration of the AFM system parameters, determine the stiffness of the cantilever and rationally select and digitize the probe shape.

The purpose of this study is to demonstrate the capabilities of AFM in the study of topography, microstructure and measurement of quantitative local elastic properties (Young's modulus) of human hair in transverse and longitudinal directions with accurate calibration of the AFM system. The variety of mechanical actions on the probe side gives a wide choice for hardware realization.

2. EXPERIMENT

Before the study, a sample of Caucasian human hair (purchased from https://haircenters.ru) was thoroughly washed in deionized water and dried at room temperature. After that, the hair fragments were impregnated in epoxy resin and after its curing were dissected transversely and longitudinally with a diamond knife at room temperature using a MicroStar 01 microtome (Microstar Technology, USA).

AFM studies were performed at room temperature using a MultiMode^{TM} atomic force microscope and a Nanoscope IIIA^{TM} controller from Bruker NanoSurface Inc. (USA). Before the nanoindentation procedure in order to select the most morphologically informative site, structural studies of the samples in the Tapping Mode^{TM} were performed.

To probe the local elastic properties of the material using the nanoindentation method, force curves (FC) were generated to record the forces of attraction and repulsion between the indenter and the surface of the investigated sample (Fig. 3). The modulus of elasticity (Young's modulus) E_{loc} was determined by the slope of the tangent to the initial linear section of the unloading curve.

In order to measure E_{loc} on a quantitative level, a complete calibration of the system was carried out. The stiffness of cantilevers was determined through the procedure of thermal excitation of free oscillations using the built-in SPM-system from the company "PolyTec" (Germany). The obtained stiffness values were in the range from 50–53 N/m. The cantilevers with probes of symmetrical parabolic shape with radius of curvature 30–50 nm with wear-resistant silicon carbide coating from "TeamNanotec GmBH" (Germany) were used. The choice of such probes was due to the possibility of more accurate characterization of their apex geometry. Probe geometry was assessed using SEM-micrographs followed by a piecewise linear interpolation procedure (Fig. 4).

The values of E_{loc} were calculated using LabVIEW program within the framework of Sneddon's contact mechanical model [22]:

$$H(a) = \int_0^1 \frac{f'(x)dx}{(1-x^2)^{1/2}},$$

$$kD(a,E) = \frac{2Ea}{(1-\nu^2)} \int_0^1 \frac{x^2 f'(x)dx}{(1-x^2)^{1/2}},$$

where: *H is* the indentation depth; *a* is the probe-sample contact radius; *E* is the sample modulus of elasticity; *v* is the Poisson's ratio of the sample; *k* is the cantilever stiffness; *D(a, E)* is the cantilever bending during indentation; *f' (x) = w(ax),* where *w* is the coefficient describing the geometry of the probe apex, equal to 1.5 for a paraboloid of rotation. The details of the probe geometry estimation and E_{loc} calculation using the adapted Sneddon model minus the hysteresis contribution are presented in [27].

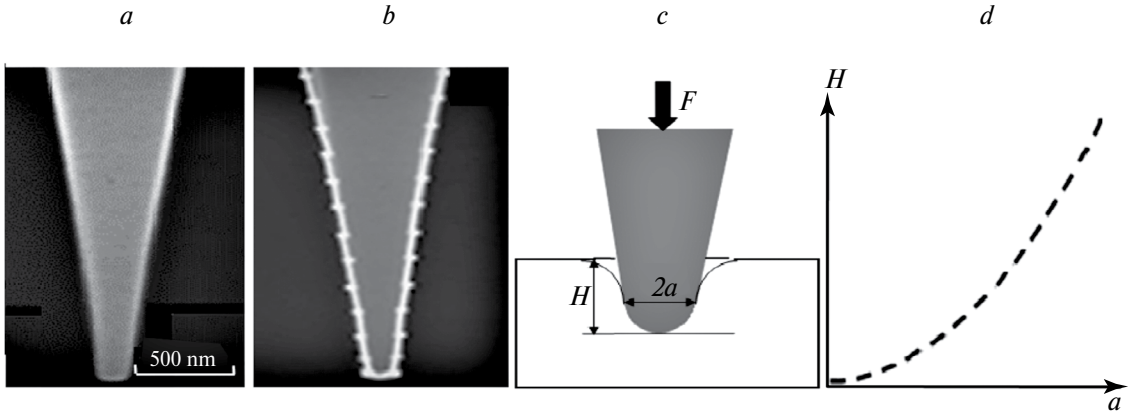

Fig. 4. Estimation of the probe geometry using the piecewise linear interpolation method. *a* – SEM-micrograph of the parabolic probe; *b* – Profile of the probe through a set of rectilinear segments; *c* – Scheme of the probe indentation into the sample surface; *d* – Graph of the function *H(a)* determining the radius of the probe contact with the hypothetical sample at any current indentation depth

3. DISCUSSION OF RESULTS

3.1. Cross section

3.1.1. Structure

Figure 5a shows an optical photograph of a cross-sectional microtomized hair impregnated in epoxy resin. The AFM topographic image of a cross section including the outer cuticular zone and part of the adjacent right cortex zone is shown in Fig. 5b. The cuticle is an ensemble of parallel oriented sublayers, a detailed image of which is shown in Fig. 5 (c, d). Each sublayer (450–600 nm wide) is tightly connected with the neighboring one, forming the so-called membrane complex. As noted above, the main structural elements of each membrane are the so-called A-layer, exocuticle and endocuticle. According to [9] the outer A-layer is a component with a high cysteine content (>30%). It is highly cross-linked and tightly binds neighboring protein layers via disulfide bonds, which provides significant mechanical strength, chemical resistance and low swelling of hair in water. The exocuticle immediately adjacent to the A-layer contains ~15% cysteine, while the endocuticular layer contains only ~3% cysteine [28]. The topographic image in Fig. 5c shows that the exocuticular cells are 150–200 nm wide deepened and the endocuticular layer cells are elevated by ~13 nm and their width is 300–400 nm. In [29], endocuticular cells were found to be more friable due to lower cross-linking sulfur content. This conclusion is supported by the phase image in Fig. 5g, where a less dense (porous) packing of the material is visualized.

The most voluminous part – the cortex – structurally represents irregularly shaped domains with a transverse size from 0.2 to 2.0 μm (Fig. 5 e, f). In contrast to the cuticle, it is in the cortex that rounded-shaped inclusions with a diameter of~ 100 nm are visible, which appear to be particles of melanin pigment that determines hair color (Fig. 5e, f). In addition, the detailed phase image (Fig. 5e) clearly shows that a single subdomain of the cortex is surrounded by a light in contrast chain-like border. The latter is probably the so-called S-border formed by transverse disulfide cross-links, which provide high mechanical strength and elasticity of the hair.

3.1.2. Nanoindentation

Figure 6a shows a topographic image of the cuticular zone of the hair with traces left after the nanoindentation procedure. It can be seen that indents in the elevated exocuticular zones are clearly visualized and have a much larger diameter than indents in the endocuticular layers. This fact correlates with the above-mentioned statement about a denser degree of cross-linking and corresponds to the data of [29]. In addition, around the indents in the exocuticular layers, light contrast framing is visible, indicating a more pronounced irreversible plastic deformation (G) developed during nanoindentation. This conclusion is confirmed by the characteristic force curves for both zones (Fig. 6b, c). It can be seen that the plastic deformation in the stiffer zones is almost 2 times smaller than in the more pliable zones. The averaged values of E_{loc} determined from the slope of the unloading curve in its initial zone using the modified Sneddon equation are: 6.1 ± 0.6 GPa for the stiffer endolayer and 3.9 ± 0.7 GPa for the exolayer.

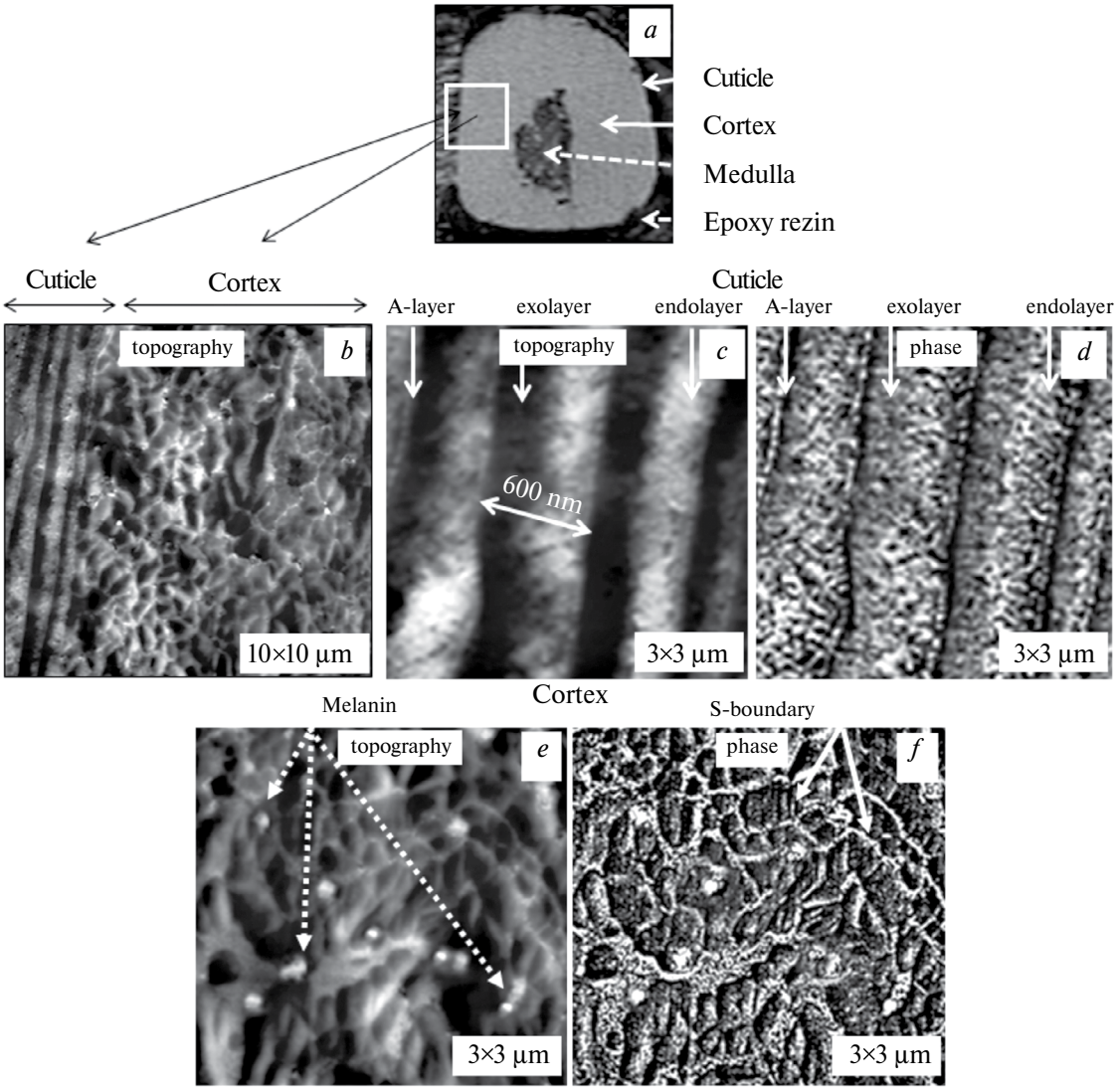

Fig. 5. Features of the internal structure of the hair in perpendicular section. *a* – Optical image of microtomized hair impregnated in epoxy resin. *b* – Topographic image of the outer cuticular zone (left) and part of the cortex zone (right). *c, d* – Detailed topographic and phase images of the cuticle. *e, f* – Detailed topographic and phase images of the cortex

Figure 7 illustrates a topographic image of the cortex zone in the transverse direction with traces of indents and force curves obtained in characteristic structural regions. Three regions can be distinguished, where diameter and depth of indents, as well as local elastic modulus differ markedly (Fig. 7b – d). The variation of the elasticity index in the cortex matrix is probably related to the presence of functionally different cortical cells (para- and ortho-), which differ in the degree of cysteine cross-linking and the density of fibril twisting. Straight hair contains mainly paracortical cells, while curly hair is enriched with orthocortical cells. In our experiment, the paracortical regions of the cortex are 2.5 times stiffer than the orthocortical regions (highlighted by a rectangle): $E_{loc\ para-} = 7.8 \pm 0.5$ GPa (Fig. 7b) vs. $E_{loc\ ortho-} = 2.8 \pm 0.6$ GPa (Fig. 7c). At melanin pigment localization sites (highlighted by circles in Fig. 7d), $E_{loc\ melanin} = 0.9 \pm 0.4$ GPa.

3.2. Longitudinal section

3.2.1. Structure

Figure 8a shows an optical photograph of a longitudinally microtomized hair impregnated in epoxy resin. AFM topographic image of the conjugated zones of cuticle and cortex in the longitudinal direction is shown in Fig. 8b, c. Comparing the structural features in transverse and longitudinal directions

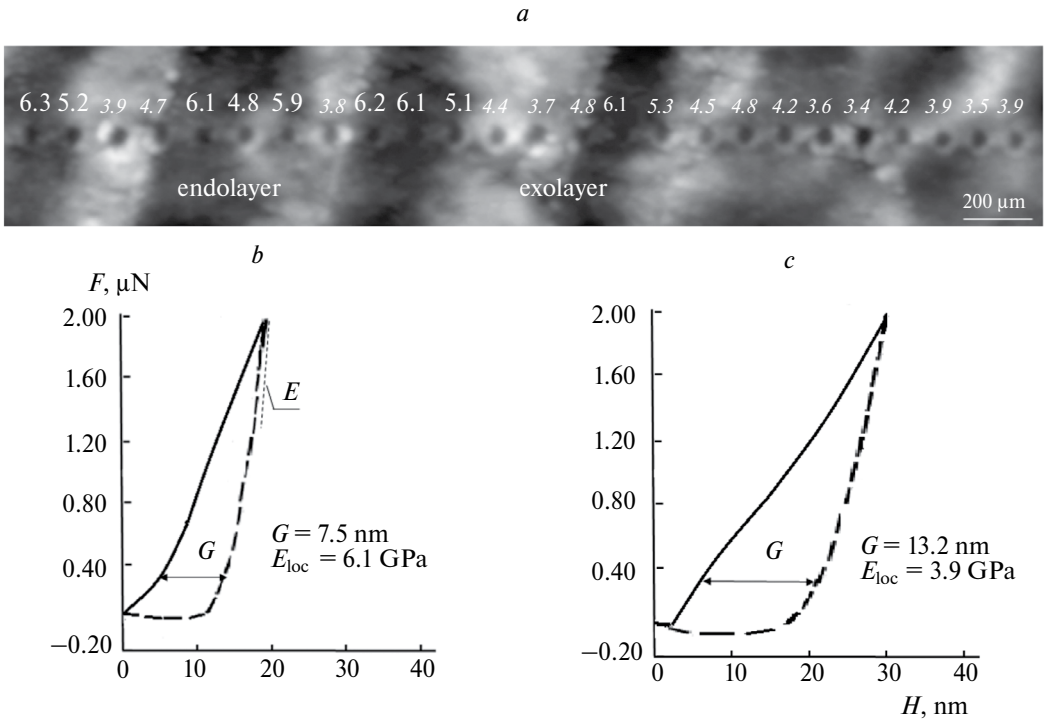

Fig. 6. *a* – Topographic image of the cuticle showing indentation marks and indices of local Young's modulus values for the endo- and exolayer. *b, c* – Characteristic force curves

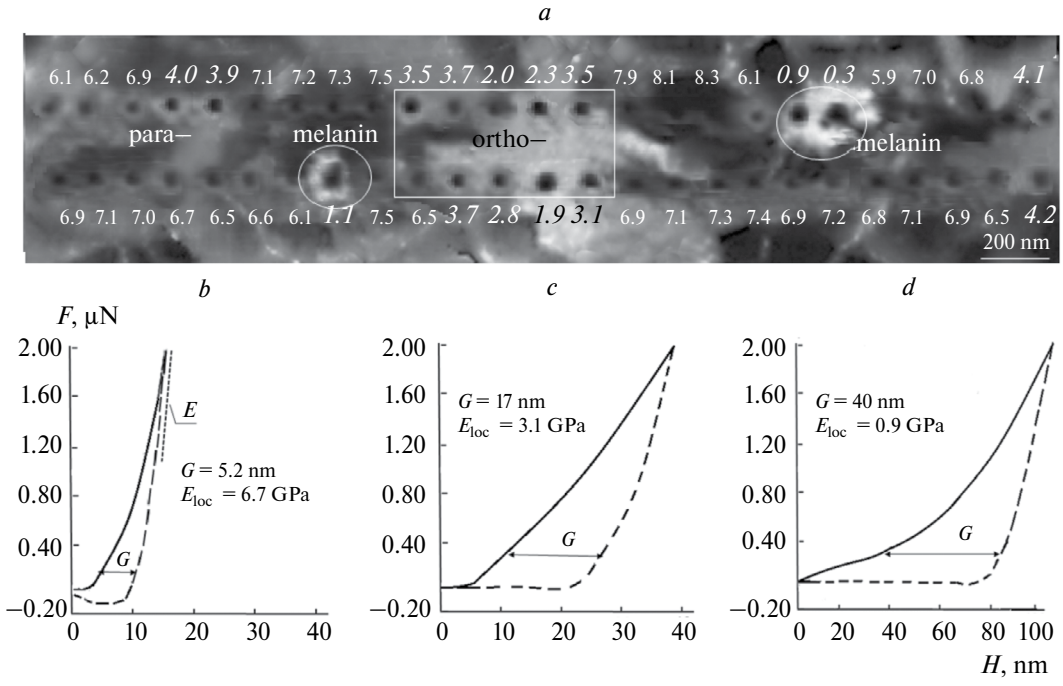

Fig. 7. *a* – Topographic image of the cortex with indentation traces and indices of local Young's modulus values. *b-d* – Characteristic force curves in different zones of the cortex

(Fig. 5a vs. Fig. 8a), one can see the obvious manifestation of morphological anisotropy in both cuticle and cortical areas. It should also be noted that the spiral-shaped structure of the hair cuticle obtained by AFM visually coincides with the α-keratin image predicted by Pauling and Corey using the X-ray method (Fig. 2) [5]. Figure 8c shows that the width of a single twisted cuticle cell is about 600 nm.

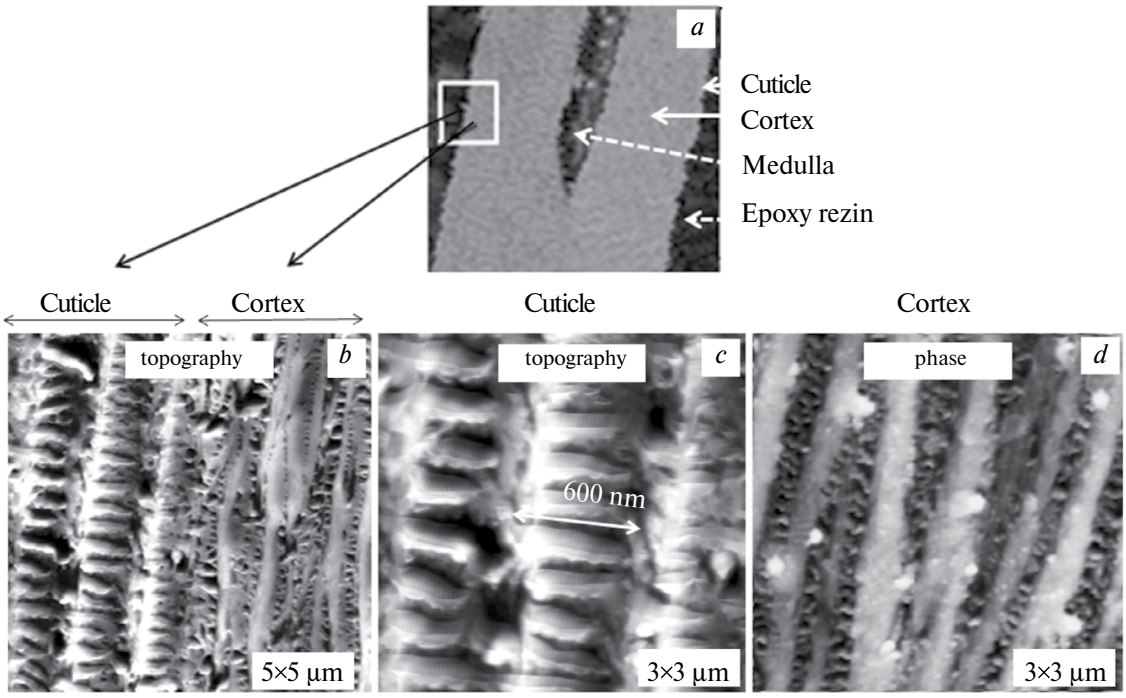

Fig. 8. Features of internal structure of hair in longitudinal section. *a* – Optical image of microtomized hair impregnated in epoxy resin; *b* – AFM topographic image of substructures in conjugated areas of cuticle and cortex *c, d* – Magnified topographic images of cuticle and cortex areas, respectively

Figure 8g illustrates the topography of the cortex, which shows elongated fibers (filaments) of various widths from 70 to 180 nm located along the hair. According to [30] the organization of these filaments is an ensemble of hierarchically organized α-helices. Small clusters of three protofibrils twisted together then twist into nine, forming a kind of "cable" known as a microfibril, which is embedded in an amorphous protein-rich matrix. The hundreds of microfibrils are then organized into a fibrous bundle called polypeptide macrofibrils.

The topographic image (Fig. 8d) also shows that polypeptide marcofibrils are connected in the perpendicular direction by ~15 nm wide ties. These ties are probably cysteine bridges with disulfide bonds involved in the elastic stretching mechanism of the hair. In addition, Fig. 8g visualizes light inclusions of rounded shape with a transverse size of 80–100 nm, which are probably inclusions of melanin pigment.

3.2.2. Nanoindentation

Structural anisotropy is also manifested in the difference of the elastic response in mutually perpendicular sections of the hair. Fig. 9a shows a topographic map of the cuticular zone in the longitudinal direction with localization of the locations where nanoindentation was performed.

It can be seen that, in contrast to previous cases, no indentation marks are observed. This is explained by the fact that the cuticular cell in the direction perpendicular to the helix turn behaves elastically during indentation, demonstrating the effect of rapid restoration of the original shape of the material after applied loading without development or with a small manifestation of hysteresis (Fig. 9b, c). The averaged local Young's modulus in these zones is $E_{loc} = 9.2 \pm 0.7$ GPa. The white points ($E_{loc} = 7.3 \pm 0.4$ GPa) correspond to the location of indents that fell outside the main plane of the helical link. In dark contrast zones, located between neighboring turns of the helix, SCs were not produced due to a large height difference (~ 100 nm).

Figure 10a illustrates the topography of the longitudinal section of the cortex zone with indentation traces and local Young's modulus values. In this zone, we were only able to obtain force curves in the monolithic keratin regions located along the main axis of the hair, where the average local Young's modulus was found to be $E_{loc} = 4.2 \pm 0.4$ GPa. However, force curves that

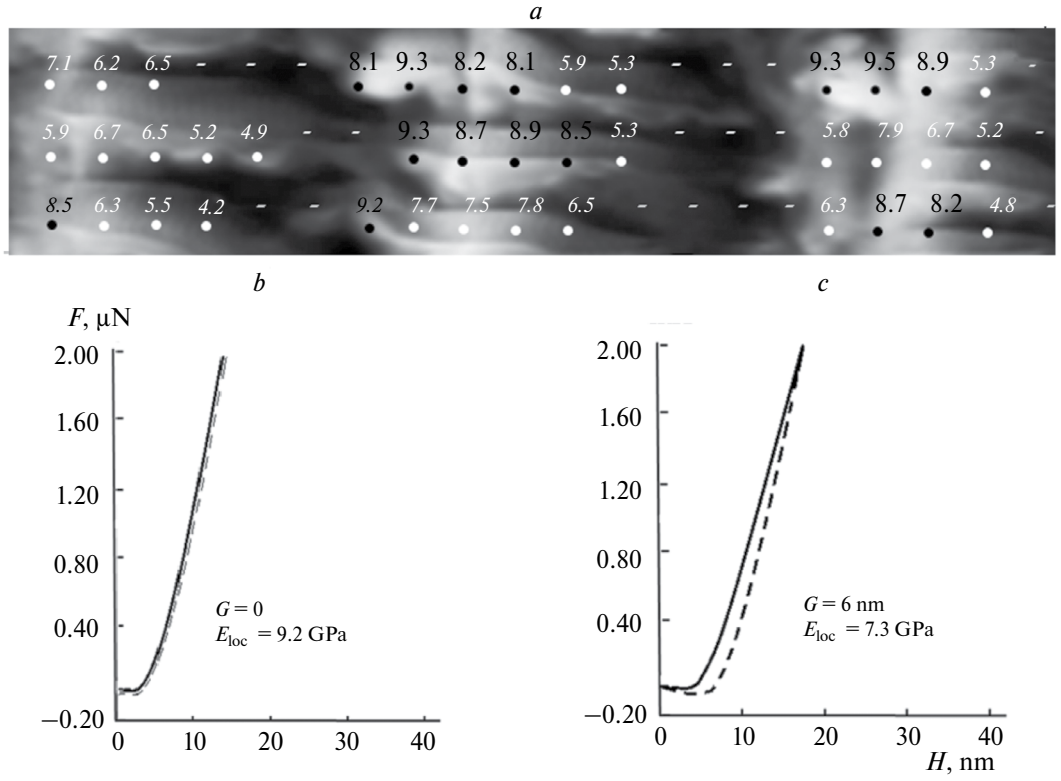

Fig. 9. *a* – Topographic image of the internal structure of the cuticle in the longitudinal direction with indentation of indents location and indices of local Young's modulus values. *b, c* – Characteristic force curves in different zones of the cuticle

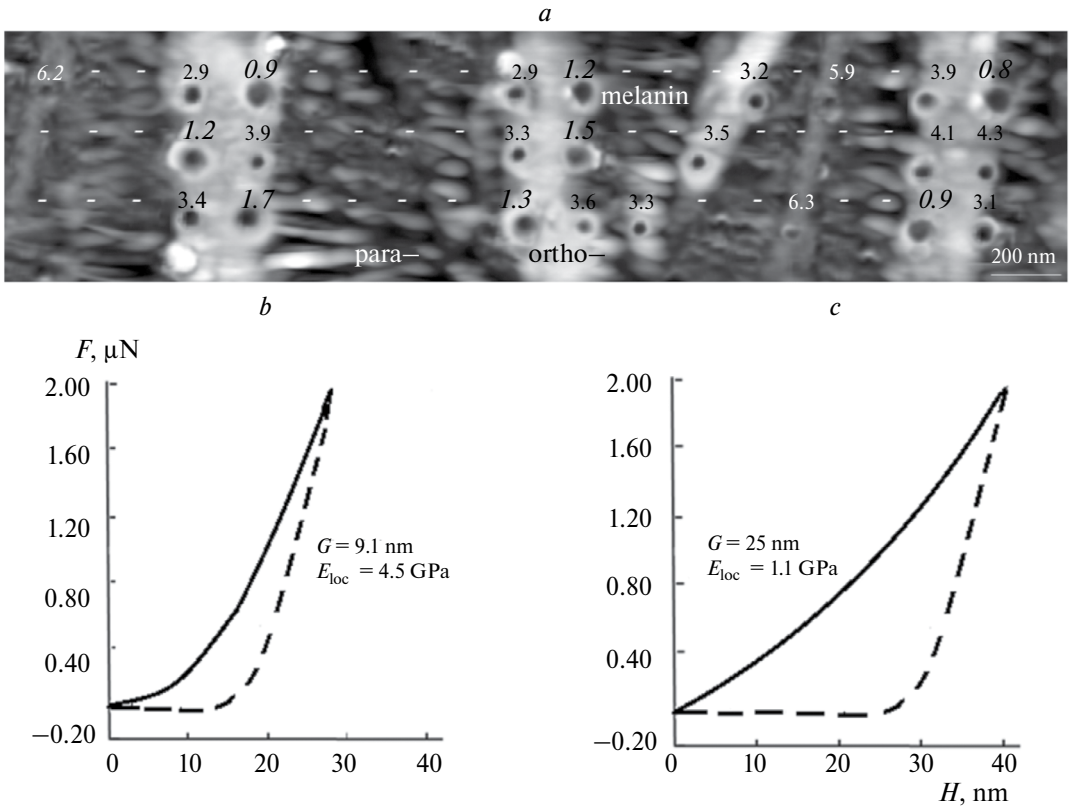

Fig. 10. *a* – Topographic image of the cortex in the longitudinal direction with indentation of indents location and indices of local Young's modulus values. *b, c* – Characteristic force curves in different cuticle zones.

could be taken into account were not reproducibly produced in the darker contrasting (lower) regions. This was probably due to the probe being snagged by transverse disulfide binding ties during extraction from the material, and the initial slope of the unloading curve was not reliably reconstructed. The modulus of elasticity at melanin localization sites was $E_{loc\ mel} = 1.0 \pm 0.3$ GPa.

It should also be noted that the accuracy of the modulus measurement results is affected both by height differences between different morphological elements on the topographic map and by the ratio between the geometric dimensions of structural units and the probe tip. When the linear size of a structural unit is smaller than the size of the contacting probe, the so-called convolution effect – overlapping of the measured structure by the probe – appears. In such situations, the measured values will differ from the true values, which affects the value of statistical scatter.

4. CONCLUSION

The features of the internal structure of the main functional zones (cuticle and cortex) of the native human hair microtomized in transverse and longitudinal directions have been characterized in detail using the AFM method. It is these morphologically complexly organized areas that determine the strength, elasticity and color of hair. It is demonstrated that the hair microstructure is characterized by pronounced structural anisotropy in both morphological zones.

In addition, the local Young's modulus in each structural element was quantitatively measured using AFM nanoindentation. In order to quantitatively measure the local Young's modulus, a preliminary procedure was carried out to fully calibrate the AFM system. The calibration included the steps of measuring the system sensitivity, determining the cantilever stiffness, and estimating the probe apex geometry using TEM followed by a piecewise linear interpolation procedure. An adapted Sneddon model using static analysis was used to calculate Young's modulus.

The nanoindentation method was used to quantify the local elastic modulus in all structurally different regions of the sample, which is not possible in macroscopic studies when generalized integral information is collected for the entire volume of the material under study. The nanoindentation experiment showed that it is the cuticle with densely packed spiral bundles of α-keratin, despite its smaller volume fraction compared to the cortex zone, that determines the elastic properties of the hair.

In the next stage of the study, the structure and measured local elastic properties of hair from the same batch after chemical treatment procedures are expected to be studied using similar techniques.

ACKNOWLEDGEMENTS

The author is grateful to Bruker NanoSurface Inc. (USA) for the opportunity to work on the MultiMode™ AFM microscope.

CONFLICT OF INTERESTS

The author declares that he has no conflict of interest with any party.

ETHICS DECLARATION

This article does not contain any studies using animals as subjects.

REFERENCES

1. *Robbins C. R.*. Chemical and Physical Behavior of Human Hair. N. Y.: Springer, 1988.
2. *Fernandes C., Medronho B., Alves L., Rasteiro M.* // Polymers. 2023. Vol. 15. No. 3. P. 603. https://doi.org/10.3390/polym15030608
3. *Chen N., Bhushan B.* // J. Microscopy. Microscopy. 2005. Vol. 220. P. 96. https://doi.org/10.1111/j.1365–2818.2005.01517.x
4. *Araujo R., Fernandes M., Cavaco-Paulo A., Gomes A.* // Adv. Biochem. Eng./Biotechnol. 2010. Vol. 125. https://doi.org/10.1007/10_2010_88
5. *Pauling L., Corey R. B., Branson H. R.* // Proc. Nat. Acad. Sci. 1951. Vol. 37. No. 4. https://doi.org/10.1073/pnas.37.4.205
6. *Brill R.* //Anal. Chim. 1923. Vol. 434. P. 204.
7. *Feughelman, M.* // Text. Res. J. 1959. P. 223.
8. *Bendit E. G.* // Ibid. 1960. Vol. 30. P. 547.
9. *Mkentane K.* PhD Thesis. Department of Medicine (Trichology & Cosmetic Science). University of Cape Town, 2016.
10. *Binnig G., Rohrer H., Berber C.* // Appl. Phys. Lett. 1981. Vol. 40. No. 2. P. 178.
11. *Grishin M. V., Gatin A. K., Sarvady S. Yu. et al.* // Chemical Physics. 2020. Vol. 39. No. 7. P. 63. https://doi.org/10.31857/S0207401X20070067
12. *Gatin A. K., Sarvadiy S. Yu., Dokhlikova N. V., Grishin M. V.* // Chem. Physics. 2021. Vol. 40. No. 6. C. 10.

https://doi.org/10.31857/S0207401X21060042
13. *Grishin M. V., Gatin A. K., Slutsky V. G., et al.* // Chem. Physics. 2022. Vol. 41. No. 1. P. 3. https://doi.org/10.31857/S0207401X22060048
14. *Grishin M. V., Gatin A. K., Slutsky V. G. et al.* // Chem. Physics. 2023. Vol. 42. No. 1. P. 3. https://doi.org/10.31857/S0207401X23010053
15. *Binnig G., Quate C. F., Gerber. Ch.* // Phys. Rev. Lett. 1986. Vol. 56(9). P. 930. https://doi.org/10.1103/PhysRevLett.56.930
16. *Magonov S. N.* Atomic Force Microscopy in Analysis of Polymers. In Encyclopedia of Analytical Chemistry. / Ed. Meyers R. M. Chichester: John Willey & Sons Ltd, 2000. https://doi.org/10.1002/9780470027318.a2003
17. *Pittenger B., Erina N. A., Su C.* Nanomechanical Analysis of High Performance Materials. Dordrecht: Springer, 2014. https://doi.org/10.1007/978–94–007–6919–9_2.
18. *Zhong Q., Innis D., Kjoller K., Elings V.* // Surf. Sci. Lett. 1993. Vol. 290. No. 7. P. 1688.
19. *Sahin O., Magonov S., Su C., Quate C. F., Solgard O.* // Nature Nanotechnol. 2007. Vol. 2. No. 8. P. 507 https://doi.org/10.1038/nnano.2007.226
20. *Weisenhorn A. L., Hansma P. K., Albrecht T. R., Quate C. F.* // Appl. Phys. Lett. 1989. Vol. 54. P. 2651 https://doi.org/10.1063/1.101024
21. *VanLandingham M.R, McKnight S. H. et al.* // J. Adhesion. Adhesion. 1997. Vol. 64. P. 31.
22. *Sneddon I. N.* // Int. J. Eng. Sci. 1965. 3. P. 47. https://doi.org/10.1016/0020–7225(65)90019–4
23. *Smith J. R. Swift J. A.* // Micron. 2005. Vol. 36. P. 261. https://doi.org/10.10116.j.micron.2004.11.004
24. *Smith J. R., Tsibouklis J., Nevel T. G., Breakspear S.* // Appl. Surf. Sci. 2013. Vol. 285. Pt B. P. 638. https://doi.org/10.1016/j.apsusc.2013.08.104
25. *Rogers G.* // Cosmet. Sci. 2013. Vol. 6. No. 2. P. 32 https://doi.org/10.3390/cosmetics6020032
26. *Mcmullen R. L., Zhang G.* // J. Cosmet. Sci. 2020. Vol. 71. P. 117.
27. *Belikov S., Erina N., Huang L. et al.* // J. Vac. Vac. Sci. Tech. B. 2009. Vol. 27. P. 984. https://doi.org/10.1017/S1431927616002622
28. *Parbhu A., Bryson W., Lal R.* // Biochemistry. 1999. Vol. 38. P. 11755. https://doi.org/10.1021/bi990746d
29. Aebi U., Fowler W. E., *Rew P, Sun T-T.* // J. Cell Biology. 1983. Vol. 97. P. 1131. https://doi.org/10.1083/JCB.97.4.1131
30. *Ezawa Y., Nagase S., Mamada A. et al.* // Cosmetics. 2019. Vol. 6. P. 24. https://doi.org/10.3390/cosmetics6020024